

Potential use of quasicrystalline materials as thermal barrier coatings  
for diesel engine components

by

M. Brad Beardsley

A dissertation submitted to the graduate faculty  
in partial fulfillment of the requirements for the degree of

DOCTOR OF PHILOSOPHY

Major: Materials Science and Engineering

Program of Study Committee:  
Brian M. Gleeson, Major Professor  
Daniel J. Sordet  
R. Bruce Thompson  
Palaniappa A. Molian  
L. Scott Chumbley

Iowa State University

Ames, Iowa

2008

UMI Number: 3307088



---

UMI Microform 3307088

Copyright 2008 by ProQuest Information and Learning Company.  
All rights reserved. This microform edition is protected against  
unauthorized copying under Title 17, United States Code.

---

ProQuest Information and Learning Company  
300 North Zeeb Road  
P.O. Box 1346  
Ann Arbor, MI 48106-1346

Dedicated to Jan, for her support and push.

## Table of Contents

	Page
List of Figures	v
List of Tables	xvii
Acknowledgements	xix
1.0 Introduction	1
2.0 Thermal Barrier Coating Background	4
2.1 Thermal Spray Processes	4
2.2 History of Thermal Barrier Coating Applications to Turbine Engines	7
2.3 Advanced Thermal Barrier Coating Systems	9
2.4 Application of Thermal Barrier Coating Systems to Diesel Engines	11
2.5 Failure Mechanisms and Limitations of TBC Systems in Diesel Engines	17
2.6 Mechanical Properties of TBCs via Instrumented Micro-Indentation	24
3.0 Quasicrystals and Approximants as Alternative Coatings in Diesel Engines	27
3.1 Quasicrystal and Approximant Properties	27
3.2 Quasicrystal and Approximant Coatings	29
3.3 Primary Issues That Need to be Addressed for Application of QC as TBC	31
4.0 Experimental Procedures	32
4.1 Coating Materials	32
4.2 Spray Process	33
4.3 Diffusion Experiments	35
4.4 Characterization of Coatings and Powder via SEM, Microprobe and XRD	36
4.5 Diffusion Analysis Procedure	37
4.6 Mechanical Properties of Quasicrystal Coating via Instrumented Micro-Indentation	41
5.0 Results	46
5.1 Analysis of Starting BT1 QC Powder	46
5.2 Coating Deposition	48
5.3 Microstructure, XRD and Instrumented Indentation of BT1 QC Coating	50
5.4 Quasicrystal and Bond Coat/Substrate Interaction	61
5.5 Interlayer Thickness Analysis	75
5.6 Estimation of Average Interdiffusion Coefficients	84
5.7 Root-Mean-Squared Penetration Depths	96

## Table of Contents (continued)

6.0	Discussion	98
6.1	Mechanical Properties	99
6.2	Interface Diffusion Interactions	104
6.3	Diffusion Coefficients	118
6.4	Bond Coat and Graded Material Selection	120
7.0	Conclusions	122
	References	123

## List of Figures

	Page
Figure 1-1. Typical microstructure of a graded TBC applied to diesel engine components showing the 100% zirconia top coating (left), center graded section of zirconia and bond coating, and bond coat/substrate interface (right). The crack resulted from thermal stress induced during engine testing.	2
Figure 1-2. Thermal conductivity of a zirconia TBC as a function of coating porosity from internal data at Caterpillar.	2
Figure 1-3. Microstructure of a PVD deposited zirconia TBC used in turbine applications showing the columnar structure of the coating [1].	3
Figure 2.1-1. Schematic of Rockide type spray torch showing rod feedstock and air cap arrangement for melting and atomizing the material [6].	5
Figure 2.1-2. Schematic of a plasma spray torch showing the basic electrode/anode and gas arrangement of a typical DE plasma system. Powder is injected either internally or external of the nozzle [6].	5
Figure 2.1-3. Schematic of a HVOF torch showing the combustion chamber and nozzle arrangement with axial powder injection. Some torches use converging/diverging nozzle designs to increase gas velocity [6].	6
Figure 2.2-1. Timeline for the development of high temperature superalloys for turbine applications showing the continued improvement in high temperature capability of the alloys [7].	8
Figure 2.3-1. Gas burner rig for heating of TBC samples to similar temperature ranges as found in turbine engines [18].	11
Figure 2.4-1. Diesel engine exhaust valves coated with a 0.5 mm thick zirconia TBC to lower valve face temperature to prevent attack by liquid vanadium pentoxide [22].	12
Figure 2.4-2. Cross section of a TBC piston after engine testing showing the cracking in the coating caused by the bending stress in the bowl area and high compressive stress on the top land [22].	13
Figure 2.4-3. Bending fatigue sample of ceramic layer of TBC showing spalling failure similar to that of the TBC piston shown in Figure 2.4-2. [24]	14

## List of Figures (continued)

	Page
Figure 2.4-4. Finite element analysis of TBC and piston substrate showing temperatures under peak load conditions [22]. TBC coating on top land only as indicated.	15
Figure 2.4-5. Heat release diagram of engine combustion for metal baseline engine, unsealed TBC and sealed TBC engine showing longer heat release time for unsealed TBC engine components [21].	16
Figure 2.4-6. Glass composite sealed piston showing cracking and chipping of the glass seal coating after only 100 hours of engine testing [22].	16
Figure 2.5-1. Goodman type diagram of mean and alternating stress levels for design of TBC systems.	17
Figure 2.5-2. Schematic of stress state resulting from the applied thermal load on the TBC in a diesel engine. [from E. Redja, University of Illinois]	19
Figure 2.5-3. Tubular specimen developed by Caterpillar and University of Illinois for testing the ceramic TBC in tension /compression [27].	19
Figure 2.5-4. Stress-strain response of a zirconia TBC tested using the specimen geometry shown in Figure 2.5-3 [28].	20
Figure 2.5-5. Fatigue response of ceramic TBC showing high strength in compression and low tensile strength. Data points with mean compressive stress demonstrate that the failure mechanisms in tension and compression do not interact, the failure is either due to the maximum compressive stress or maximum tensile stress [27].	20
Figure 2.5-6. Stress-strain response of ceramic TBC held for one hour at a temperature of 800°C at the indicated stress. Increasing modulus with stress level indicates that the material has crept under load [27].	21
Figure 2.5-7. Thermal mechanical test of ceramic TBC showing that creep at high temperature and stress can result in a tensile stress on cooling. This is similar to the stress-strain history of a TBC on a metallic substrate during heating and cooling [28].	21

## List of Figures (continued)

	Page
Figure 2.5-8. Proposed model by Redja, et al. [28], to explain the non-linear stress strain response of the TBC. Model prediction is compared to actual measurement in Figure 2.6-9.	23
Figure 2.5-9. Model results compared to actual measured stress-strain of ceramic TBC [28]	23
Figure 2.5-10. Thermal mechanical prediction compared to resulting failures indicating that the proposed model of Redja, et al., appears to be valid [28].	24
Figure 2.6-1. Modulus of elasticity for 8% YSZ coating (Lot 39073) as a function of applied load is shown as measure by Redja et al. using free standing tube specimens [28].	26
Figure 2.6-2. Modulus of the same 8% YSA coating as in Figure 4.7-1 as a function of applied load is shown but measured using instrumented indentation method with spherical indenter.	26
Figure 3.1-1. Yield stress of QC materials decrease with temperature and approaches zero at 1000°C [36]	29
Figure 4.1-1. Schematic showing the setup for spraying of the diffusion couple samples using the Sulzer Metco DJ2700 spray torch and the two types of specimens sprayed, BT1 on one of the MCrAlY bond coats or BT1 on the SAE steel substrate.	33
Figure 4.5-1. Schematic of concentration profile for component i of a multicomponent diffusion couple.	38
Figure 4.5-1. Diffusion profile for component i of a multicomponent diffusion couple with a multiple phases in the couple. The diffusion coefficient is evaluated on either side of the middle phase.	41
Figure 4.6-1. Typical load displacement curves for BT1 coating indentation using the Vickers and spherical indenters are shown. The measurements shown were on the BT1 QC coating held at 700°C for 500 hours.	43

## List of Figures (continued)

	Page
Figure 4.6-2. Vickers indenter impressions at 1N and 5N loads in cross sections of the BT1 QC coating showing the relative size of the Vickers impression (a) to that of the coating “splat” structure (b) created by the impact of individual powder particles. The circle (c) represents the area of contact of the 0.4 mm diameter spherical indenter showing the large area and volume of the coating that is being sampled.	44
Figure 4.6-3. Schematic representation of the coating depth and volume sampled by the Vickers and spherical indenters (not to scale).	45
Figure 5.1-1. XRD pattern for the as received powder and annealed powders showing the fewer and less defined peaks found in the as received powders.	47
Figure 5.1-2. BT1 QC powder particle showing the instrumented indents with minor cracking around some of the indents.	47
Figure 5.2-1. Typical microstructure of BT1 QC sprayed with initial parameters in Figure 5.2-1 which exhibit lack of fusion between particles and high crack density.	48
Figure 5.2-2. Particle speed and temperature for the experimental runs from Table 4.2-1 are shown. Run 13 in Table 4.2-1 (circled points above) has the highest temperature and speed of the parameters tested which resulted in the highest deposition efficiency	50
Figure 5.3-1. BT1 QC coating microstructure sprayed with the selected HVOF parameters showing high density with microcracks typical of hard coating sprayed by HVOF. The coating features such as pores, microcracks and the deposited powder particles that comprise the lamellar coating structure are identified in (b).	51
Figure 5.3-2. Microstructure of BT1 QC coating exposed at 500°C for 25 hours (a,c) and 500 hours (b,d) showing similar coating porosity and microcracking density to that of the as-sprayed coating. The 500 hour microstructure has precipitates which are attempted to be indicated by the arrows in (d). EDS analysis showed the precipitates to be higher in chrome and cobalt than the matrix of BT1 coating.	52

## List of Figures (continued)

	Page
Figure 5.3-3. XRD patterns for BT1 quasicrystal material are shown for the various diffusion couples after exposure at temperature. Note the peaks that begin to appear in the 500 hr at 500°C scan in the 20 to 35 2-theta range. These peaks appear strongly in the 25 hr at 700°C and 25 hr 900°C samples but have nearly disappeared in the 500 hr 700°C and 900°C samples.	53
Figure 5.3-4. Hardness (top), Vickers modulus (middle) and spherical modulus (bottom) of 500°C BT1 QC coating samples measured by instrumented indentation are shown. Error bars indicate one standard deviation for the 10 measurements on each specimen.	55
Figure 5.3-5. Microstructure of BT1 QC coating exposed at 700°C for 25 hours (a,c) and 500 hours (b,d) showing porosity and microcracking density decreasing with increase time at temperature. The 500 hour microstructure has precipitates (indicated by arrows in d) similar to those in the 500°C-500 hour sample but are large (visible at 5000X as compared to the 10,000X for the 500°C sample in Figure 5.3-2).	56
Figure 5.3-6. Hardness (top), Vickers modulus (middle) and spherical modulus (bottom) of 700°C BT1 QC coating samples measured by instrumented indentation are shown. Error bars indicate one standard deviation for the 10 measurements on each specimen.	57
Figure 5.3-7. Microstructure of BT1 QC coating exposed at 900°C for 25 hours (a,c) and 500 hours (b,d) showing decrease porosity and microcracking density at 25 hour compared to the as-sprayed coating and nearly complete microcrack elimination at 500 hours with coalescences of the porosity (b,d). The 500 hour microstructure has precipitates (indicated by arrows in d) similar to those in the 500°C-500 hour and 700C-500 hour sample but again are coarser than those at the lower temperatures.	58
Figure 5.3-8. Higher magnification of boxed area in Figure 5.3-9d showing location of EDS analysis shown in table. The lighter areas show an increase in chromium and a relative increase in iron and cobalt relative to the surrounding matrix.	59

## List of Figures (continued)

	Page
Figure 5.3-9. Hardness (top), Vickers modulus (middle) and spherical modulus (bottom) of 900°C BT1 QC coating samples measured by instrumented indentation are shown. Error bars indicate one standard deviation for the 10 measurements on each specimen.	60
Figure 5.4-1. Interface between the BT1 QC coating and the SAE 1040 steel substrate and bond coats showing little change after exposure at 500°C for 500 hours. Embedded alumina grit from the surface prep is visible in the SAE 1040-BT1 couple. As the bond coats were not grit blasted prior to spraying the BT1 QC coating the interfaces of those couples do not have embedded grit.	62
Figure 5.4-2. Microprobe concentration profile aligned with SEM image of microstructure of interface between the BT1 – Ni-17Cr-6Al-0.5Y bond coat at 500°C after 500 hours in showing the small diffusion distances of the species. All of the couples showed similar small diffusion zones, on the order of 5 microns.	63
Figure 5.4-3. Interface between the BT1 QC coating and the SAE 1040 steel substrate (left) and Fe26Cr9Al0.4 bond coat (right) at 700°C showing progression of interlayer phase in the Fe26Cr9Al0.4-BT1 couple (marked with “c” in photos). No interlayer phase is seen in the SAE 1040-BT1 couple even after 500 hours.	64
Figure 5.4-4. Interface between the BT1 QC and the Ni17Cr6Al0.5Y (left) and Ni31Cr11Al0.6Y (right) bond coats at 700°C showing progression of interlayer zone in both couples. An initial interlayer forms at 25 hours (c) that thickens with time. Kirkendall voids form on the BT1 side of the couples (d). A region appearing to be a diffusion zone (a) develops on the bond coat side of the couples.	65
Figure 5.4-5. Microprobe results for the 700°C-500 hour SAE 1040-BT1 QC couple showing no interlayer phase and small diffusion distances for the species.	67
Figure 5.4-6. Microprobe analysis of the Fe26Cr8Al0.4Y-BT1 couple showing the interlayer phase to be aluminum and iron compound roughly equal to that of FeAl <sub>2</sub> .	68

## List of Figures (continued)

	Page
Figure 5.4-7. Microprobe concentration profile aligned with SEM image of microstructure of interlayer formed 700°C after 100 hours in BT1 – Ni17Cr6Al0.5Y bond coat showing how the concentration of aluminum and nickel align with the structure observed. The interlayer phase is seen to be primarily nickel and aluminum with a composition similar to Ni <sub>2</sub> Al <sub>3</sub> .	69
Figure 5.4-8. Microprobe concentration profile aligned with SEM image of microstructure of interlayer formed 700°C after 500 hours in BT1 – Ni17Cr6Al0.5Y bond coat showing how the concentration of aluminum and nickel align with the structure observed. The interlayer phase is seen to be primarily nickel and aluminum with a composition similar to Ni <sub>2</sub> Al <sub>3</sub> .	70
Figure 5.4-9. Interface between the BT1 QC and the SAE 1040 steel substrate (left) and Fe26Cr9Al0.4 bond coat (right) at 900°C showing progression of interlayer zone in both couples. An initial interlayer develops in both couples at 25 hours that progressively thickens. Kirkendall voids developed on either side of the interlayer (b and d). A region appearing to be a diffusion zone (a) develops in both couples but is very visible in the SAE 1040 substrate	71
Figure 5.4-10. Interface between the BT1 QC and the Ni17Cr6Al0.5Y (left) and Ni31Cr11Al0.6Y (right) bond coats at 900°C showing progression of interlayer zone in both couples. Both couples have an initial interlayer structure consisting of a solid layer with Kirkendall voids (d) in the BT1 QC. Voids also develop in the Ni17Cr6Al0.5Y bond coat (b) at the longer times but not in the Ni31Cr11Al0.6Y bond coat. A region appearing to be a diffusion zone (a) develops on the bond coat side of the couples.	72
Figure 5.4-11. Microprobe concentration profile aligned with SEM image of microstructure of interlayer formed 900°C after 25 hours in SAE 1040-BT1 couple showing how the concentration of aluminum and iron align with the structure observed. The interlayer phase is seen to be primarily iron and aluminum with a composition similar to FeAl.	73

## List of Figures (continued)

	Page
Figure 5.4-12. Microprobe concentration profile aligned with SEM image of microstructure of interlayer formed 900°C after 25 hours in Fe26Cr8Al0.4Y-BT1 couple showing how the concentration of aluminum and iron align with the structure observed. The interlayer phase is seen to be primarily iron and aluminum with a composition similar to FeAl.	74
Figure 5.4-13. Microstructure of the Ni-31Cr-11Al-0.6Y and BT1 interface after holding for 25 hours at 900°C. Note the formation of voids in the BT1 at the short diffusion time and the high scatter in the measured concentration of the nickel in the bond coat.	76
Figure 5.4-14. Microstructure of the Ni-31Cr-11Al-0.6Y and BT1 interface after holding for 500 hours at 900C. The scatter in the measured concentration of the nickel and aluminum in the bond coat is not related to the formation of voids as is the case in the BT1 concentration measurements.	77
Figure 5.4-15. Microprobe concentration profile aligned with SEM image of microstructure of interlayer formed 900°C after 500 hours in BT1 – Ni-17Cr-6Al-0.5Y bond coat showing how the concentration of aluminum and nickel align with the structure observed.	78
Figure 5.5-1. Schematic of interlayer phases showing approximate locations for measurement of phase thickness.	80
Figure 5.5-2. K values for the interlayer thickness plotted as function of temperature to allow for extrapolation to lower temperature interactions.	84
Figure 5.6-1. Concentration and flux profiles for SAE 1040-BT1 and Fe26Cr8Al0.5Y-BT1 diffusion couples held at 500°C for 500 hours. The fluxes outside of the interlayer area are the result of the small concentration fluctuations.	85
Figure 5.6-2. Concentration and flux profiles for SAE 1040-BT1 and Fe26Cr8Al0.4Y-BT1 diffusion couples held at 700°C for 500 hours. Note the positive flux for cobalt diffusion in in the Fe26Cr8Al0.4Y-BT1 couple in contrast to the for the Ni base bond coats. Note the lower aluminum flux in the SAE 1040-BT1 couple as well as the interlayer phase developing in the Fe26Cr8Al0.4Y-BT1 couple at ~50 atom fraction.	86

## List of Figures (continued)

	Page
Figure 5.6-3. Concentration and flux profiles for SAE 1040-BT1 and Fe26Cr8Al0.4Y-BT1 diffusion couples held at 900°C for 25 hours. The high mobility of the aluminum has consumed most of the bond coat thickness. Higher hours at 900C showed completed diffusion of the aluminum through the bond coat . The interlayer composition appears to be close to the FeAl compound and the cobalt flux is negative as in the Ni bond coats with a Al <sub>9</sub> Co <sub>2</sub> compound being formed.	87
Figure 5.6-4. Concentration and flux profiles for the Ni17Cr6Al0.5Y-BT1 and Ni31Cr11Al0.6Y-BT1 diffusion couples held at 500°C for 500 hours. The fluxes outside of the interlayer area are the result of the small concentration fluctuations	88
Figure 5.6-5. Concentration and flux profiles for the Ni17Cr6Al0.5Y-BT1 diffusion couple held at 700°C for 100 hours and the Ni31Cr11Al0.6Y-BT1 diffusion couple held at 700°C for 500 hours. Note the negative flux for cobalt, diffusion to the left against the concentration profile. This is caused by the formation of CoAl compound in the interlayer zone next to the BT1 as well as the NiAl <sub>3</sub> next to the bond coat in each couple. Note the development of a zero flux plane for Co in the Ni31Cr11Al0.6Y-BT1 couple.	89
Figure 5.6-6. Concentration and flux profiles for the Ni17Cr6Al0.5Y-BT1 and Ni31Cr11Al0.6Y-BT diffusion couples held at 900°C for 500 hours. Both cobalt and chromium show a negative flux, diffusion to the left against the concentration profile. The formation of CoAl and chromium-aluminum compounds in the interlayer zone next to the BT1. NiAl is formed next to the bond coat in each couple	90
Figure 5.6-7. The average diffusion coefficient ( $D_{i,C}$ ) for aluminum plotted as a function of temperature using Eq. (22). Note the lower diffusion coefficient for the SAE 1040-BT1 and Fe26Cr8Al0.4Y-BT1 couples at 700°C.	94
Figure 5.6-8. The average diffusion coefficient ( $D_{i,C}$ ) for nickel or iron plotted as a function of temperature using Eq. (22). Note lower diffusion coefficient for the SAE 1040-BT1 and Fe26Cr8Al0.4Y-BT1 couples at 700°C.	95

## List of Figures (continued)

	Page
Figure 6-1. Schematic of the phase development at the interface between the BT1 QC and NiCrAlY bond coats is shown. The nickel flux into the BT1 QC is less than that of the aluminum flux into the bond coat which results in Kirkendall void formation in the BT1 QC. The iron-based bond coat showed similar behavior at both 700°C and 900°C while the SAE 1040 substrate only should interface phases at 900°C.	100
Figure 6.1-1. Deformation model proposed by Redja, et. al. [28] showing relationship between model parameters and the Vickers and spherical moduli measured in this study.	101
Figure 6.2-1. Phase diagram for aluminum and nickel with the three exposure temperatures indicated by the horizontal lines. [55]	107
Figure 6.2-2. Phase diagram for aluminum and cobalt with the three exposure temperatures indicated by the horizontal lines. [55]	107
Figure 6.2-3. Phase diagram for aluminum and iron with the three exposure temperatures indicated by the horizontal lines. [55]	108
Figure 6.2-4. Microstructure of Ni31Cr11Al0.6Y-BT1 diffusion couple after initial 25 hours at 700°C showing the development of the phases at the interface. The NiAl intermetallic phase initially forms at the interface with Al <sub>3</sub> Ni <sub>2</sub> and Al <sub>5</sub> Co <sub>2</sub> forming to the left of the interface as the Al diffuses into the bond coat and a NiAl <sub>3</sub> forming to the right.	109
Figure 6.2-5. Microstructure of Ni31Cr110.6Y-BT1 diffusion couple after 500 hours at 700°C showing the development of the phases at the interface. The NiAl intermetallic phase has thickened with Co substituting into the structure on the BT1 QC side of the interface and Al <sub>3</sub> Ni <sub>2</sub> and Al <sub>5</sub> Co <sub>2</sub> forming in the void area. NiAl <sub>3</sub> on the right side of the interface has also thickened and Cr has increase due to the reduction in Ni as it diffuses into the interface.	110
Figure 6.2-6. Nickel-aluminum phase diagram on the nickel rich side showing the relative location of the aluminum content for the Ni17Cr6Al0.5Y bond coat relative to the Ni31Cr11Al0.6Y bond coat. Note the lower amount of aluminum that would need to be transported to the Ni31Cr11Al0.6Y bond coat to begin the formation of the intermetallic phase at the interface with the BT1 QC.	112

## List of Figures (continued)

	Page
Figure 6.2-7. Microstructure of Fe26Cr8Al0.4Y-BT1 diffusion couple after initial 25 hours at 700°C showing the development of the phases at the interface. The FeAl intermetallic phase initially forms at the interface with FeAl <sub>2</sub> composition indicated in the BT1 QC.	113
Figure 6.2-8. Microstructure of Fe26Cr8Al0.4Y-BT1 diffusion couple after 500 hours at 700°C showing the development of the phases at the interface. The FeAl intermetallic phase has thickened with Co substituting into the structure on the BT1 QC side of the interface. FeAl <sub>2</sub> begins to form on the BT1 QC side of the interface and the aluminum diffuses into the iron bond coat as solid solution.	114
Figure 6.2-9. Microstructure of Ni31Cr11Al0.6Y-BT1 diffusion couple after initial 25 hours at 900°C showing the development of the phases at the interface. The NiAl intermetallic phase forms at the center of the interlayer phase with Al <sub>3</sub> Ni <sub>2</sub> and Al <sub>5</sub> Co <sub>2</sub> forming to the left of the interface due to the relative increase in Co content as the Al diffuses into the bond coat. AlNi <sub>3</sub> forms initial forms in the bond coat until enough Al diffuses into the coating from the interface.	115
Figure 6.2-10. Microstructure of Fe26Cr6Al0.4Y--BT1 diffusion couple after initial 25 hours at 900°C showing the development of the phases at the interface. The FeAl intermetallic phase form at the center of the interlayer phase with FeAl <sub>2</sub> and Al <sub>5</sub> Co <sub>2</sub> formation to the left of the interface as Al diffuses into the interface increasing the relative Co content. Aluminum diffuses into the iron-based bond coat as solid solutions to the right of the interface.	116
Figure 6.2-11. Microstructure of SAE 1040-BT1 diffusion couple after initial 25 hours at 900°C showing the development of the phases at the interface. The FeAl intermetallic phase form at the center of the interlayer phase with FeAl <sub>2</sub> and Al <sub>5</sub> Co <sub>2</sub> formation to the left of the interface as Al diffuses into the interface increasing the relative Co content. Aluminum diffuses into the steel substrate as solid solutions to the right of the interface.	117
Figure 6.3-1. The average diffusion coefficient ( $D_{i,C}$ ) for nickel or iron for current work compared to prior work of Hirano et al. [56] showing lower values.	119

## List of Figures (continued)

	Page
Figure 6.4-1. Higher magnification of graded TBC structure shown in Figure 1-1 showing the metallic graded phase (white areas indicated by arrows) to be on the order of 5 to 10 $\mu\text{m}$ in thickness.	120

## List of Tables

	Page
Table 2.4-1. Diesel engine performance shows approximately 5% decrease in specific fuel consumption (SPC) using a sealed thick TBC (TTBC). TTBC was 3.5 mm thick.	13
Table 2.4-2. Operating temperatures and stress states comparison between diesel turbine engines.	15
Table 3.1-1. Thermal properties (room temperature) of quasicrystal (QC) alloys (Al-Cu-Fe icosahedral phase and the $Al_5Co_2$ type of approximant of the decagonal Phase) and other materials [4, 35]	28
Table 4.1-1. Nominal compositions of the bond coatings and quasicrystal material used in the study	32
Table 4.1-2. Samples sprayed for diffusion study	33
Table 4.3-1. Exposure temperature and times for the BT1 diffusion couples	35
Table 4.4-1. Polishing procedure used for quasicrystal coatings	36
Table 4.4-2. Elements, x-ray lines, WDS crystals and standards used for microprobe analysis.	37
Table 5.1-1. Quasicrystal powder, BT1, composition via ICP/AES analysis	46
Table 5.2-1. Experimental runs used to determine the parameter set to spray the BT1 quasicrystal alloy with high deposition efficiency.	49
Table 5.4-1. Average microprobe analysis (MP) of the BT1 QC, SAE 1040 substrate, and bond coat materials are shown. The BT1 QC microprobe analysis agrees well with the ICP analysis shown in Table 5.1-1 for the elements included in the analysis. The substrate and bond coat analysis also agrees well with the nominal compositions specified for the materials.	61
Table 5.5-1. Interlayer thickness measured from SEM photos at magnifications up to 300X.	79
Table 5.5-2. Interlayer thickness from microprobe analysis	82
Table 5.5-3. Fit of the Interlayer Thickness to Equation 1 and Extrapolation to 10,000 hours	82

## List of Tables (continued)

	Page
Table 5.5-4. Extrapolated interlayer thickness at 300°C and 400°C	83
Table 5.6-1. Average interdiffusion coefficients for the four types of diffusion couples at the three temperatures and three times.	92
Table 5.6-2. Linear equation fits to the diffusion data in Figure 5.6-7 and 5.6-9 are shown below. The second equation for the aluminum diffusion coefficient in the SAE 1040 couple represents the fit for the 500°C to 700°C only.	95
Table 5.7-1. Aluminum penetration depths calculated from predicted $D_{i,C}$ compared with measured penetration depth at 500 hours measured by SEM photomicrographs.	96
Table 6.1-1. The relationship of the Vickers and spherical modulus to changes in the model parameters $E_0$ , $V_{OPEN}$ , and $V_{SLIDING}$ . The modulus shown is the average of all samples at each temperature. $E_0$ affects the Vickers modulus while both $V_{OPEN}$ , and $V_{SLIDING}$ affect the spherical modulus.	102
Table 6.2-1. Interdiffusion flux nickel, iron and aluminum for the couples are shown for selected temperatures and times. A negative flux represents movement toward the BT1 and a positive flux is toward the bond coat or substrate.	106

## **Acknowledgements**

I would like to acknowledge the financial support from the Department of Energy, Assistant Secretary for Energy Efficiency and Renewable Energy, Office of Transportation Technologies as part of the Ceramic Technology Project of the Materials Development Program, under contract FC05-97OR22580.

I would also like to acknowledge the financial support of Caterpillar Inc. and the support of the management of Caterpillar for allowing me the time to complete this study.

My thanks to my Caterpillar colleagues, Otto Rajtora, Dr. Jason Sebright, Dr. Ondrej Racek and Dr. Elmer Zanoria for their support and encouragement to finish.

## 1.0 Introduction

The development of thermal barrier coatings (TBCs) for use in diesel engines is driven by the same issues that have resulted in their applications in turbine engines: increased engine efficiencies derived from higher engine operating temperatures and lower heat rejection. TBCs applied to diesel engine components such as pistons and cylinder heads will allow higher combustion pressures and temperatures, while reducing overall heat loss to the coolant, with direct benefit to the engine performance and efficiency. Diesel engines will require high TBC durability to allow maintenance and trouble free engine use. Routine engine inspection and overhaul for turbine engines are typically much lower than the 15,000 hour or 1 million mile overhaul intervals now expected of diesel engines.

Thermal barrier coatings have been used in aero-turbine engine applications since the mid-1960s [1]. TBCs usually consist of a metallic bond coating beneath a top coating of a low thermal conductivity ceramic, usually zirconium oxide, Figure 1-1. The bond coating material provides for oxidation protection of the substrate at high temperatures, as well as strain compliance to mitigate the difference in thermal expansion between the substrate and the lower expansion zirconia. Zirconia, usually stabilized with 7-8% yttria to prevent undesirable phase transformations, is used due to its low thermal conductivity (2 to 2.5 W/m-K vs ~50 W/m-K for steel) and relatively high thermal expansion (~9 mm/mm/C vs ~12 mm/mm/C for steel). Thermal conductivity of the zirconia is reduced further by the introduction of porosity and microcracking during coating application (0.5 to 1 W/m-K), Figure 1-2. Coatings of this type are typically applied by plasma spraying. Zirconia top coats are also applied via physical vapor deposition, but are much thinner than those applied by plasma spraying (0.1 to 0.2 mm vs. 0.25 to 1 mm) and have higher initial thermal conductivities (1 to 1.5 W/m-K) due to their dense, columnar structure, Figure 1-3.

Relatively new families of metallic materials known as quasicrystals (QCs) have unique properties [2] that may provide advantages in their use as thermal barrier coatings over current ceramic materials. Quasicrystals have well ordered atomic structures but are aperiodic in that they do not have simple lattice structures that repeat. This leads to rotational crystal symmetries that do not fit classical crystallography rules. The reported low thermal conductivity of QC materials (1 to 6 W/m-K) could provide for good insulating properties while their high thermal expansion coefficient (14 to 19 mm/mm/C) may allow for reduced stress states due to lower expansion mismatch between the coating and metallic substrates. In addition, the intrinsic high-temperature deformation behavior of quasicrystalline materials provides a unique ability to accommodate strain at high

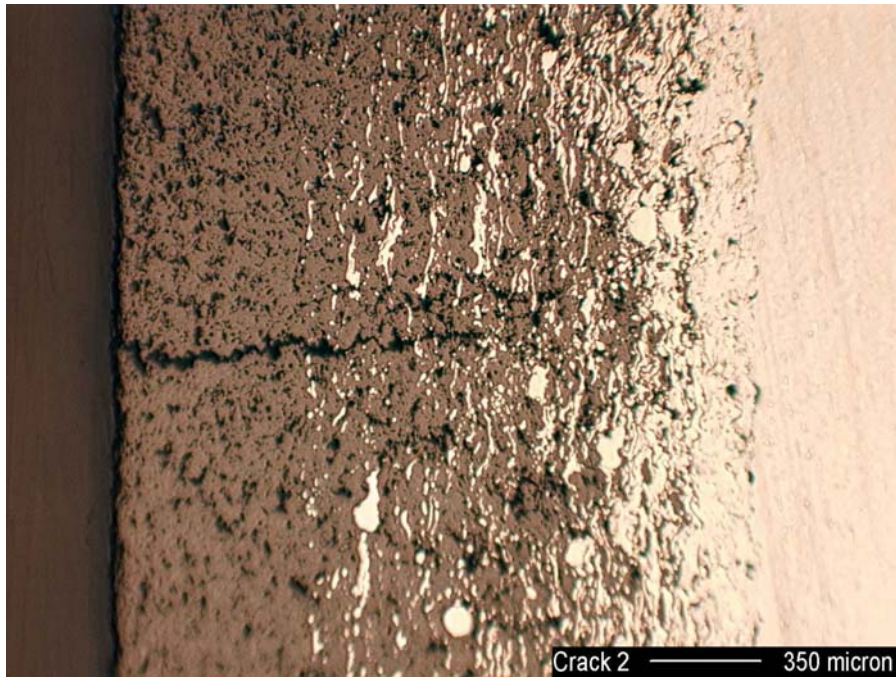


*Figure 1-1. Typical microstructure of a graded TBC applied to diesel engine components showing the 100% zirconia top coating (left), center graded section of zirconia and bond coating, and bond coat/substrate interface (right). The crack resulted from thermal stress induced during engine testing.*

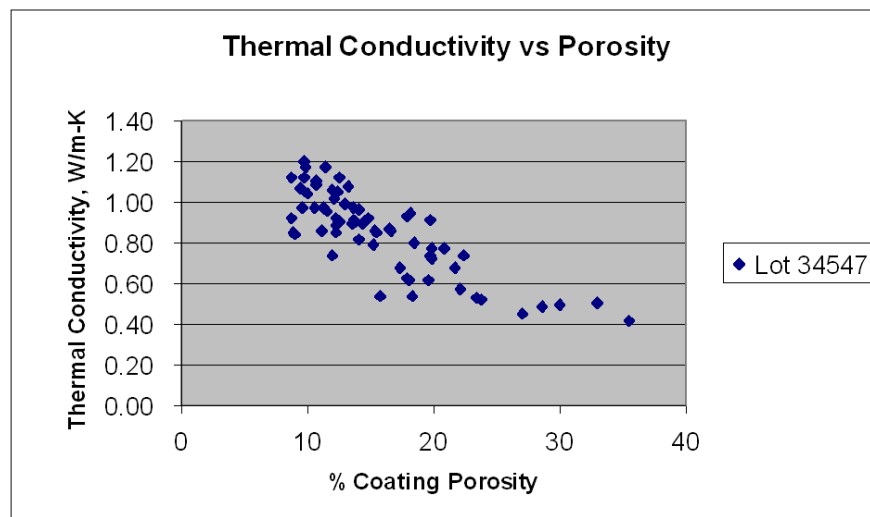


*Figure 1-2. Thermal conductivity of a zirconia TBC as a function of coating porosity from internal data at Caterpillar.*

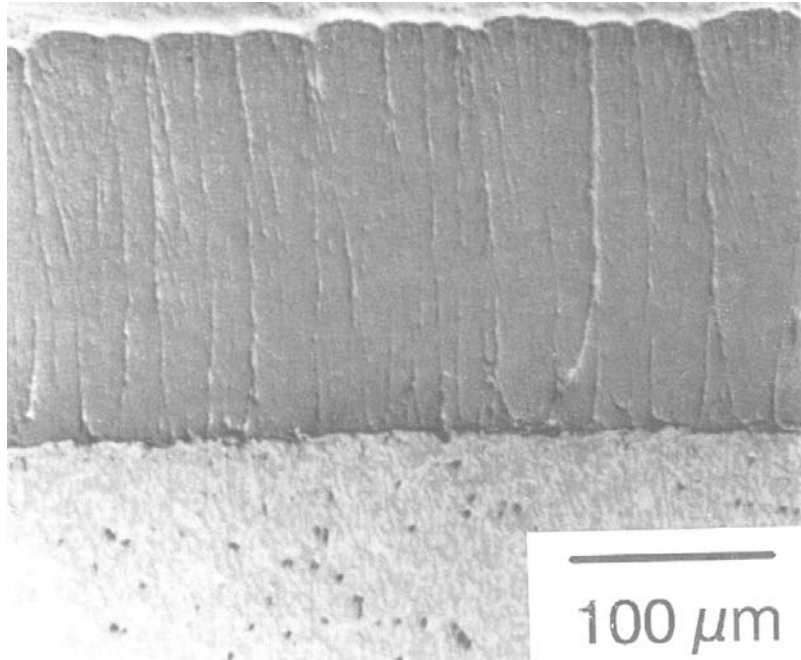


*Figure 1-3. Microstructure of a PVD deposited zirconia TBC used in turbine applications showing the columnar structure of the coating [1].*

temperature [3]. Specifically, plastic deformation that is not recoverable on cooling to room temperature may be detrimental if high stresses on cooling are formed. One type of QC approximant, with the stoichiometry  $\text{Al}_{71}\text{Co}_{13}\text{Fe}_8\text{Cr}_8$ , has been previously investigated for use as a TBC in aero turbines and will be the material used in this work [4, 5]. This alloy was reported to have a bulk thermal conductivity similar to that of zirconia and was shown to have good high temperature oxidation.

The overall goal of this project is to assess and understand the high-temperature behavior of quasicrystalline approximant,  $\text{Al}_{71}\text{Co}_{13}\text{Fe}_8\text{Cr}_8$ . The structure and properties of coatings created using HVOF spraying of this approximant will be studied. The specific aims of this program are to:

- 1) Deposit quasicrystalline approximant coatings using the HVOF process.
- 2) Assess the structures and compositions of the coatings.
- 3) Determine the stability of coatings after exposure at high temperatures.
- 4) Characterize the mechanical properties of the coatings by instrumented micro-indentation techniques.

## 2.0 Thermal Barrier Coating Background

Thermal barrier coatings have been developed using both thermal spray and physical vapor deposition techniques (PVD). PVD coatings require vacuum chambers for the process and are relatively thin compared to thermal spray coatings. For this study, thermal spraying will be the method to produce the quasicrystalline TBC systems. A review of the thermal spray processes used for TBCs follows as well as a background on TBC application to turbine and diesel engines.

### 2.1 Thermal Spray Processes

Thermal spraying can be thought of in terms of “hot” painting. Thermal spraying consists of using a heating source created by combustion gases or electric arc plasmas to heat and accelerate a gas that then is used to heat and/or melt the material to be sprayed [6]. If the material is in a rod or wire form instead of a powder, the spray system must also atomize the material into small droplets for spraying. Ceramic thermal barrier coatings were first produced using Rockide type spray systems [1,6], in which combustion of oxygen and acetylene melt and atomize a solid rod of ceramic, Figure 2.1-1. Materials were limited to those with melting points lower than the combustion temperature of acetylene and that could be fabricated into suitable feed rods. The introduction of plasma spray systems allowed for the spraying of any material, particularly high-melting point ceramics, in the form of powder. Plasma spraying is particularly suited for producing the ceramic layer of the TBC due to the high temperature ( $>10,000^{\circ}\text{K}$ ) and enthalpy of the plasma, allowing virtually any material to be melted. Due to the low velocity of the plasma spray process, it does produce relatively high porosity. Although porosity is intentionally introduced into the ceramic TBC layer in order to reduce its thermal conductivity [21], porosity is detrimental to the ability of the bond coating to protect the substrate from oxidation. New high velocity oxygen-fuel (HVOF) systems have been introduced which create higher density oxidation resistant coatings and have been applied in advanced TBC systems for application of the bond coating.

Plasma Spraying - There are several different configurations of plasma spray torches, but all are basically similar in operation, Figure 2.1-2 [6]. The torch consists of a water-cooled electrode and anode with the anode in the form of a nozzle through which the inert plasma gas (usually nitrogen or argon) flows. A DC electric arc is struck from the electrode to the anode through the gas, creating the plasma. The amperage of the plasma is controlled via the power supply, and the voltage is controlled by the introduction of a secondary gas,

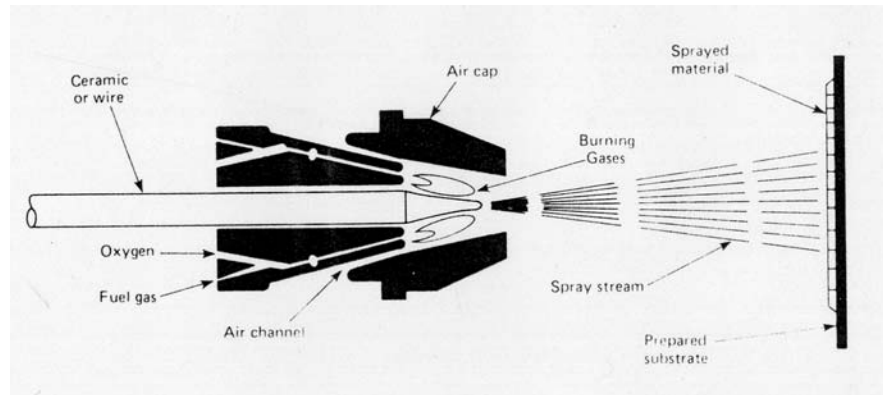


**Figure 2.1-1. Schematic of Rockide type spray torch showing rod feedstock and air cap arrangement for melting and atomizing the material [6].**

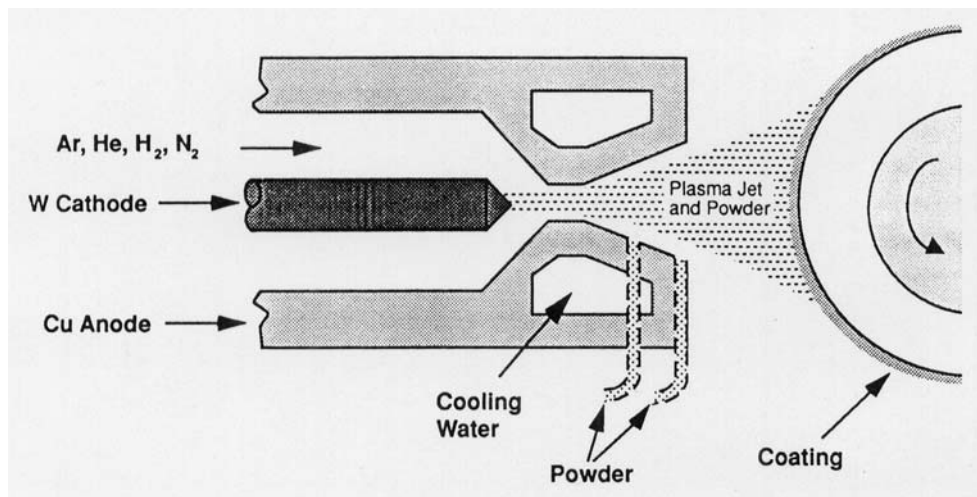


**Figure 2.1-2. Schematic of a plasma spray torch showing the basic electrode/anode and gas arrangement of a typical DE plasma system. Powder is injected either internally or external of the nozzle [6].**

such as hydrogen or helium, which changes the enthalpy of the plasma and raises voltage and thus power of the plasma. The feedstock (powder) is introduced into the plasma either through internal passages in the nozzle or externally. The velocity of the gas in the plasma accelerates and heats the powder, projecting it onto a prepared component surface. The surface to be sprayed is prepared by cleaning to remove all oil/grease/dirt and is roughened usually by grit blast. The roughened surface allows the melted material to solidify around the asperities and hence lock the coating into place. Due to the relatively small mass of the powder particles compared to the mass of the substrate, the former are subjected to very high cooling rates and no detectable melting of the surface occurs. Therefore, the coating

adherence is by mechanical locking onto the roughened surface with minimal metallurgical bonding via interdiffusion.

Thermal spraying can be done in inert atmospheres and under partial vacuums (low pressure plasma spraying or LPPS), but this raises cost due to the capital expense for chambers and high cycle times for loading and unloading the chamber. For this study, atmospheric HVOF spray process will be used for the coating application. The higher porosity of a plasma sprayed coating does result in a lower thermal conductivity than the bulk material being sprayed but the porosity also decreases strength. To date, plasma spray processing of TBC systems has concentrated on the development of low thermal conductivity. Due to the need for higher durability in diesel engine applications, the ability to use HVOF processes to spray quasicrystalline materials with the higher strength of HVOF coatings is attractive.

**HVOF Spraying** - High velocity oxygen-fueled (HVOF) torches use the combustion of a fuel and oxygen, and a nozzle configuration that provides for supersonic gas velocities, Figure 2.1-3 [6]. As with plasma torches, several different configurations are available, most differences having to do with what type of fuel is used. Torches that burn liquid fuel such as kerosene have different combustion chamber designs than those that burn gases, and some torches are designed to burn both liquid and gaseous fuels. In all configurations, the point of the process is to channel the combustion gas products through a nozzle to accelerate the gas to supersonic velocities. The resulting flame is similar to that of a jet engine. The material to be sprayed is injected into the spray system, accelerating it to high velocities and projecting it

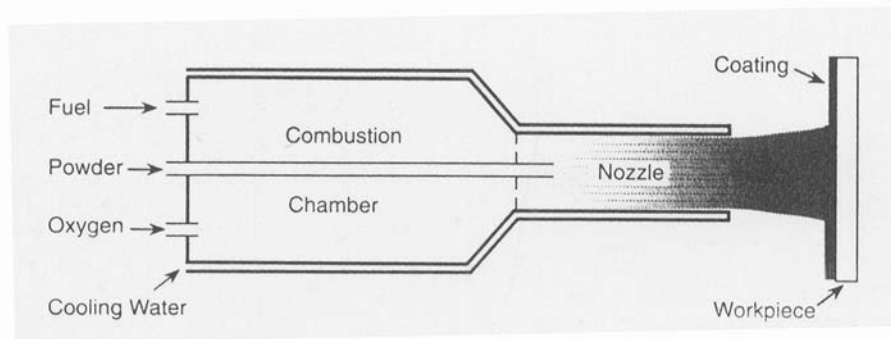


**Figure 2.1-3. Schematic of a HVOF torch showing the combustion chamber and nozzle arrangement with axial powder injection. Some torches use converging/diverging nozzle designs in increase gas velocity [6].**

onto the substrate as in plasma spraying. The velocity of the particles in HVOF spraying are typically in the 500 to 700 m/sec range, compared to 200 to 400 m/sec for the plasma spray process. This higher velocity is due to the nozzle design and the use of high flow rates of the combustion gases. The advantage of the HVOF process over plasma spraying is that the higher particle velocity imparts higher kinetic energy to the particles and results in high energy on impact with the substrate. This results in greater particle adherence and higher coating densities. Due to the high velocity, the dwell time of the particle in the hot gas is short, and the particle temperature is therefore lower than in plasma spraying. This is advantageous when spraying metallic or carbide materials due to minimized oxidation at the lower spray temperature, but also limits HVOF processing to materials with lower melting points. This prevents HVOF spraying of most ceramic materials, particularly zirconia. A major advantage of the quasicrystalline materials based on aluminum is that their lower melting points will allow them to be processed via HVOF. This will result in higher strength TBC coatings with higher adherence to be produced than can be done using plasma processing. Although HVOF processing results in a denser coating, the thermal conductivity of an HVOF sprayed alumina has been shown to be close to that of plasma spray [22]. This is thought to be due to the crack density and orientation of the cracks in the HVOF coating.

## **2.2 History of Thermal Barrier Coating Applications to Turbine Engines**

The need for increased turbine efficiencies and performance was evident from the first jet engine flights. A major limitation on the design of higher performance engines was the high temperature strength of materials used in the hot section of the engine. Concentrated research and development activities resulted in a steady improvement in high temperature alloys, leading to the development of the current class of high-temperature nickel based alloys that can be used up to about 0.8 of their melting temperature, as indicated in Figure 2.2-1 [7]. As these alloys have been under development, alternate methods to provide for increased temperature capabilities were also investigated, leading to the development of thermal barrier coating (TBC) systems.

Initial coatings used in turbines during the late 1940's to 1950 were ceramic glass coatings applied to reduce oxidation of the alloys and extend the temperature range of operations. Initial trial TBC systems were based upon alumina and zirconia. The relatively high thermal conductivity of alumina, and phase transformations from the metastable alumina structures produced during thermal spraying to the stable alpha structure at high temperatures, limited its use. Zirconia, initially stabilized with calcia and magnesia, proved

to have better durability and lower thermal conductivity, allowing the use of thinner coatings. It is thought that the first thermal barrier used in flight was a calcia- zirconia flame sprayed coating on the rocket exhaust of the X15 experiment aircraft [1]. One of the first commercial uses was by Pratt and Whitney, a two-layer coating of 22% magnesia-stabilized zirconia with a nickel-aluminum bond coating used on turbine combustors beginning in 1963 [8].

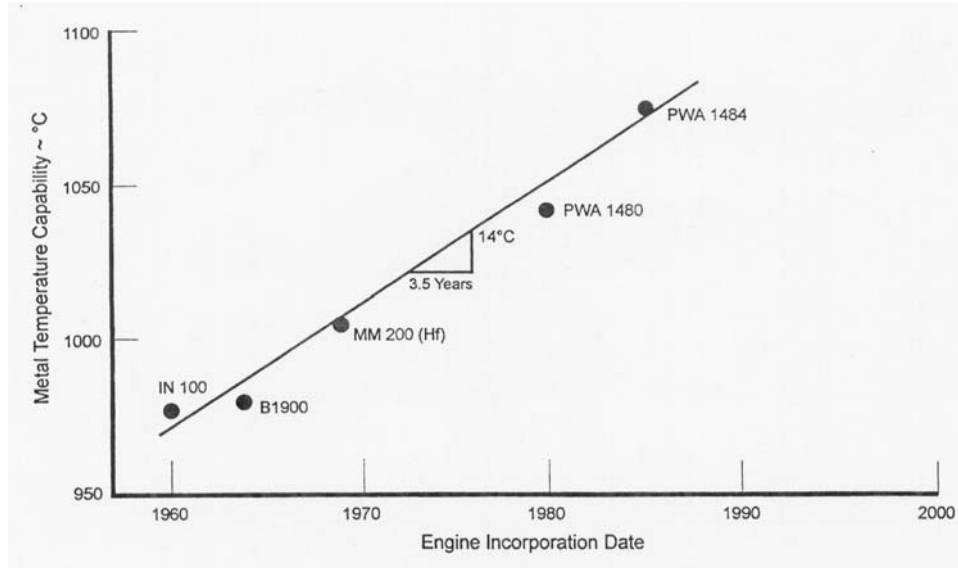


**Figure 2.2-1. Timeline for the development of high temperature superalloys for turbine applications showing the continued improvement in high temperature capability of the alloys [7].**

Initial TBC ceramic materials were flame sprayed using processes such as the Rockide process, which uses a combustion flame to melt a rod of the ceramic material [1]. This limited the types of materials that could be sprayed to those that could be easily fabricated into rods. The development of the plasma arc torches (initially developed for low thrust plasma engines and used for tests related to vehicle reentry) provide for a very high heat source that allow for a wide range of materials in the form of powders to be sprayed [1].

The beginning of the “modern era” of TBCs began when NASA Lewis Research Center (now Glenn Research Center) successfully demonstrated high durability using a 12% yttria-zirconia with a Ni-Cr-Al-Y bond coating on turbine blades in the mid-1970’s [1]. This success was attributed to the two-layer bond coat/top coat structure with use of yttria stabilization of the zirconia for higher temperature stability and the highly oxidation resistant Ni-Cr-Al-Y bond coating material developed by NASA. The two-layer structure was an improvement over prior attempts to use graded structures of metal and ceramic in the coating

design due to the oxidation of the metal in the graded layer at the high temperatures found in the turbine applications ( $>1100$  C). The M-Cr-Al-Y type bond coatings have been extensively studied over a range of compositions, where the major constituent, M, is nickel, iron, cobalt, or a combination of these elements [9]. Ni-Cr-Al-Y has been widely used due to its compatibility with the nickel superalloys used in turbine engines. The nickel content of these coatings is in the range of 60% to 70%, chromium is in the range of 20% to 30%, aluminum is in the range of 6% to 10% and yttria is 0.5% to 2%.

The success of thermal barrier coating systems of this type has allowed the combustion temperatures of modern land-based turbine engines to be increased to where the peak surface of the thermal barrier coating is in the range of  $1200^{\circ}$  C, while keeping bond coat/substrate temperatures in the proximity of  $1000^{\circ}$  C [68]. Advanced cooling methods have also been developed to provide for increased combustion temperature capability.

The use of graded coating systems was not successful in turbine applications due to the oxidation of the bond coating materials when exposed to the high temperatures found in the hot section of turbines. Graded coatings consist of layers containing varying percentages of ceramic and bond coating material. The number of graded layers and the bond coat/ceramic ratio used in each layer can be varied to achieve different stress states in the final coating layer. This is due to the change in thermal expansion as the bond coat/ceramic ratio changes. Although the use of graded coatings in the hot section of the engine proved not to be successful, their application to lower temperature areas of the engine, such as tip seals, were successful and provided the basis for TBC systems developed for diesel engine applications, Figure 1-1 [10].

### **2.3 Advanced Thermal Barrier Coating Systems**

Current development of both advanced plasma sprayed and PVD type coatings in aero and land-base gas turbines has concentrated on increasing the durability of the coatings, while maintaining or increasing their insulation capability. New ceramic materials with lower thermal conductivities and longer-term stability at high temperatures have been introduced aimed at achieving these two goals. At the same time, there has been an increasing recognition that the requirements of the two applications (aero vs. land based power generation turbines) in regard to load cycles and peak temperatures are significantly different to the extent that different approaches to coating design and materials are required [11]. Major efforts current underway to develop new materials with lower thermal conductivity than zirconia and/or better high-temperature stability, as well as programs to

better understand material properties and the degradation of properties with time at temperature [12-16].

Durability and stability of TBCs have been key issues since their first use. Low durability of TBCs has dictated that their life cycle be predicted in order that inspection of the coated components can be scheduled at intervals to allow for overhaul and replacement of the coatings after failure [7]. This initially limited the use of TBCs to high-performance military engines where the expense of additional inspections could be justified. The use of TBCs in land-base gas turbines and commercial aircraft has only recently begun and long-term durability of the coatings is a critical issue. New methods to predict the long-term behavior of TBC systems are under development [11, 13,17,18,25,28].

Typical methods for assessing the durability of TBC systems have relied on the use of burner rigs to thermal cycle the coatings at or near engine temperatures [1]. Burner rigs of the type shown in Figure 2.3-1 have proven to be quite capable of imposing surface temperatures and temperature gradients on samples similar to those experienced by the TBC in engine operation. This type of thermal cycling has proven useful in development of better bond coating materials for oxidation protection and was used in the development of the current yttria-stabilized zirconia topcoat. Use of high temperature exposure has also shown the need for better stability in the zirconia top coats due to sintering effects that increase its thermal conductivity from the as-applied state. This has been shown to be true for both plasma sprayed and PVD zirconia coatings and has led to the investigation of novel insulating materials with the potential for greater high temperature stability [12-15]. In addition to increasing the thermal conductivity of the coating, thermal cycling has also been shown to cause sintering effects that change the mechanical properties of the coating [17].

A major limitation of the use of rig testing to assess TBC systems has been the lack of good correlation of rig life cycles to engine cycles. A factor of two increase in rig cycling cannot be used to predict similar life increases in actual engine use. This has resulted in a lack of good prediction of long-term durability for use in land base gas turbines and a lack of fundamental material property data base for design of coatings [16]. One promising test method is the use of a laser rig developed by NASA Glenn Research Center for imposing high thermal gradients on TBC systems that simulate engine conditions [18].

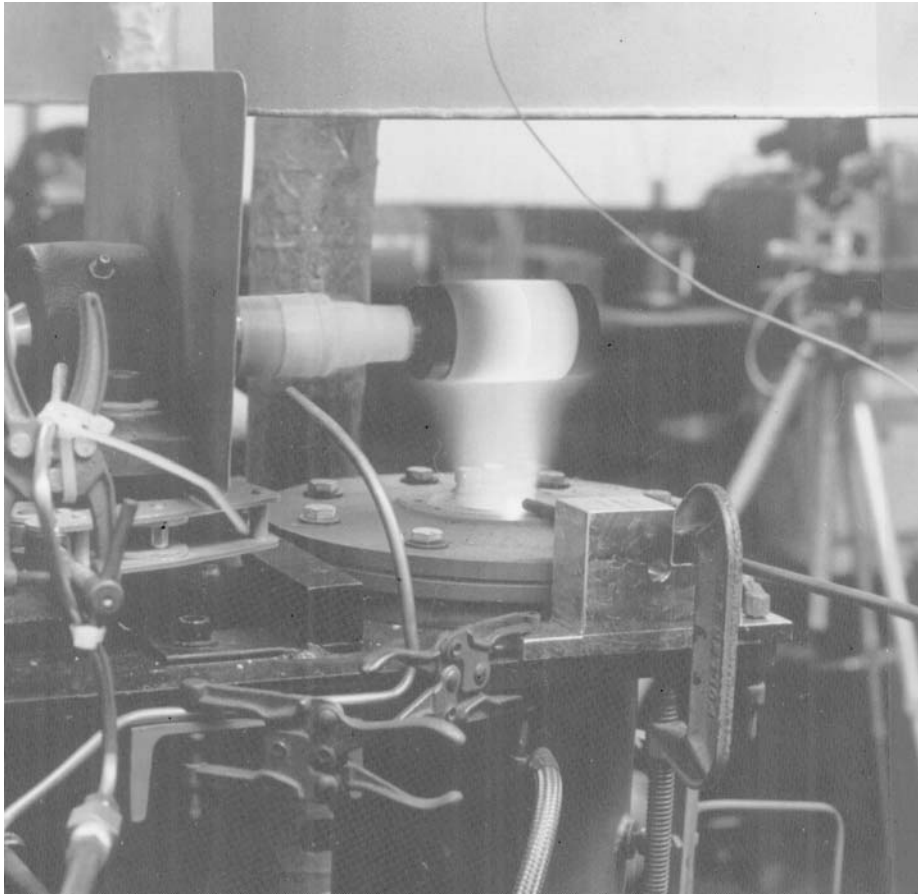


*Figure 2.3-1. Gas burner rig for heating of TBC samples to similar temperature ranges as found in turbine engines [18].*

## **2.4 Application of Thermal Barrier Coating Systems to Diesel Engines**

Initial interest in applying TBC systems to diesel engines began in the mid-1980's with the recognition of the benefits of lower component temperatures and the effect of lower heat rejection on engine performance [16,19]. The initial claims for the benefits of insulating piston and head components with thin TBCs similar to that used in turbine engines were substantial decreases in fuel consumption and heat rejection. However, these claims proved to be somewhat misleading, and benefit gains for applying TBCs with thickness of 0.5 mm or less are difficult to measure in laboratory engine testing. Even so, there were demonstrations of the benefits of reduced component temperature on extending service life, particularly where high temperatures and poor fuel quality lead to corrosive attack [20]. Exhaust valves



**Figure 2.4-1. Diesel engine exhaust valves coated with a 0.5 mm thick zirconia TBC to lower valve face temperature to prevent attack by liquid vanadium pentoxide [22].**

in residual fueled engines are specific examples where Caterpillar has applied thin (0.5 mm) thermal barrier coatings to enhance the durability of engine components, Figure 2.4-1.

Benefits from using thicker thermal barrier coatings based on zirconia were in dispute until the demonstration by Caterpillar of the benefits of insulating the combustion chamber, Table 2.4-1 [21]. This work used a 3.5 mm thick graded coating of zirconia and a NiCrAlY bond coating to achieve thermal conductance of  $400 \text{ W/m}^2\text{-K}$ , equivalent to 2.5 mm thickness of a zirconia coating with a thermal conductivity of  $1 \text{ W/m-K}$ . A fuel consumption reduction of 4.9% was demonstrated but durability of the coatings was limited to approximately 100 hours. The failures of the coatings in this testing were determined to be due to bending stresses caused by the high thermal gradients in the coatings and the bending loads caused by the combustion process, Figures 2.4-2 and 2.4-3.

Thermal barrier coatings for diesel engines continue to be of interest due to the high benefit in engine efficiency and the continued rise in component temperatures in advanced engine designs, Table 2.4-1. The lower temperatures of the diesel allow the use of graded designs without the concern for accelerated oxidation. Changing from a two-layer coating design on engine valves to a graded coating design with similar thermal resistance increased

**Table 2.4-1. Diesel engine performance shows approximately 5% decrease in specific fuel consumption (SPC) using a sealed thick TBC (TTBC). TTBC was 3.5 mm thick.**

		Water Cooled Baseline	Unsealed TTBC	Sealed TTBC
Recip BMEP	KPa	1427	1411	1406
Air Flow	Kg/hr	274	288	249
Vol Efficiency	%	85.5	81.3	80.3
Air/Fuel Ratio		30.4	30.3	29.5
Peak Cyl Press.	MPa	16.0	16.0	16.0
Recip SFC	G/kW- hr	217.1	231.7 (+6.7%)	206.5 (-4.9%)
Recip SHR	KW/KW	0.479	0.499	0.399

Data from Caterpillar's final report for Thick Thermal Barrier Coatings for Diesel Components,  
DOE/NASA/0332-1, NASA CR-190759, August 1992

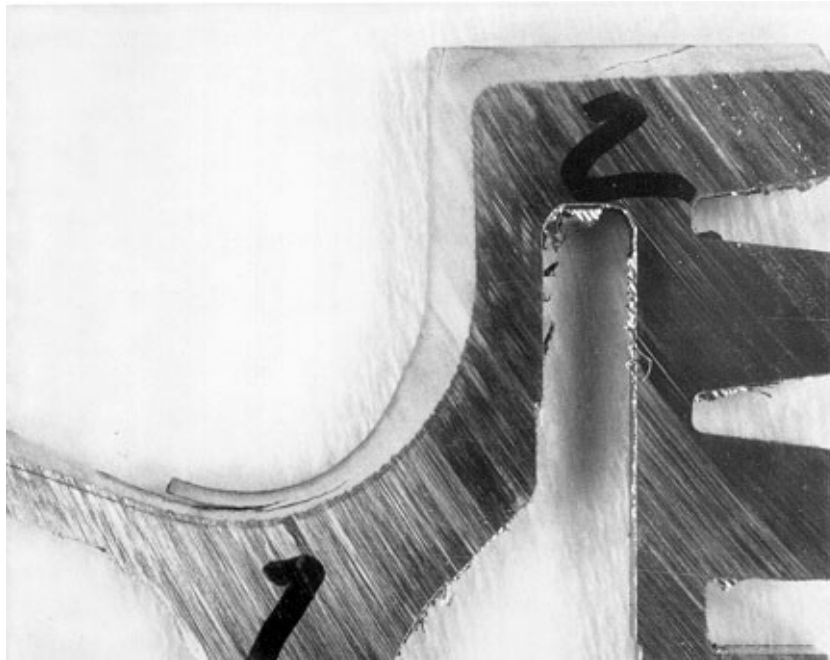


**Figure 2.4-2. Cross section of a TBC piston after engine testing showing the cracking in the coating caused by the bending stress in the bowl area and high compressive stress on the top land [22].**

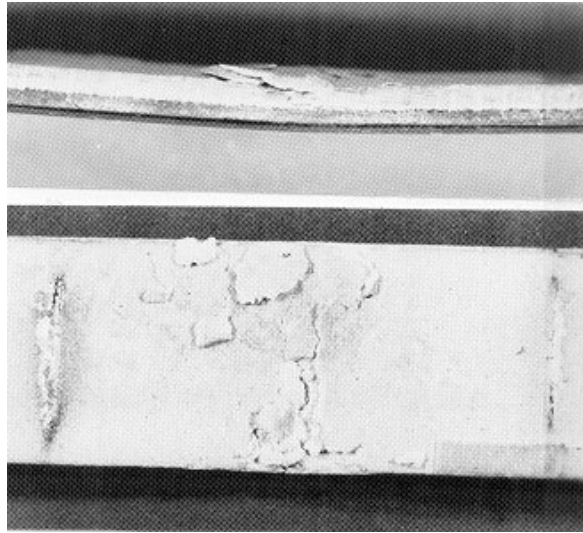


*Figure 2.4-3. Bending fatigue sample of ceramic layer of TBC showing spalling failure similar to that of the TBC piston shown in Figure 2.4-2. [24]*

the coating life on diesel engine valves from 2000-3000 hours to 5000-6000 hours [22]. However, customer expectations are that engines run for 15,000 to 20,000 hours prior to overhaul, so further increased durability of the TBC is required.

Component temperatures in the range of 600 to 1000° C result from the high efficiency of the water cooling systems in diesel engines, together with the discontinuous combustion process of the diesel. Typical component temperatures for diesel engines are summarized in Table 2.4-2. The lower temperature of diesel engine components has allowed the use of graded coatings, particularly for the head and valve components. Piston temperatures are high enough that care must be taken in the design of the coating to make sure that the metallic component of the graded layers are not exposed to the higher temperatures. A typical temperature prediction for a TBC coated piston in an advanced diesel engine is shown in Figure 2.4-4. Cylinder head temperatures would be lower due to the higher cooling efficiency of the water jacket in the head versus the oil jet spray that cools the underside of the piston.

Additionally, the requirement for relatively high insulation to gain the benefits for applying TBCs to diesel results in major differences in operating environments from that of turbine engines. In addition to the peak operating temperatures, temperature gradient differences resulting from the heat load and insulation required (TBC thickness) and the mechanical loading found in diesels due to the high compression pressures combine to result in high compressive stress states not found in thin turbine TBCs. This has resulted in

relatively low hours to failure for diesel TBC applications, ranging from less than 100 hours for high performance piston applications to 2,000 to 3,000 hours for less highly stressed applications, such as engine valves. One method to reduce the stress in the coating is to reduce the thickness or increase the thermal conductivity of the ceramic, thereby reducing the temperature gradient and reducing the imposed stress state. However, this reduces the benefit of the applied coating, making it economically impractical to use.

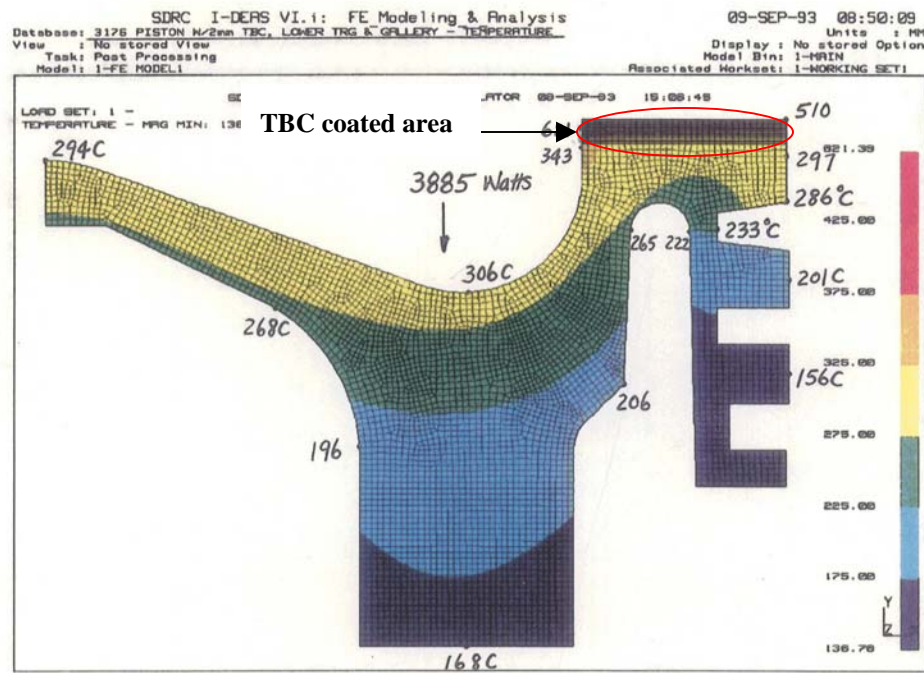


**Figure 2.4-4. Finite element analysis of TBC and piston substrate showing temperatures under peak load conditions [22]. TBC coating on top land only as indicated.**

**Table 2.4-2. Operating temperatures and stress states comparison between diesel turbine engines.**

Engine Type	Peak Surface Temperature	Temperature Gradient Through Coating	Relative Mechanical Stress
Diesel, 1 mm TBC	700 C	200 C	20% of thermal stress
Diesel, 3.5 mm TBC	800 C	400 C	30% of thermal stress
Turbine	1260 C	150 C	10% of thermal stress

The issue of TBC durability is further complicated by the need for seal coatings to reduce the influence of the porosity in the ceramic coating to interact with the combustion process. It is thought that the air/fuel mixture for combustion is forced into the pore structure of the top coating and graded layers on compression and would consequently not be directly available for combustion, thereby lengthening the time of the burning of the fuel and decreasing the overall efficiency of the engine, Figure 2.4-5.

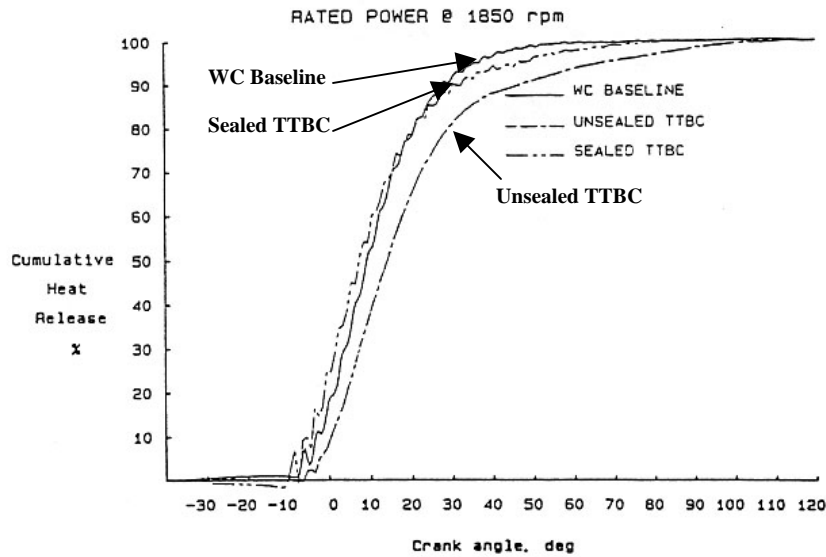


*Figure 2.4-5. Heat release diagram of engine combustion for metal baseline engine, unsealed TBC and sealed TBC engine showing longer heat release time for unsealed TBC engine components [21].*

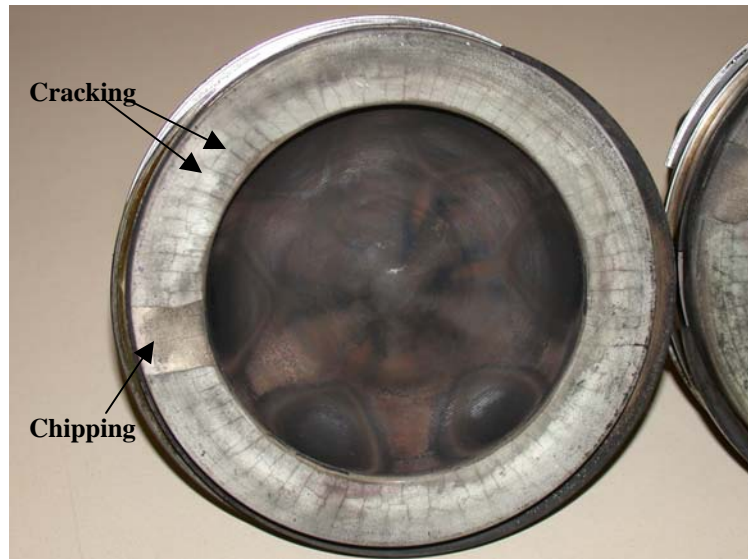


*Figure 2.4-6. Glass composite sealed piston showing cracking and chipping of the glass seal coating after only 100 hours of engine testing [22].*

Various seal coating application methods have been tried, including changing of the spray parameters to create dense ceramic layers on top of the TBC to novel glass structures [23]. Problems encountered with these methods include cracking and chipping of the higher density ceramic layers rendering them ineffective and low-hour failures of the glass-type coatings, Figure 2.4-6.

## 2.5 Failure Mechanisms and Limitations of TBC Systems in Diesel Engines

The major mechanisms of low-hour (<5000 hours) failures identified for TBCs used on diesel engine components are surface-initiated fatigue due to compressive bending loads and surface-initiated tensile failures resulting from creep under compression at operating temperatures.

Compressive bending fatigue failures have been observed in low-hour engine failures and verified by specimen testing. Figure 2.4-2 shows the surface initiated cracking pattern in a zirconia TBC that was engine tested. This failure mode was duplicated in TBC specimens fatigue tested in compression using 4-point bending, indicating that the cyclic compressive stresses generated during the engine test are responsible for the cracks in the piston TBC, Figure 2.4-3 [24]. By varying the mean compressive stress in fatigue, it has been shown that there is a region in the compressive stress range where the coating can be safely cycled, Figure 2.5-1. By designing a graded coating structure to maintain the desired compressive mean stress in the top coating layer, bending fatigue failures can be avoided. [21].

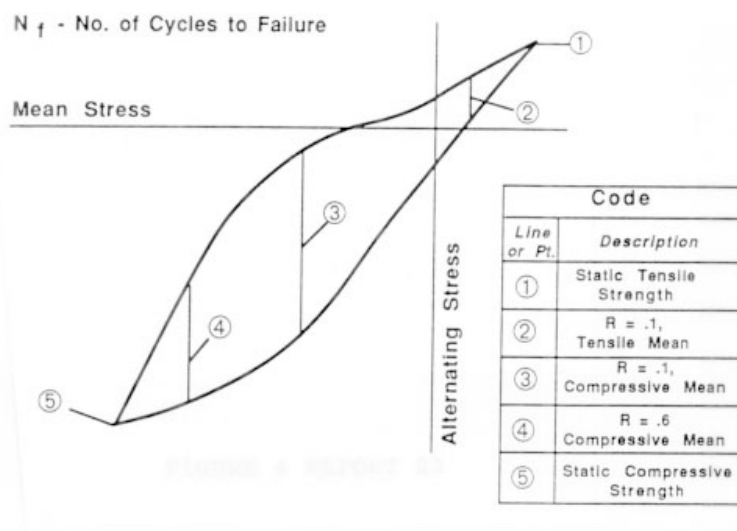
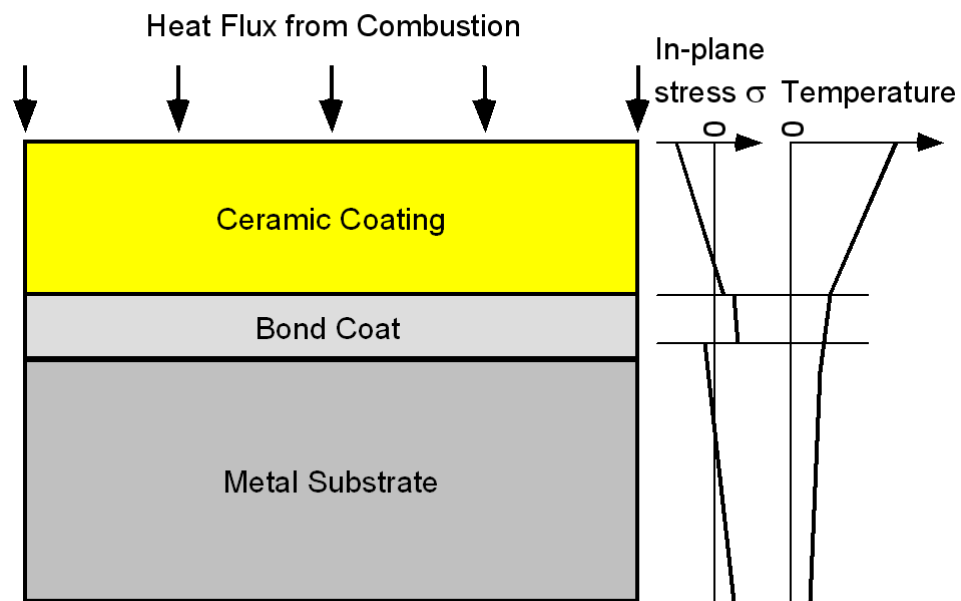


Figure 2.5-1. Goodman type diagram of mean and alternating stress levels for design of TBC systems.

In the combustion cylinder, the surface of the TBC is exposed to a high heat flux which generates high surface temperatures in the coating resulting in compressive stresses in the TBC surface, Figure 2.5-2. Tensile failure results from creep of the coating under compression at high temperature, which induces a tensile stress state on cooling to the original temperature. Gaining an understanding of this failure mechanism has been the focus of work by Dr. Darrell Socie and associates at the University of Illinois using TBC materials and uniquely designed ceramic tube specimens designed and supplied by Caterpillar. This specimen design allows the ceramic material to be loaded in both compression and tension, Figure 2.5-3 [27]. Using this type of specimen, it has been shown that the zirconia-based TBC exhibits a very inelastic stress/strain response and develops hysteresis upon cycling, Figure 2.5-4 [27]. Similar behavior of alumina-, mullite- and calcium titanate-based TBC materials has also been reported [25,26]. The high defect structure of the coating resulting from the plasma spray process is thought to control this behavior. It has been shown that the material exhibits a fatigue behavior similar to that of cast iron, strong in compression and weak in tension. The fatigue limit in compression at room temperature is approximately 200 MPa for a 8% yttria-zirconia while the fatigue limit in tension is less than 10 MPa, Figure 2.5-5 [27]. In order to fully understand the material's behavior under engine conditions, recent focus has been on understanding the creep behavior of the material and its response to thermal-mechanical loading. Creep was initially investigated by holding the specimen at various stress states and temperatures and measuring the resulting strain response. Specimens held in compression at 300 MPa for one hour at 800°C exhibited 60% less strain in compression than specimens held at 50 MPa or lower, Figure 2.5-6 [27]. Additional thermal mechanical studies have shown that loading the zirconia TBC in compression at high temperature can cause sufficient creep of the material that results in tensile strains on unloading sufficient to cause failure, Figure 2.5-7 [28].

Initial thermal mechanical testing of ceramic TBC materials has shown that these materials undergo a high amount of non-elastic deformation when subjected to the temperatures and strains found in diesel engines [18]. It is believed that this behavior is due to the high defect structure (crack density) of the thermal sprayed ceramic material, as well as to sintering effects of the microcracks at high temperature. The behavior of thermal sprayed metallic materials has been shown to be considerably different from that of the ceramic TBCs [22]. The behavior of the former is closer to that of a metallic solid, which explains why metallic thermal sprayed coatings have been used with high success in rebuilt diesel engine components. The thermal gradient, and therefore thermal stress, is also lower for a metallic



*Figure 2.5-2. Schematic of stress state resulting from the applied thermal load on the TBC in a diesel engine. [from E. Redja, University of Illinois]*

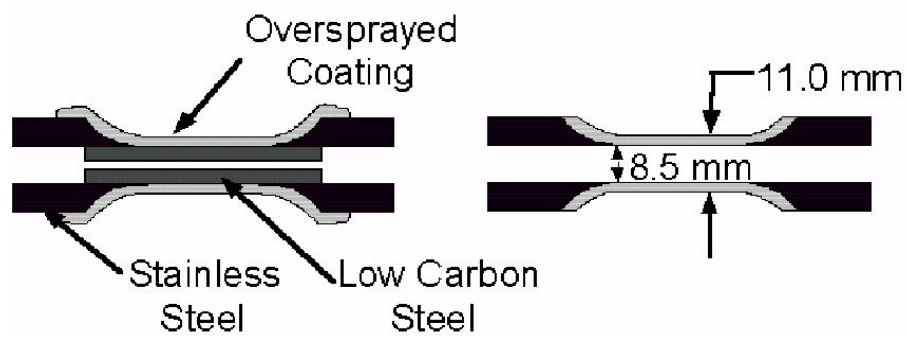


*Figure 2.5-3. Tubular specimen developed by Caterpillar and University of Illinois for testing the ceramic TBC in tension /compression [27].*

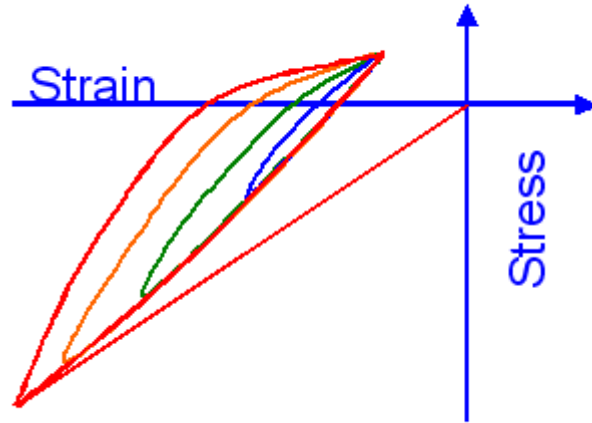


Figure 2.5-4. Stress-strain response of a zirconia TBC tested using the specimen geometry shown in Figure 2.5-3 [28].

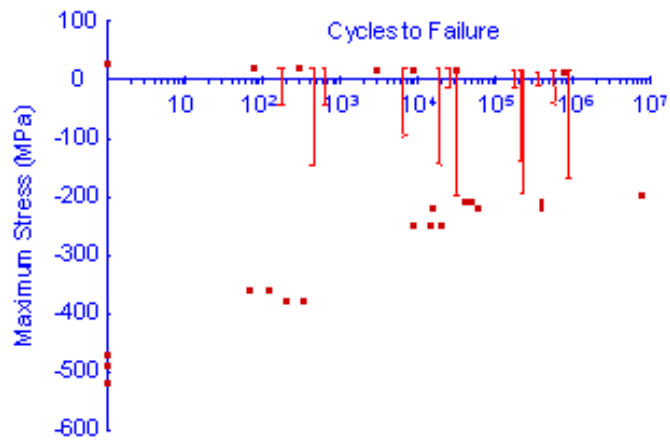


Figure 2.5-5. Fatigue response of ceramic TBC showing high strength in compression and low tensile strength. Data points with mean compressive stress demonstrate that the failure mechanisms in tension and compression do not interact, the failure is either due to the maximum compressive stress or maximum tensile stress [27].

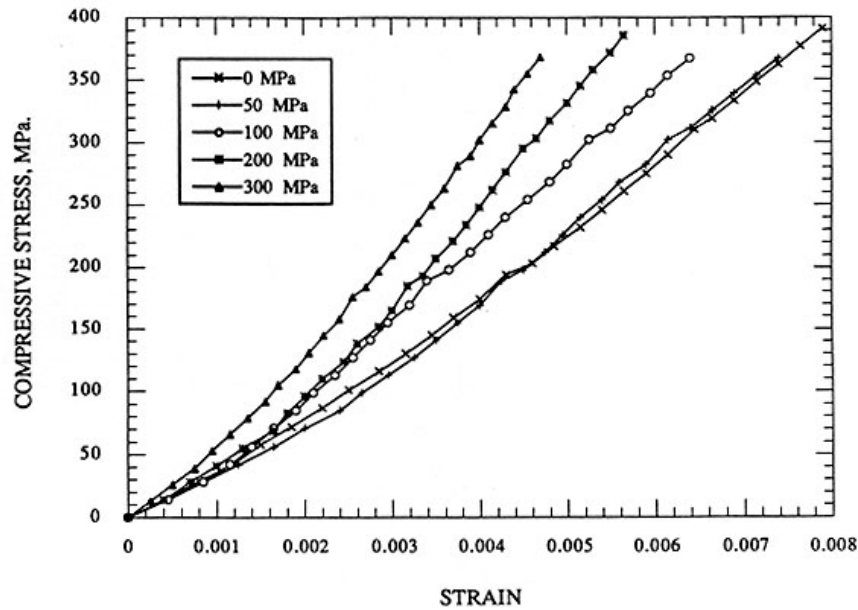


Figure 2.5-6. Stress-strain response of ceramic TBC held for one hour at a temperature of 800 °C at the indicated stress. Increasing modulus with stress level indicates that the material has crept under load [27].

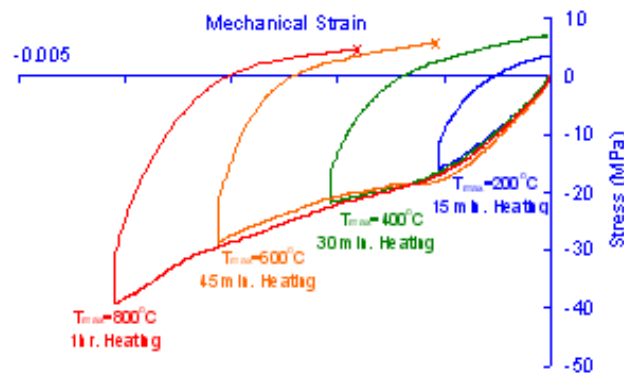


Figure 2.5-7. Thermal mechanical test of ceramic TBC showing that creep at high temperature and stress can result in a tensile stress on cooling. This is similar to the stress-strain history of a TBC on a metallic substrate during heating and cooling [28].

coating due to its higher thermal conductivity, which, in combination with higher strength and ductility, helps to increase their durability.

Property evaluation and modeling of the TBC structures to understand their mechanical behavior have been the focus of several studies [15,17,18,22,26,27,28,]. A significant result in this area has been the development of a tentative model based upon the physical structure of the coating by Redja [28]. The model accounts for the deformation or strain of the coating based on four characteristics of the coating; the basic elastic response of the material,  $\Delta\epsilon_{\text{ELASTIC}}$ , the influence of the open crack closure,  $\Delta\epsilon_{\text{OPEN}}$ , the sliding of microcracks in the structure,  $\Delta\epsilon_{\text{SLIDING}}$ , and tensile microcrack extension under load,  $\Delta\epsilon_{\text{CRACKING}}$ , Figure 2.5-8. The intrinsic modulus of the material will be lowered by the effect of the other three characteristics. The effect of open crack closure and sliding of microcracks is described in the model by the concept of crack volume,  $V_{\text{OPEN}}$  and  $V_{\text{SLIDING}}$ .  $V_{\text{OPEN}}$  is defined as the crack length per volume of coating that opens or closes under loading.  $V_{\text{SLIDING}}$  is defined as the crack length per volume of coating that under goes sliding at the interface of the crack under load. In addition to the volume of sliding cracks, the friction of the crack interface,  $f_{\text{SLIDING}}$ , and the orientation of the cracks relative to the applied load,  $\beta_{\text{MIN}}$  and  $\beta_{\text{MAX}}$ , must be taken into consideration. Tensile cracking is accounted for by the increase in extension due to the stress level that is above the tensile strength of the coating.

By appropriate selection of the model parameters, this model has been shown to predict the stress-strain response of the TBC ceramic quite well. Figure 2.5-9 shows the actual and predicted stress-strain curves for an 8% yttria-zirconia TBC. The model has been used to predict the coating response to thermal mechanical loading with some success and the model predicts the maximum compressive strain limit above which failure will occur. Comparison of the model to thermal fatigue specimen test results is shown in Figure 2.5-10.

The model parameters for crack volume that is active to the opening/closing and to sliding under load can be determined from simple mechanical test of the material. Redja et. al. [28] used tubular free standing specimens of the coating under tensile and compressive loading to determine the elastic and non-elastic response of the coating. A new method using instrumented indentation techniques can also be used to determine the coating response. The instrumented indentation technique is discussed in Section 4.6.

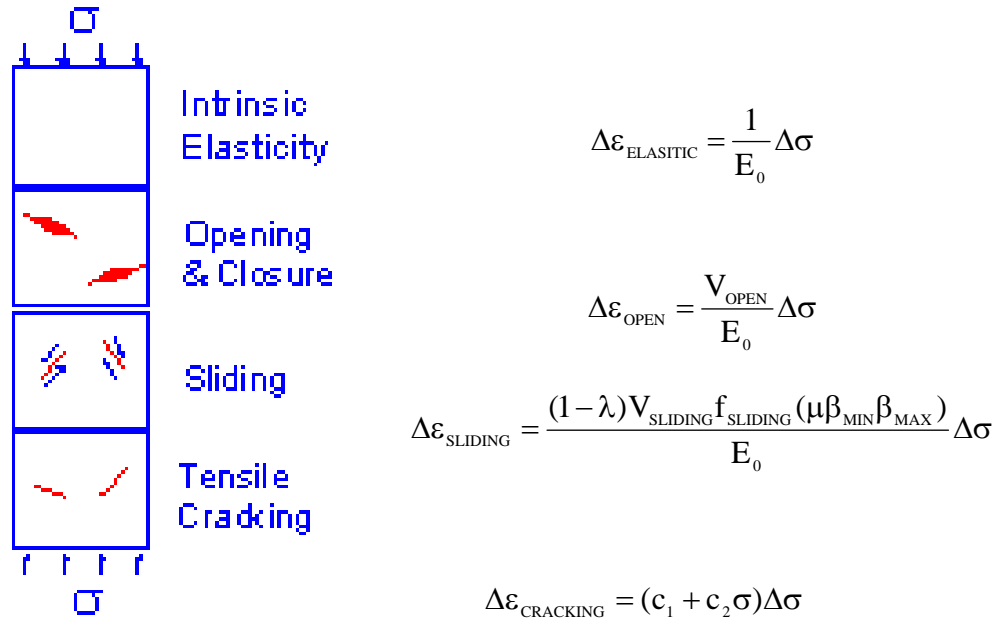


Figure 2.5-8. Proposed model by Redja, et al. [28], to explain the non-linear stress strain response of the TBC. Model prediction is compared to actual measurement in Figure 2.6-9.

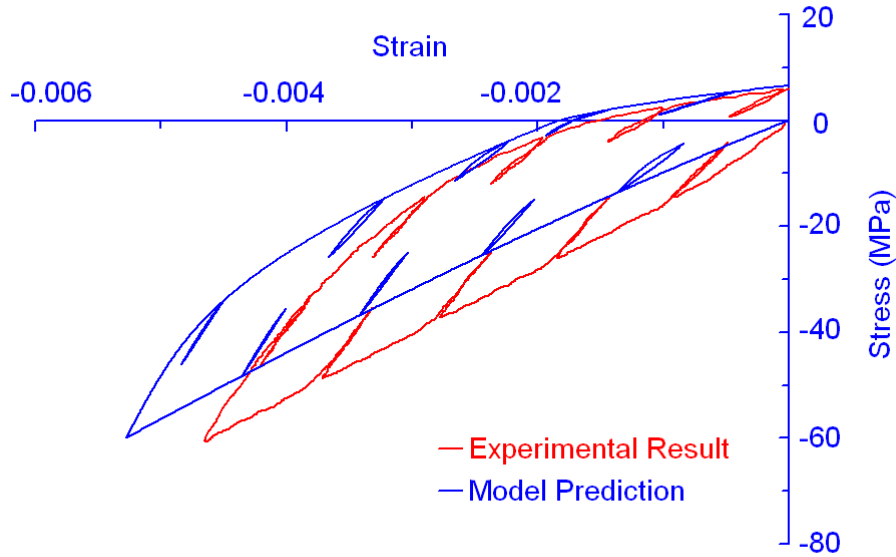
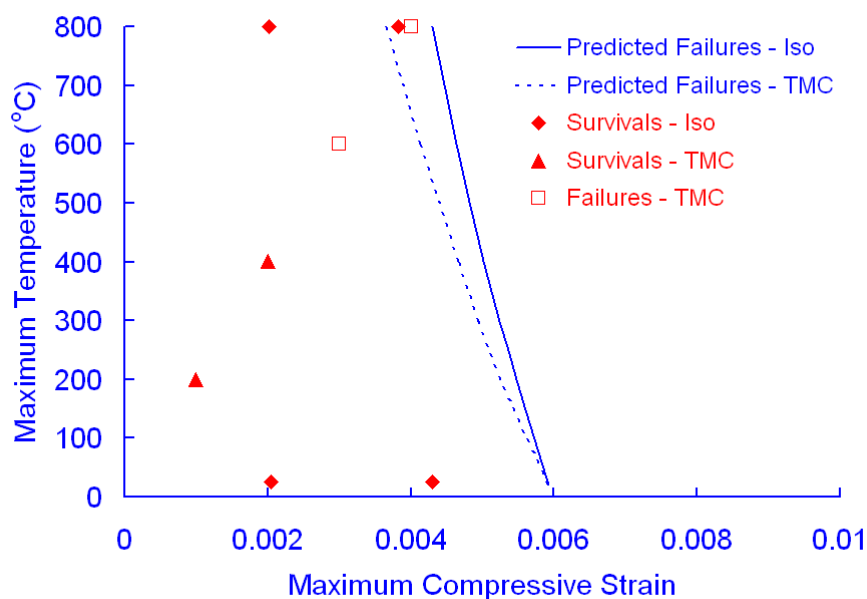


Figure 2.5-9. Model results compared to actual measured stress-strain of ceramic TBC [28].



*Figure 2.5-10. Thermal mechanical prediction compared to resulting failures indicating that the proposed model of Redja, et al., appears to be valid [28].*

## 2.6 Mechanical Properties of TBCs via Instrumented Micro-Indentation

Instrumented indentation techniques have been used to evaluate various coating as well as monolithic materials [60, 61]. The principle of the method is the precise measurement of the load and displacement of an indenter into the material from which the elastic modulus and hardness can be derived. By using low loads, on the order of 50 to 5000 mN, the properties of materials on the microstructural level can be assessed. Oliver and Parr [60] have developed a method for analyzing the load-unload curves for materials to account for the non-linearity of the unloading portion and demonstrated good correlation between the indentation method and standard tensile/compression testing of materials.

This is important in the area of thermal sprayed coatings, which have been shown to have non-linear load-deflection characteristics due to the inherent porosity and microcracking in the sprayed structure [62-65]. Alcalá et al. [62] demonstrated this for several metallic coatings sprayed via standard air plasma spray (APS) and vacuum plasma spray (VPS) techniques. The VPS-sprayed materials showed less porosity than APS coatings and had higher stiffness or modulus.

Penetration of the sharp indenter tips, such as a Vickers indenter, can induce elastic-plastic deformation and fracture at critical loads depending on the mechanical properties of the thermal spray coating. The indentation size for Vickers indenters is also on the order of the splat structure of the thermal sprayed coatings and therefore does not provide sufficient information in regard to the coating structure. The use of large spherical indenters has been proposed as a means to further evaluate the of coating structures [63].

Instrumented indentation techniques have been used in the past to evaluate thermal barrier coating systems and have been shown to provide insight into the mechanical behavior of the coatings. As the prior work does not provide a direct link to standard mechanical property testing of the coating materials, an assessment of the technique was made using a TBC material from prior Caterpillar testing in which modulus and strength data were available. The material was a plasma sprayed 8% yttria stabilized zirconia (YSZ) coating. Drs. Ed Redja and Darrel Socie of the University of Illinois have done extensive studies of the mechanical properties of this particular YSZ coating using samples sprayed at Caterpillar [21,23,28]. In particular, the elastic modulus of the coating under varies loads was determined by Dr. Redja, Figure 2.6-1. The modulus of the coating provides information on its structure and a model was proposed for the observed behavior by Dr. Redja (Figure 2.5-8).

As an assessment of the instrumented indentation method, the elastic modulus of samples of the same plasma sprayed YSZ coating, as provided to Redja and Socie, were measured using a spherical indenter (200 micron diameter) at Caterpillar. The moduli measured for the coating under the compressive loading by indentation compared very well with those measure by Redja and Socie using tube specimens loaded in compression, Figure 2.6-2.

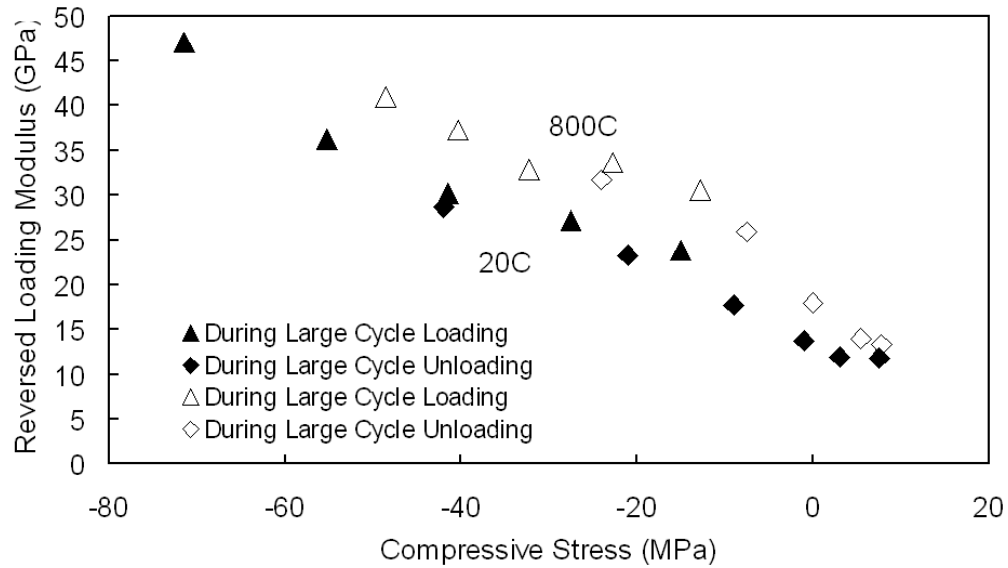


**Figure 2.6-1.** Modulus of elasticity for 8% YSZ coating (Lot 39073) as a function of applied load is shown as measure by Redja et al. using free standing tube specimens [28].

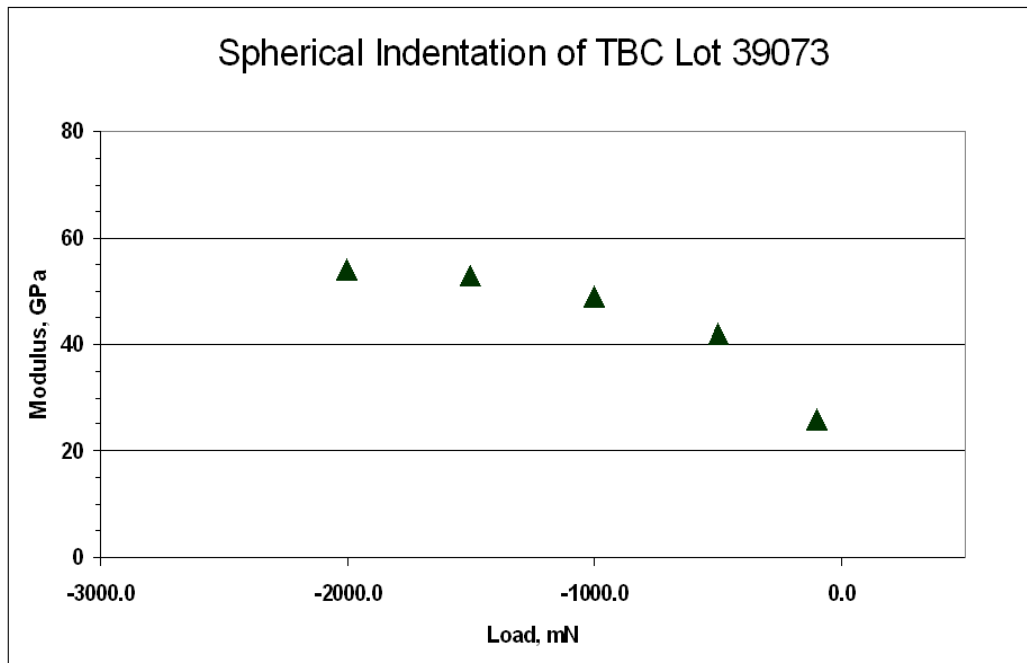


**Figure 2.6-2.** Modulus of the same 8% YSA coating as in Figure 4.7-1 as a function of applied load is shown but measured using instrumented indentation method with spherical indenter.

### **3.0 Quasicrystals and Approximants as Alternative Coatings in Diesel Engines**

Quasicrystalline materials may provide advantages over ceramic TBCs due to the formers unique properties. The reported low thermal conductivity of some quasicrystalline materials approach that of zirconia, while the thermal expansion of certain quasicrystalline materials is similar to that of steel, aluminum, and cast iron materials used in diesel engines. This may provide some advantage in reducing thermal stress caused by the mismatching of thermal expansion coefficients between the coating and the substrate, which is an important contribution to the total stress state in the current ceramic/metal systems. However, the higher ductility of the quasicrystal materials at high temperature may aggravate the creep of the coating caused by the compressive stress state induced by the thermal gradients found in TBC diesel engine applications.

#### **3.1 Quasicrystal and Approximant Properties**

The structures of quasicrystals (QCs) do not fit the classical definition of a crystal, in that the QCs have “forbidden” rotational symmetries of 5, 8, 10 and 12 fold symmetries [29]. QC materials have long-range translational order in regard to the atom locations within the crystal but do not have a periodic lattice cell that repeats. Instead, the “unit cell” dimension is essentially the QC structure. Thus, QC materials have aperiodic order, which result in their unique rotational symmetries. The aperiodic order results in the unique mechanical and physical properties of the QC materials, in particular their low thermal conductivity for a metallic material (see Table 3.1-1) [35].

In addition to true QC structures, numerous approximant structures, which exhibit atomic arrangements that are very similar to aperiodic QC structures, have been identified. The approximant structures are crystals in the traditional sense that they exhibit periodic translational order [30, 43]. Both the QC and approximant structures typically exist over relatively narrow compositional ranges, and many of these are metastable, which accounts for their late identification in the field of crystallography [31-33]. A large number of QC and approximants have been identified in two major alloy systems: Al-TM (transition metals) and Mg-Al-Zn. These alloy systems form both metastable and stable QC and approximant phases with two predominate structures, icosahedral and decagonal [34].

The thermal and electrical properties of QC materials differ the most from traditional metallic materials. The reasons for this difference are not well understood and are the area of

current research. QC alloys based on aluminum have thermal conductivities in the 1 to 6 W/m-K range, which is more typical of ceramics such as zirconia, but have thermal expansion properties similar to metals (14 to 19 mm/mm/C), Table 3.1-1 [4, 35]. These unique attributes of QC materials make them candidates for TBC applications. The  $\text{Al}_{71}\text{Co}_{13}\text{Fe}_8\text{Cr}_8$  composition studied by Archambault et al. [4] and Sanchez et al. [5], has a melting temperature near 1000 °C and low thermal conductivity. It was shown that this alloy is resistant to oxidation at temperatures up to 1000 °C [5]. Although not widely studied, several Al-based QC materials and approximants have been developed that exhibit good high temperature oxidation resistance. However, one unresolved limiting factor is diffusion of the aluminum in these alloys when in contact with iron and nickel containing alloys, which has been shown to change in the composition of the QC or approximant [5,47]. This can cause transformation to non-QC (i.e., crystalline) phases with potentially dramatic impact on their properties.

**Table 3.1-1. Thermal properties (room temperature) of quasicrystal (QC) alloys (Al-Cu-Fe icosahedral phase and the  $\text{Al}_5\text{Co}_2$  type of approximant of the decagonal Phase) and other materials [4, 35]**

	<b>Thermal Conductivity, W/m-K</b>	<b>Thermal Expansion, <math>10^{-6}/\text{K}</math></b>
<b>Cu</b>	<b>387</b>	<b>17</b>
<b>Al</b>	<b>202</b>	<b>24</b>
<b>Steel and cast iron</b>	<b>50-54</b>	<b>10-12</b>
<b>ZrO<sub>2</sub></b>	<b>1.8</b>	<b>7-9</b>
<b>QC (Al-Co-Fe)</b>	<b>4</b>	<b>14-19</b>
<b>QC (Al-Cu-Fe)</b>	<b>1.8</b>	<b>14-19</b>
<b>QC (<math>\text{Al}_{71}\text{Co}_{13}\text{Fe}_8\text{Cr}_8</math>)</b>	<b>2.1</b>	<b>13.7</b>

In addition to thermal conductivity, the mechanical properties of QC materials have unique characteristics. High hardness (500 to 1000 DPH) and low ductility are typical room-temperature characteristics of aluminum-based QCs. The high hardness of the QC material is attributed to the low dislocation mobility at lower temperatures [3]. Higher ductility is observed at elevated temperatures (about 70% of their absolute melting temperature) with an indication of a brittle-to-ductile transition temperature [36]. Figure 3.1-1 shows the effect of temperature on the yield stress of several QC alloys [36]. The ability for plastic deformation

at high temperature and relatively low melting temperatures allows processing of these materials by the HVOF thermal spray process.

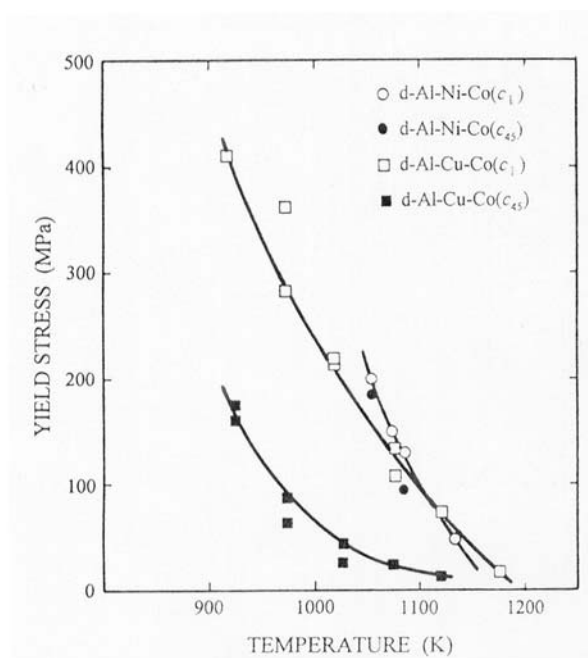


*Figure 3.1-1. Yield stress of QC materials decrease with temperature and approaches zero at 1000 °C [36]*

### 3.2 Quasicrystal and Approximant Coatings

One of the major advantages in the use of the quasicrystalline materials based on aluminum is the ability to apply the coating via HVOF (high velocity oxygen-fueled) processing, thereby creating a coating with relatively high strength, adherence, and density. Coating structures produced using HVOF processes can have nearly 99% densities compared to the 80-95% densities found in plasma sprayed zirconia TBCs. Coating adherences of 65 MPa or greater are common for HVOF coatings, while the adherence of plasma coatings are generally less than 50 MPa. The high density of the material could also eliminate the need for seal coatings, a major issue with durability related to the zirconia TBC systems.

The use of HVOF will also minimize compositional changes in the coating due to aluminum loss during spraying. Aluminum evaporates from the surface of the QC powder being plasma sprayed due to the low thermal conductivity of the QC material causing high surface temperatures [41]. The lower spraying temperature of the HVOF process should prevent this aluminum depletion.

Although the low melting point of the QC material provides an advantage in the choice of the coating-deposition process to be used, it also is a disadvantage in their use at high temperatures due to stability and strength considerations. Studies have shown that QC materials and coatings of the Al-Cu-Fe, Al-Cr-Fe, Al-Cu-Fe-Cr and Al-Co-Cr-Fe systems all show good oxidation resistance in the range of 750 to 1080°C due to the formation of dense aluminum oxide layers that inhibit any rapid oxidation of the material [44, 45, 46].

However, when applied as coatings, interdiffusion with the substrate/bond coating has been shown to occur [5, 47]. A major focus of Sanchez et al.'s [5] study was on the stability of the QC approximant and the development of bond coatings that act as diffusion "barriers" to prevent aluminum depletion of the QC coating. Results were reported for bond coatings consisting of Ni-5% Al mixed with yttria and the QC approximant mixed with yttria. The addition of the yttria was reported to slow the interdiffusion between the QC approximant and the substrate. No data were presented for bond coatings of more traditional MCrAlY composition. The use of high-aluminum containing MCrAlY type bond coatings may decrease the chemical driving force and hence the extent of aluminum diffusion.

A recent study by Huttunen-Saarivirta et al. [42] using HVOF to deposit the  $\text{Al}_{71}\text{Co}_{13}\text{Fe}_8\text{Cr}_8$  alloy has raised the issue as to the exact structure of the starting powder and resulting coating. The initial work by Archambault et al. [4] identified the  $\text{Al}_{71}\text{Co}_{13}\text{Fe}_8\text{Cr}_8$  composition to be an approximant of the decagonal phase that was close in similarity to the hexagonal  $\text{Al}_5\text{Co}_2$  crystal structure. The  $\text{Al}_5\text{Co}_2$  structure was identified for the starting materials used by Sánchez et al. [4] as well. In addition, Reyes-Gasga et al [66] showed that  $\text{Al}_{71}\text{Co}_{13}\text{Fe}_8\text{Cr}_8$  powders produced by Saint Gobain Company under the trade name of Christome BT1 contained compounds of  $\text{Al}_5\text{Co}_2$ ,  $\text{Al}_2\text{O}_3$ , and  $\text{Co}_2\text{O}_3$  and the alloys  $\text{Al}_{86}\text{Cr}_{14}$  and  $\text{Al}_{80}\text{Cr}_{20}$ , which have been reported to be quasicrystalline phases. However, Huttunen-Saarivirta et al. [42] showed that the starting powder of  $\text{Al}_{71}\text{Co}_{13}\text{Fe}_8\text{Cr}_8$  was comprised of the QC dodecagonal phase and a texture of this phase was present in the coatings produced. Detailed diffraction analysis and phase identification were not within the scope of this study, therefore, only a comparison of the X-ray diffraction patterns to that of Sánchez et al. [4] for the starting powders and coating was done.

Although the oxidation, hardness and wear characteristics of QC materials have been investigated, little information on the mechanical strength of these materials (particularly in coating form) is available. In this work the mechanical properties and thermal stability of thermal sprayed  $\text{Al}_{71}\text{Co}_{13}\text{Fe}_8\text{Cr}_8$  quasicrystalline approximant material will be assessed using instrumented indentation methods. The Saint Gobain Company markets this material under

the trade name of Christome BT1. Although the BT1 material is a quasicrystal approximant, it will hereafter be referred to simply as a quasicrystal.

### **3.3 Primary Issues That Need to be Addressed for Application of QC as TBC**

The primary issues to be addressed in the development of QC materials as thermal barrier coatings are related to high temperature phase stability and mechanical properties. Due to aluminum being the major alloying element in the oxidation-resistant QC alloys, their melting points are relatively low and close to the 900 °C to 1000 °C maximum component temperatures of insulated diesel engine components. At these temperatures the chemical mobility or diffusion kinetics for aluminum is high. The  $\text{Al}_{71}\text{Co}_{13}\text{Fe}_8\text{Cr}_8$  approximant to be investigated contains Co and Cr to raise its melting point and enhance its oxidation resistance. In cyclic oxidation testing, it demonstrated good stability and oxidation resistance to 1000 °C when tested as a free-standing material (not attached to a substrate) in prior studies [5]. When the alloy was applied as a coating to a nickel substrate, diffusion of aluminum into the substrate followed by formation of Ni-Al compounds resulted. The depletion of aluminum in the BT1 alloy will result in the loss of the insulating properties as the materials composition changes from that for the quasicrystal structure. To prevent the aluminum loss, the use of a diffusion “barrier” was proposed and several types were investigated [5]. By using a bond coat consisting of yttria combined with either a nickel aluminide or the BT1 QC resulted in slowing the growth of the interlayer compounds between the BT1 to the substrate. This suggests that the diffusion behavior of the chemical species in the QC will be dependent on the composition of the bond coat as well as the oxidation behavior of the bond coat.

In addition to oxidation and phase stability, the mechanical properties of the QC coatings will be of particular interest. It has been shown that the coating process has significant influence on the resulting coating strength and Young’s modulus [26]. Since QC materials have low yield stress at the temperatures of the diesel engine operation, Figure 3.1-1, the effect of the high component temperatures and high compressive stress states on the long-term durability of the approximant coatings will need to be investigated. In the present study, only the room-temperature properties of the QC coatings will be investigated using instrumented indentation techniques.

## 4.0 Experimental Procedures

### 4.1 Coating Materials

Three bond coat materials were used in this study and are listed in Table 4.1-1. The two nickel-based compositions were chosen to determine if the difference in aluminum content, and hence chemical activity, would have any effect on the resulting diffusion interaction between the BT1 QC and the bond coating. The iron-based bond coating was chosen to determine if there is a significant difference in diffusion behavior between the BT1 QC and iron compared to that of nickel. All three of the bond coating powders were made by gas atomization techniques with the powder sized to a  $-45+10$  micron distribution.

The quasicrystal powder ( $\text{Al}_{71}\text{Co}_{13}\text{Fe}_8\text{Cr}_8$ , designated as BT1 by the manufacturer) was purchase from Saint-Gobain with a nominal powder size of  $-53+20$  micron. The BT1 powder is a gas-atomized material with spherical particle morphology. The nominal weight percent composition of the BT1 powder is included in Table 4.1-1. The crystal structure of the BT1 powder was characterized by x-ray diffraction prior to spraying and was confirmed to be the same as the BT1 quasicrystalline approximant developed by Dubois et al. [4].

Plain carbon steel of type SAE 1040 was used for the coating substrates. The substrates were 19 mm long by 12.5 mm diameter rods. The ends of the rods were coated as shown in Figure 4.2-1. Four sets of nine specimens each were sprayed as outline in Table 4.1-2. One set consisted only of the QC material coated onto the substrate material. The other three sets consisted of one of the bond coating materials (Table 4.1-1) and the QC material sprayed in layers on the substrate as shown in Figure 4.1-1).

**Table 4.1-1. Nominal compositions of the bond coatings and quasicrystal material used in the study**

Bond Coat Designation	Nominal Composition, weight %					Manufacture
	Nickel	Chromium	Aluminum	Yttrium	Iron	
Ni-17Cr-6Al-0.5Y	76.5	17	6	0.5	-	Sulzer Metco
Ni-31Cr-11Al-0.6Y	57.4	31	11	0.6	-	Sulzer Metco
Fe-26Cr-8Al-0.4Y	65.5 (Fe)	26	8	0.4	-	Dynamet
BT1 QC	54.4 (Co)	11.4	55.4	-	12.8	St. Gobain

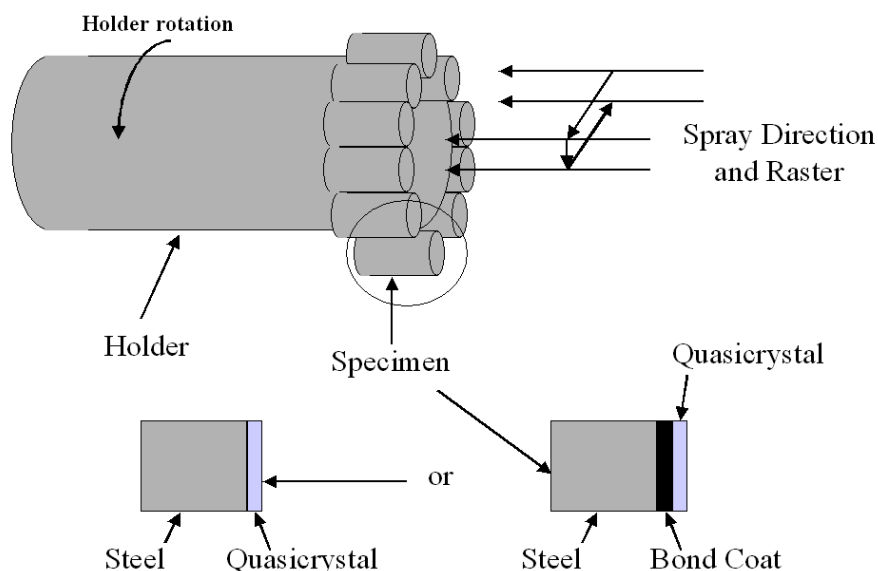


**Figure 4.1-1.** Schematic showing the setup for spraying of the diffusion couple samples using the Sulzer Metco DJ2700 spray torch and the two types of specimens sprayed, BT1 on one of the MCrAlY bond coats or BT1 on the SAE steel substrate.

**Table 4.1-2.** Samples sprayed for diffusion study

Coating Substrate	Bond Coating	Bond Coating Thickness, mm	BT1 Coating Thickness	Number of Specimens Sprayed
SAE 1040 steel	None	N/A	1.0	9
SAE 1040 steel	Ni-17Cr-6Al-0.5Y	1.0	1.0	9
SAE 1040 steel	Ni-31Cr-11Al-0.6Y	1.0	1.0	9
SAE 1040 steel	Fe-26Cr-8Al-0.4Y	0.5	0.5	9

## 4.2 Spray Process

The specimen holder was rotated at 300 RPM and the torch was traversed in a square raster pattern at 100 mm per second with a raster step of 5 mm. This is similar to the motion used to spray engine pistons. The SAE 1040 substrates were grit blasted to roughen the surface prior to spraying. Bond coatings and the BT1 QC were sprayed to thickness as shown in Table 4.1-2. As the bond coat materials were not grit blasted (only the SAE 1040) there was no of alumina grit embedded in these samples. Embedded grit was visible in the SAE 1040 samples at the interface between the BT1 and substrate.

The specimens extended by 5 to 10 mm in front of the specimen holder to prevent bridging of the coating between the specimens and the holder. The temperature of the specimens during spraying was kept to a maximum of 275°C by air-cooling.

The coating depositions were done at Caterpillar Inc.'s Technical Center in Peoria, IL, using a DJ2700 HVOF system manufactured by Sulzer Metco, Westbury, NY. The DJ2700 system uses oxygen, air and propylene in the combustion process. In thermal spraying, the critical processing parameters that control the resulting coating structure and properties for a given material are the particle temperature and speed on impact of the substrate surface. The particle temperature and speed were controlled in the process by the gas flows in the torch and the distance from the torch that the substrates were held. In order to aid in the selection of the spray parameters for the BT1 alloy, particle temperature and velocity were measured for various torch parameters using a DPV 2000 instrument marketed by TECNAR Ltd. of Montreal, Canada. The DPV instrument uses a sensor head with special optics and two slits in it to capture the radiant energy of individual particles. The optical sensor consists of special multi-element lens which is coupled to an optical fiber bundle. The optical sensor is sensitive to the particle radiation and has a two-slits photomask inserted between the lens and the central optical fiber. As a particle passes in front of the sensor it will generate a two signals, one from each mask slit. Precise timing of the signals and knowing the distance between the two slits allows for accurate calculation of the particle speed. The temperature measurement were based on two-wavelength pyrometry theory using the radiant energy of the particle viewed. The DPV instrument uses multiple particles to provide average particle velocity and temperature information.

Initial HVOF spraying of the BT1 material using selected standard parameters for metallic coatings recommended by Sulzer Metco was used to verify the design space to be used. Design of experiment techniques were used to investigate the spray parameters that impacted the coating deposition of the quasicrystal material. The major response variable used for the selection of the coating process variables was the deposition efficiency (DE). The DE is percentage of the powder fed through the spray torch that is deposited onto the substrate. For HVOF processing, DE in the range of 40 to 50% is typical for hard cermet type materials. Metallic materials can have a DE in the range of 60 to 80%.

HVOF spray parameters evaluated included total gas flow, fuel/oxygen ratio, airflow, and spray distance (standoff). The total gas flow and fuel/oxygen ratio influences the combustion temperature and gas velocity, and thus the particle temperature and speed. The air flow influences the particle speed while not affecting the temperature due to the high nitrogen content, which compensates for the oxygen addition by cooling the flame. The

spray distance, or standoff, results in changes in the particle speed and temperature as the particles accelerate after exiting the torch then start to decelerate as the gas velocities slow.

Two types of coating specimen geometries were produced. One with the BT1 QC coating on the SAE 1040 substrate with no bond coat layer and the other with the BT1 QC on one of the three bond coat materials (Figure 4.1-1).

### 4.3 Diffusion Experiments

The quasicrystal and bond coat/substrate compatibilities were assessed by isothermal exposure studies in vacuum, performed at the Ames Laboratory, Ames, IA. Each of the sprayed samples were sealed in quartz tubing under vacuum and held at temperature, after which they were directly quenched in water in order to preserve the structure formed at temperature. Samples of each substrate/bond coat/quasicrystal combination were held at 500°C, 700°C and 900°C for time intervals of 25, 100, and 500 hours as shown in Table 4.3-1. This resulted in a total of 36 different material couple, time and temperature combinations.

**Table 4.3-1. Exposure temperature and times for the BT1 diffusion couples**

Material Combinations	Temperature	Test Hours
SAE 1040/BT1, Ni-17Cr-6Al-0.5Y/BT1, Ni-31Cr-11Al-0.6Y/BT1, Fe-26Cr-8Al-0.4Y/BT1	500	25
SAE 1040/BT1, Ni-17Cr-6Al-0.5Y/BT1, Ni-31Cr-11Al-0.6Y/BT1, Fe-26Cr-8Al-0.4Y/BT1	500	100
SAE 1040/BT1, Ni-17Cr-6Al-0.5Y/BT1, Ni-31Cr-11Al-0.6Y/BT1, Fe-26Cr-8Al-0.4Y/BT1	500	500
SAE 1040/BT1, Ni-17Cr-6Al-0.5Y/BT1, Ni-31Cr-11Al-0.6Y/BT1, Fe-26Cr-8Al-0.4Y/BT1	700	25
SAE 1040/BT1, Ni-17Cr-6Al-0.5Y/BT1, Ni-31Cr-11Al-0.6Y/BT1, Fe-26Cr-8Al-0.4Y/BT1	700	100
SAE 1040/BT1, Ni-17Cr-6Al-0.5Y/BT1, Ni-31Cr-11Al-0.6Y/BT1, Fe-26Cr-8Al-0.4Y/BT1	700	500
SAE 1040/BT1, Ni-17Cr-6Al-0.5Y/BT1, Ni-31Cr-11Al-0.6Y/BT1, Fe-26Cr-8Al-0.4Y/BT1	900	25
SAE 1040/BT1, Ni-17Cr-6Al-0.5Y/BT1, Ni-31Cr-11Al-0.6Y/BT1, Fe-26Cr-8Al-0.4Y/BT1	900	100
SAE 1040/BT1, Ni-17Cr-6Al-0.5Y/BT1, Ni-31Cr-11Al-0.6Y/BT1, Fe-26Cr-8Al-0.4Y/BT1	900	500

#### 4.4 Characterization of Coatings and Powder via SEM, Microprobe and XRD

The exposed samples were evaluated using standard metallography, SEM, XRD and microprobe analysis. Sample preparation was performed at the Ames Laboratory's metallography facility. The quenched samples were sectioned lengthwise using a low-speed diamond saw. One half of each sectioned sample was mounted in a standard epoxy mounting material and polished for metallographic, microprobe and SEM examinations using the automated polishing procedure outlined in Table 4.4-1. The other half of the sample was used for X-ray diffraction analysis of the thermally exposed BT1 QC coatings. The initial crystalline structure of the powders was documented via x-ray diffraction. XRD patterns for both the powders and BT1 QC were generated using copper as the x-ray source ( $\lambda = K\alpha \text{ Cu} = 0.154178 \text{ nm}$ ). The initial powder XRD was conducted at Caterpillar's Technical Center and the coatings of BT1 were done at the Ames Laboratory.

*Table 4.4-1. Polishing procedure used for quasicrystal coatings*

Media	Head Pressure	Head Rotation	Rotation Speed	Polish Time
240-600 SiC	5 lbs.	contra	120rpm	50 sec
6um diamond on Texmet™*	7 lbs.	comp	120rpm	4 min
1um diamond on Mastertex™*	7 lbs.	comp	120rpm	4 min
Colloidal Silica on ChemometITM*	9 lbs	contra	120rpm	4 min
Colloidal Silica on ChemometITM*	5 lbs.	comp	120rpm	2 min

\*Buelher Ltd. polishing supplies

Scanning electron microscopy of the BT1 QC coatings was performed at Caterpillar's Technical Center using a JOEL (Japanese Electron Optics Laboratory) Field Emission SEM with 20 kV beam excitation. Energy dispersive x-ray analysis was used with the SEM to identify compositions of precipitates in the BT1 QC coating. Penetration depths and interlayer thickness were also determined via SEM micrographs at 300X magnification.

The microprobe analysis was performed using a JEOL model JXA-8200 equipped with 5 WDS spectrometers. A 20kV acceleration voltage and a 20nA beam current (measured on a Faraday cup before each analysis) were used for each analysis. Table 4.4-2 shows the x-ray lines, the WDS crystal used for each element and the standards used for calibration. Spacing of each analysis was 2 or 4 micron depending on the resolution required which was related to the thickness of the diffusion zones assessed. The polished specimens were carbon coated prior to analysis.

The accuracy of the microprobe analysis is greatly affected by the presences of microcracks and porosity in the samples. Detection limits on the order of 100 ppm are standard for this technique, but the volume of material excited by the electron beam is on the order of 1  $\mu\text{m}$  in depth and 1  $\mu\text{m}$  in diameter. Sample porosity this size range or larger can result in considerable scatter in the measurement. Spatial resolution limits the measurement increments to 2  $\mu\text{m}$  minimum with up to 4  $\mu\text{m}$  being used depending on the dimensions of the feature being analyzed.

**Table 4.4-2. Elements, x-ray lines, WDS crystals and standards used for microprobe analysis.**

Atomic no.	Element	Line	Crystal	Standard
13	Al	K $\alpha$	TAP	Metal
24	Cr	K $\alpha$	LIF	Metal
26	Fe	K $\alpha$	LIF	Metal
27	Co	K $\alpha$	LIF	Metal
28	Ni	K $\alpha$	LIF	Metal

#### 4.5 Diffusion Analysis Procedure

Estimated average interdiffusion coefficients were calculated from the microprobe concentration gradients based on the method outlined by Dayananda [49,50]. Using Dayananda's analysis method, it is possible to calculate average interdiffusion coefficients for individual species of multicomponent systems based on a single diffusion couple. Dayananda's approach is outlined in the following [49].

For a multicomponent diffusion profile as shown in Figure 4.5-1, the interdiffusion flux is expressed by

$$\tilde{J}_i = -\sum_{j=1}^{n-1} D_{ij}^n \frac{\partial C_j}{\partial x} \quad (i=1,2,\dots,n-1) \quad (1)$$

This can be written as

$$\tilde{J}_i = \tilde{D}_i^{\text{eff}} \frac{\partial C_i}{\partial x} \quad (i=1,2,\dots,n) \quad (2)$$

where

$$\tilde{D}_i^{\text{eff}} = \tilde{D}_{ii}^n + \sum_j \frac{\tilde{D}_{ij}^n}{\partial C_i / \partial x} \frac{\partial C_j}{\partial x} \quad (j \neq i) \quad (3)$$

Dayananda recognized that  $\tilde{D}_i^{\text{eff}}$  is a function of the composition of the diffusion path for a given couple. This then allowed for defining of the diffusion flux as

$$J_i = \frac{1}{2t} \int_{C_i^+ \text{ or } C_i^-}^{C_i(x)} (x - x_0) dC_i \quad (i=1,2,\dots,n) \quad (4)$$

where  $x_0$  is the Matano plane and assumes that  $C_i$  is a function of the Boltzmann parameter  $\lambda$  given by  $x/\sqrt{t}$ . This integral can be evaluated from the appropriate area under the composition/distance profiles for the various diffusion couples. On integrating, one gets

$$\int_{x_1}^{x_2} \tilde{J}_i dx = \int_{(x_1-x_2)}^{(x_2-x_1)} \tilde{J}_i d(x - x_0) \quad (5)$$

$$= \tilde{J}_i (x - x_0) \Big|_{x_1}^{x_2} - \int_{\tilde{J}_i(x_1)}^{\tilde{J}_i(x_2)} (x - x_0) d\tilde{J}_i \quad (6)$$

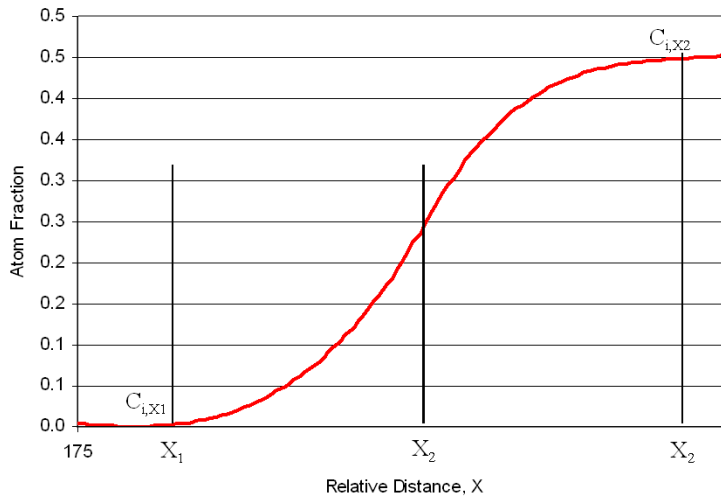


**Figure 4.5-1. Schematic of concentration profile for component  $i$  of a multicomponent diffusion couple.**

Since, according to Dayananda,  $d\tilde{J}_i = \frac{1}{2t}(x - x_0)dC_i$  from Eq. (4), Eq. (5) becomes

$$\int_1^{x_2} \tilde{J}_i dx = \tilde{J}_i(x_2)(x_2 - x_0) - \tilde{J}_i(x_1)(x_1 - x_0) - \frac{1}{2t} \int_{C_i(x_1)}^{C_i(x_2)} (x - x_0)^2 dC_i \quad (7)$$

and since  $\tilde{J}_i = \tilde{D}_i^{\text{eff}} \frac{\partial C_i}{\partial x}$ ,  $\tilde{D}_i^{\text{eff}} = \frac{\tilde{J}_i \partial x}{\partial C_i}$  (8)

therefore

$$\tilde{D}_{i,AC}^{\text{eff}} = \frac{[\tilde{J}_i(x_1)(x_1 - x_0) - \tilde{J}_i(x_2)(x_2 - x_0)]}{C_i(x_2) - C_i(x_1)} + \frac{\int_{C_i(x_1)}^{C_i(x_2)} (x - x_0)^2 dC_i}{2t[C_i(x_2) - C_i(x_1)]} \quad (9)$$

where  $x_0$  is defined as the Matano plane.

The average effective diffusion coefficient (Eq. (9)) can thus be evaluated using the microprobe composition-distance plots. By recognizing that the the flux,  $\tilde{J}_i$ , for a component will approach zero in either alloy of the couple (Figure 4.5-1), Eq. (9) reduces to

$$\tilde{D}_{i,R} = \frac{\int_{C_i^+}^{C_i^0} (x - x_0)^2 dC_i}{2t[C_i^0 - C_i^+]} \quad (10)$$

on the right side of the Matano plane and to

$$\tilde{D}_{i,L} = \frac{\int_{C_i^0}^{C_i^-} (x - x_0)^2 dC_i}{2t[C_i^- - C_i^0]} \quad (11)$$

on the left side of the Matano plane. Over the entire concentration range of the diffusion profile, Eq. (9) reduces to

$$\tilde{D}_{i,C} = \frac{\int_{C_i^+}^{C_i^-} (x - x_0)^2 dC_i}{2t[C_i^- - C_i^+]} \quad (12)$$

These three equations allow for a comparison of the mobility of each species on either side of the Matano plane which gives some insight as to the controlling specie for the interlayer growth as well as the total interlayer thickness with time.

The interlayer thickness can be estimated from the average interdiffusion coefficients based on a root mean square penetration depth analysis. By expressing the integrals in Eq. (10) and (11) by:

$$\int_{C_i^+}^{C_i^0} (x - x_0)^2 dC_i = \overline{(x - x_0)_{i,R}^2} (C_i^0 - C_i^+) \quad (13)$$

and

$$\int_{C_i^0}^{C_i^-} (x - x_0)^2 dC_i = \overline{(x - x_0)_{i,L}^2} (C_i^- - C_i^0) \quad (14)$$

one obtains:

$$\overline{(x - x_0)_{i,R}^2} = 2\tilde{D}_{i,R} t \quad (15)$$

$$\overline{(x - x_0)_{i,L}^2} = 2\tilde{D}_{i,L} t \quad (16)$$

where  $\overline{(x - x_0)_{i,L}^2}$  and  $\overline{(x - x_0)_{i,R}^2}$  represent the root mean square distances (r.m.s.) from the Matano plane over the concentration ranges given. The effective penetration of the specie,  $x_{i,R}$  and  $x_{i,L}$  for the component on the right and left of the Matano plane,  $x_0$ , are represented by the root of these distances as:

$$x_{i,R} = \sqrt{2\tilde{D}_{i,R} t} \quad (17)$$

$$x_{i,L} = \sqrt{2\tilde{D}_{i,L} t} \quad (18)$$

Similarly from equation Eq. (12) one gets:

$$x_{i,C} = \sqrt{2\tilde{D}_{i,C} t} \quad (19)$$

The ability to determine the r.m.s depth of penetration from  $\tilde{D}_i^{\text{eff}}$  allows the interlayer growth to be evaluated for each temperature of interest.

As can be seen from the analysis above, the method for determining  $\tilde{D}_i^{\text{eff}}$  relies upon a graphical solution from the concentration profiles. Dayananda has developed a software package, MultiDiFlux©, to aid in the evaluation composition-distance plots of this type using these equations [51]. The Dayananda software has not yet been updated to handle multiphase couples as are present in the microstructures of the BT1 coated specimens in this study. Notwithstanding, the software could be used to calculate the species flux, Matano plane, and provide a smoothed curve of the composition-distance data that was then used to calculate the integral in Eq. (9) using the trapezoidal rule for approximating integrals [52]. The calculation of the diffusion coefficient for each species was modified from that described to account for the multiphase nature of the diffusion couples that developed at the higher temperatures and exposure times. Profiles as shown in the schematic in Figure 4.5-1 were typical for the current coated systems. The diffusion coefficients  $\tilde{D}_{i,L}$  and  $\tilde{D}_{i,R}$  for each species were calculated based the  $x_1$  and  $x_2$  on either side of the Matano plane as defined in Figure 4.5-1 using equation (9).

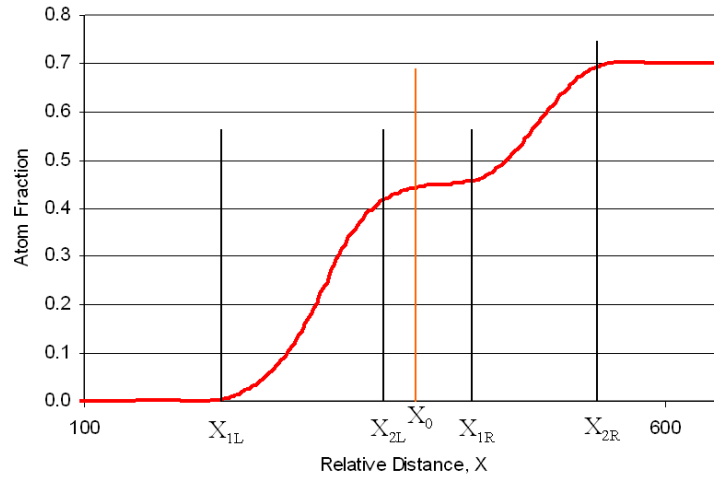


**Figure 4.5-1.** Diffusion profile for component  $i$  of a multicomponent diffusion couple with a multiple phases in the couple. The diffusion coefficient is evaluated on either side of the middle phase.

#### 4.6 Mechanical Properties of Quasicrystal Coating via Instrumented Micro-Indentation

The diffusion annealed BT1 QC coatings were also analyzed via instrumented indentation to determine the effect of time at temperature on mechanical behavior. Both a Vickers indenter and a 0.4 mm diameter spherical indenter were used with Caterpillar's CSM Micro-Combi Testers (load range: 0.1 – 30 N) to assess the QC coating in this study. The indentations with the Vickers indenter provided insight into the hardness and modulus of the

QC approximant material; while, the spherical indentation provided insight on the affect of the coating sprayed structure (porosity and microcracking) on the coating modulus [63].

The hardness and modulus of the BT1 coatings were measured at 1 N and 5 N loads for various diffusion couples. The measurements were taken at a midpoint between the top surface of the BT1 layer and the interface between the substrate so that no diffusion affects on the BT1 would be present. Not all couple specimens were evaluated, but a sufficient number was done to provide reasonable assessment of the variation found between samples. Each test consisted of loading to 1 N at 2 N per minute, a 1 second dwell at load, unloading to 0.02 N, a 1 second dwell and then reloading to the 5 N level at 10 N per minute with a 1 second dwell followed by unloading.

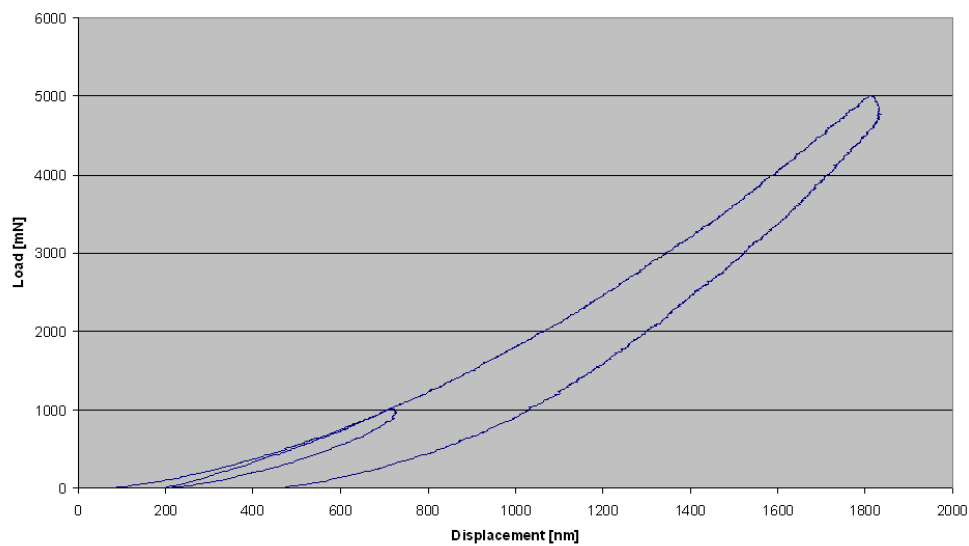
For the Vickers indenter, both the hardness and modulus of the BT1 QC were evaluated. The modulus may be determined from the load-displacement curve at the onset of unloading,  $S$ , using the equations below where  $P$  is the load,  $h$  the indentation depth,  $A$  is the area of contact  $\nu$  is Poisson ratio and the subscripts  $r$ ,  $s$ , and  $i$  correspond to the reduced modulus of the system, the sample, and the indenter material (diamond for the Vickers indenter and steel for the spherical indenter).

$$S = \frac{dP}{dh} = \sqrt{\frac{4A}{\pi}} E_r \quad (22)$$

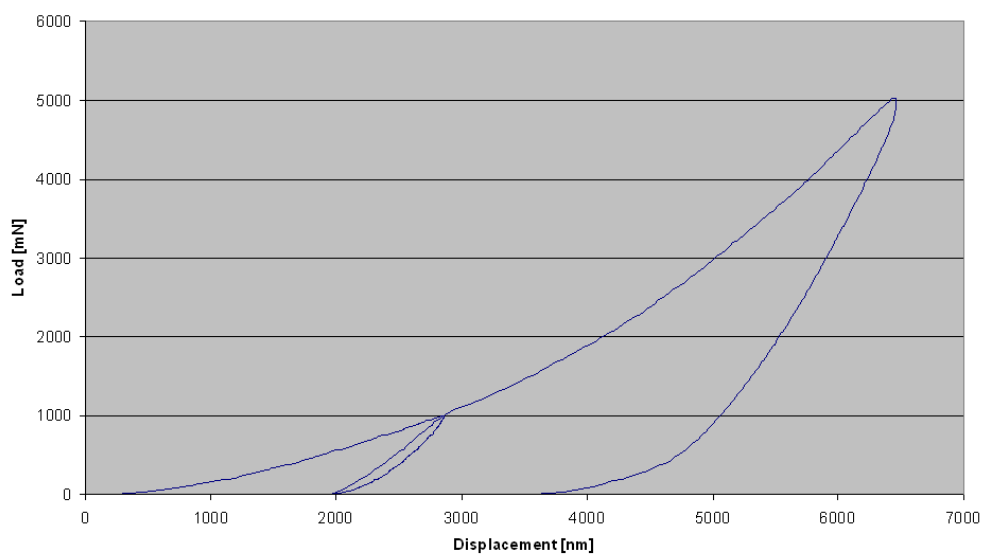
$$\frac{1}{E_r} = \frac{(1-\nu_s^2)}{E_s} + \frac{(1-\nu_i^2)}{E_i} \quad (23)$$

Ten indents were made on each coating sample with each indenter type. The average of the ten indents was used for comparison of the hardness and modulus at each load. Hardness was calculated for the Vickers indenter only while the modulus was determined for both the Vickers and spherical indenter shapes. Here in the moduli determined with the Vickers and spherical indenters will be referred to as the “Vickers modulus” or “spherical modulus” respectively.

Typical load displacement curves are shown in Figure 4.6-1 using the spherical and Vickers indenters. The volume of the coating that is sampled using the Vickers indenter is



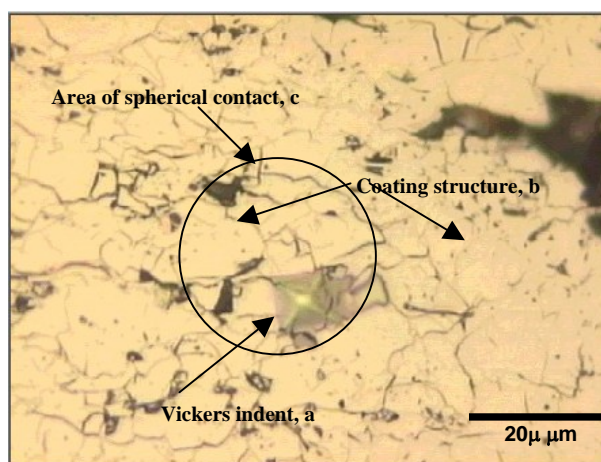
*spherical indenter load displacement curve*



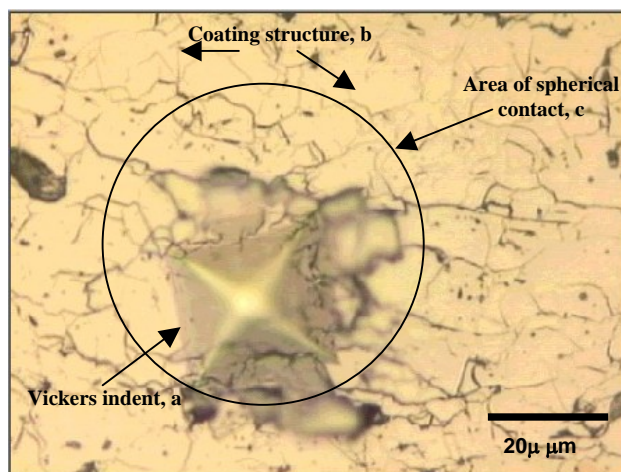
*Vickers indenter load displacement curve*

**Figure 4.6-1.** Typical load displacement curves for BT1 coating indentation using the Vickers and spherical indenters are shown. The measurements shown were on the BT1 QC coating held at 700 °C for 500 hours.

on the order of the lamellar structure or “splat” of the coating produced by the impact of each powder particle as shown in Figure 4.6-2. This results in the Vickers indenter measurement assessing the properties of the individual splats of the as-sprayed coating that should be similar to the starting powder properties. Indentation into the porosity of the coating as well as cracking at the edges of the Vickers indentations was common for many of the measurements. This resulted in a high scatter in the data as well as many of the measurements being determined to be invalid by the instrument software.



*Vickers indenter impression on the polished coating cross section. The circle represents the area of contact of the spherical indenter at 1 N*



*Vickers indenter impression on the polished cross section of the coating. The circle represents the area of contact of spherical indenter at 5 N*

**Figure 4.6-2.** Vickers indenter impressions at 1N and 5N loads in cross sections of the BT1 QC coating showing the relative size of the Vickers impression (a) to that of the coating “splat” structure (b) created by the impact of individual powder particles. The circle (c) represents the area of contact of the 0.4 mm diameter spherical indenter showing the large area and volume of the coating that is being sampled.

The indentation marks created by the 0.4 mm spherical indenter were not easily seen on the cross section of the coating after the measurement. The larger area of contact by this indenter results in the load being distributed across the coating features (multiple “splats”, cracks and porosity) such that the coating structure was assessed in addition to the bulk BT1 QC properties. This provided for an estimate of the composite properties of the coating which is the result of the influence of the movement under load of the coating cracks and pore deflection as well as the bulk properties of the BT1 QC material [63]. Circles representing the contact area of the spherical indenter are shown with the actual impression from a Vickers indentation at 1N and 5N loads in Figure 4.6-2. The relative amount of the coating structure that is being sampled by each indenter is schematically shown in Figure 4.6-3.

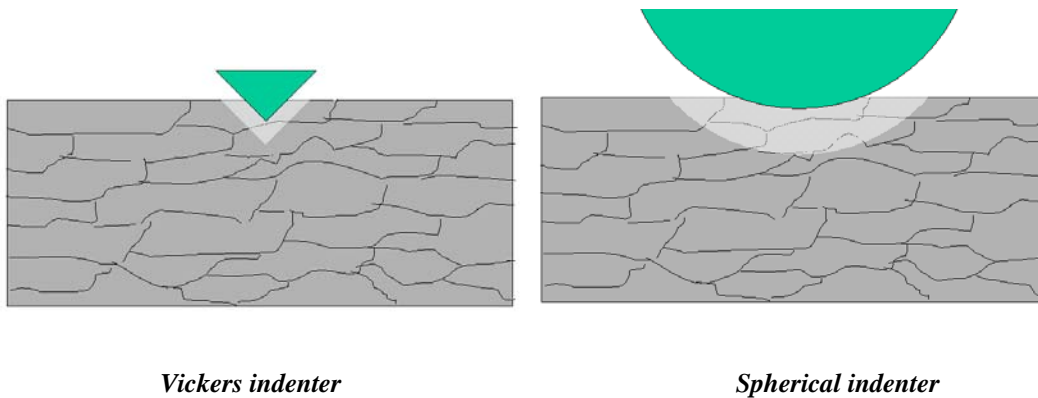


**Figure 4.6-3. Schematic representation of the coating depth and volume sampled by the Vickers and spherical indenters (not to scale).**

## 5.0 Results

### 5.1 Analysis of Starting BT1 QC Powder

The quasicrystal powder (designated as BT1 by the manufacturer) was purchased from Saint-Gobain with a nominal powder size of  $-53+20$  micron. The BT1 powder was a gas-atomized material with spherical particle morphology. The composition of the material was verified by ICP/AES chemical analysis and the results are summarized in Table 5.1-1.

The initial crystalline structure of the powders was characterized via x-ray diffraction (XRD) with  $\lambda = K\alpha$ ,  $\text{Cu} = 0.154178$  nm. The diffraction patterns for the as-received powder showed fewer and less defined peaks than what was reported previously by Sanchez et al. [5] and looked to be similar to those report by Huttunen-Saarivirta et al. [42], Figure 5.1-1. It is thought that this is due to the fine structure resulting from the high cooling rates used in the powder atomization process. The powders were therefore vacuum annealed at  $900^{\circ}\text{C}$  for one hour prior to being sprayed into coatings. This anneal allowed for the material to recrystallize or at least to develop a structure that the resulted in an XRD diffraction patterns close to that obtained by Sánchez et al. [5] for the bulk BT1 material. All the peaks corresponded to those identified by Sánchez et al. as identifying the QC structure. No additional XRD studies of this QC material were found in the literature so no detailed phase identification could be done. It is not known if the starting powders used by Sánchez et. al. had a similar crystal structure to the as-received powder used in this study, as no analysis was provided in that work. The coatings produced by Sánchez et al. were vacuum plasma sprayed and would have had much higher application temperature than the HVOF coatings in this study which probably accounts for difference in the XRD patterns they obtained for the as-sprayed coatings. The XRD diffraction pattern for the as-sprayed HVOF coating in this study reverts back to a pattern similar to that of the as-received powder. The quench rate of the sprayed particles in the HVOF process is on the order of or higher than that in the gas atomization process.

*Table 5.1-1. Quasicrystal powder, BT1, composition via ICP/AES analysis*

Primary Constituents	Wt%	At%	Residuals, ppm			
Al	54.2	71.5%	C	1400	Zn	12
Co	21.3	12.9%	O	460	S	13
Fe	12.3	7.8%	Ni	5100	Pb	4.5
Cr	11.4	7.8%	Si	1400	Ca	5.3
			Mn	230	Cd	0.01

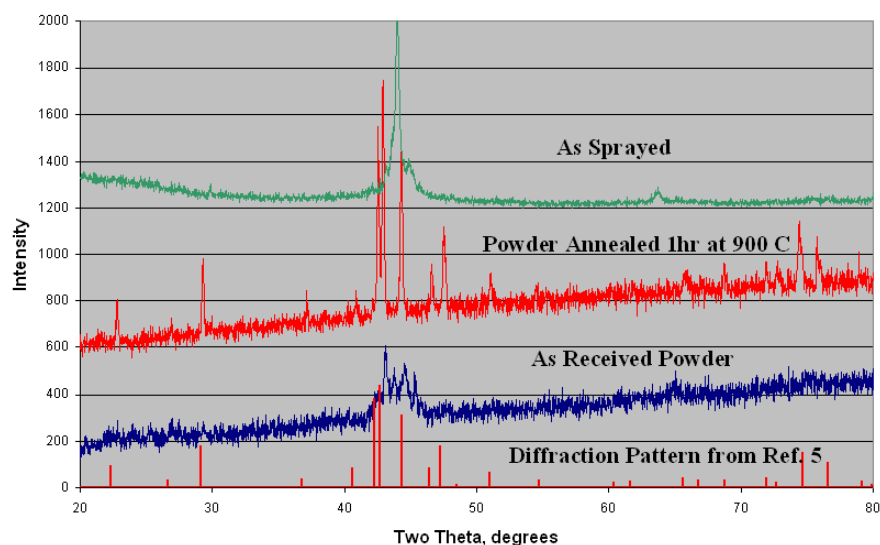


*Figure 5.1-1. XRD pattern for the as received powder and annealed powders showing the fewer and less defined peaks found in the as received powders.*

The hardness and elastic modulus of the annealed BT1 QC powder was evaluated by instrumented indentation using the Vickers indenter. Due to the small particle size, indenting loads were held to 0.1 N. Even at this low loading some cracking was seen around the indentation, as shown in Figure 5.1-2. Hardness and modulus of the powder was 1063.4 +/- 128.5 HVN and 159.5 +/- 8.7 GPa, respectively. No studies on the mechanical properties of the BT1 material were identified, so the powder properties were used as an estimate of bulk material properties.

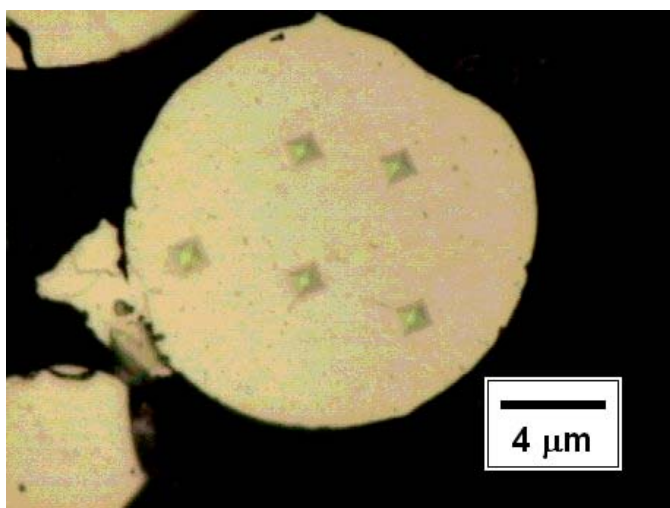


*Figure 5.1-2. BT1 QC powder particle showing the instrumented indents with minor cracking around some of the indents.*

## 5.2 Coating Deposition

Initial HVOF spraying of the BT1 material using selected standard parameters for metallic coatings was done to verify the design space to be used. Acceptable deposition efficiencies were demonstrated (30% to 40%) but coating microstructures had higher than desired porosity at all deposition parameters, Figure 5.2-2.

From the initial spraying, experimental runs were selected for spraying as shown in Table 5.2-1. In addition to the deposition efficiency, the particle temperature and velocities were measured using the DPV 2000 instrument (see section 4.2). The particle temperature and speed for the parameters used showed some correlation with the deposition efficiency, Figure 5.2-2, with higher particle temperature resulting in higher deposition efficiency.

The parameters from run 13 in Table 5.2-2 produced the best deposition efficiency (44.1%) with a dense microstructure and were used to spray the specimens for further evaluation of the QC coating properties.

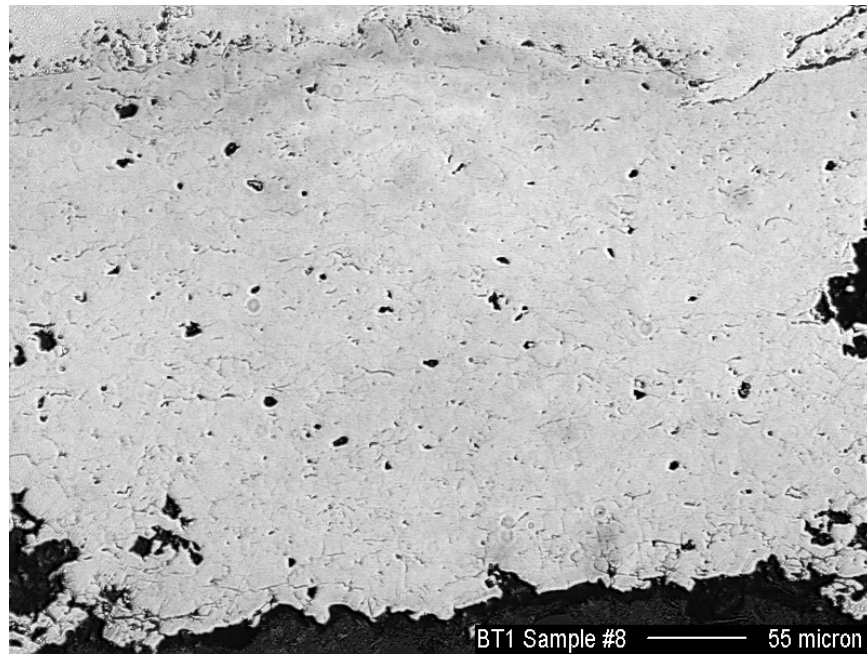


*Figure 5.2-1. Typical microstructure of BT1 QC sprayed with initial parameters in Figure 5.2-1 which exhibit lack of fusion between particles and high crack density.*

**Table 5.2-1. Experimental runs used to determine the parameter set to spray the BT1 quasicrystal alloy with high deposition efficiency.**

Run	TOTAL						Robot	Powder		
Number	O2/FUEL	FLOW	STAND	Air	Oxygen	Fuel	Speed,	No.	Feedrate,	
	(Ratio)	(SCFH)	OFF (mm)	(FMR)*	(FMR)*	(FMR)*	mm/sec	Pass	gm/min	%DE
1	2.3	1303	220	48	18	42	100	3	40	11.3
2	2.3	1303	300	48	18	42	100	2	43.5	19.0
3	2.3	1462	300	53	21	48	100	3	46.9	13.1
4	3.2	1310	300	49	20	33	100	3	44.7	22.4
5	4.2	1319	220	39	33	33	100	3	45.5	31.5
6	4.2	1319	300	39	33	33	100	3	45.7	36.5
7	4.2	1430	220	42	36	36	100	3	45	30.7
8	4.2	1430	220	42	36	36	100	3	45	28.1
9	4.2	1430	300	42	36	36	100	3	45	33.0
10	4.3	1428	230	44	34	34	100	3	46.2	28.9
11	3.1	1298	230	38	30	42	100	3	44.5	32.2
12	3.7	1414	230	42	34	39	100	3	43	31.4
<b>13</b>	<b>4.2</b>	<b>1188</b>	<b>300</b>	<b>29</b>	<b>36</b>	<b>34</b>	<b>100</b>	<b>3</b>	<b>43.5</b>	<b>44.1</b>
14	3.7	1414	300	42	34	39	100	3	45	34.1
15	3.7	1414	230	42	34	39	100	3	46.1	27.8
16	3.7	1044	260	30	26	30	100	3	41.6	38.9
17	4.1	918	260	25	25	25	100	3	41.5	34.1

\*FMR – flow meter reading from Sulzer Metco DJC console

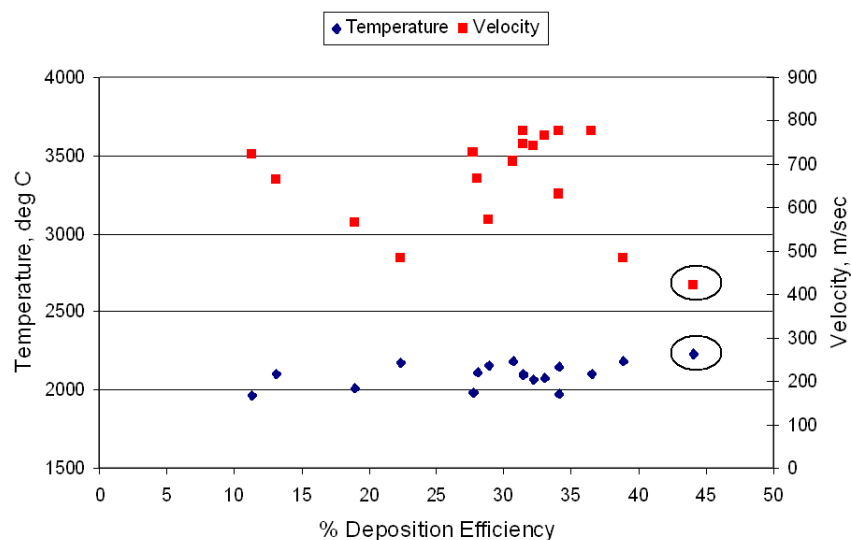


*Figure 5.2-2. Particle speed and temperature for the experimental runs from Table 4.2-1 are shown. Run 13 in Table 4.2-1 (circled points above) has the highest temperature and speed of the parameters tested which resulted in the highest deposition efficiency.*

Two types of coating geometries were produced for testing (see Figure 4.2-1). One specimen type was with the BT1 QC coating sprayed directly onto the SAE 1040 steel to 1 mm thickness. For the other type, one of the three bond coat materials was first sprayed onto the SAE 1040 steel to 1 mm thickness followed by the BT1 QC sprayed to 1 mm thickness. Thus there were four different specimen types of BT1 QC couples used in this study, one with each type of bond coat and one without.

### 5.3 Microstructure, XRD and Instrumented Indentation of BT1 QC Coating

The BT1 QC coating was characterized first without consideration of any interaction between the QC and bond coats or substrate. The BT1 QC will be required to withstand long exposures at diesel engine operating temperatures (500°C to 800°C) without degradation of its mechanical or thermal properties. Changes in the coating microstructure, crystal structure and mechanical properties were used to assess the stability of the BT1 QC coatings.

The sprayed samples exposed at temperature were examined by the methods described in Sections 4.3 to 4.6. The area of the BT1 QC coating analyzed was approximately half the distance from the coating surface to the interface between the BT1 QC and the bond coat or substrate. The initial BT1 QC coating microstructure as shown in Figure 5.3-1 exhibited low porosity, a uniform crack density and lamellar coating structure

that is on the scale of the original powder size (20 to 53 micron). The microstructure, hardness, modulus, and XRD pattern of the BT1 QC coatings exhibited different responses depending on the temperature and time of exposure. The longer times and higher temperatures resulted in microcrack and pore consolidation in the coating microstructure as well as changes in the hardness and modulus of the BT1 QC coating.

500°C Samples – Little change was seen in the coating structure at 500°C with up to 500 hours of exposure. The porosity and crack density appeared to be the same for both the 25 hour and 500 hour samples, as shown in Figure 5.3-2. From high magnification imaging, there did appear to be a small precipitate phase within the grains of the BT1 QC after 500 hours. Figure 5.3-2d attempts to indicate these precipitates, although, they are not easily seen. The size of this phase prevented accurate analysis using SEM EDS, but it was higher in Cr and Co compared to the bulk QC composition. The XRD analysis shown in Figure 5.3-3 indicates only a partial structural change toward the annealed powder state for the BT1 QC even after 500 hours at 500°C. No XRD peaks were seen that are different from those reported by Sánchez et al. [5], therefore that these precipitates may have been present in the materials used in that study.

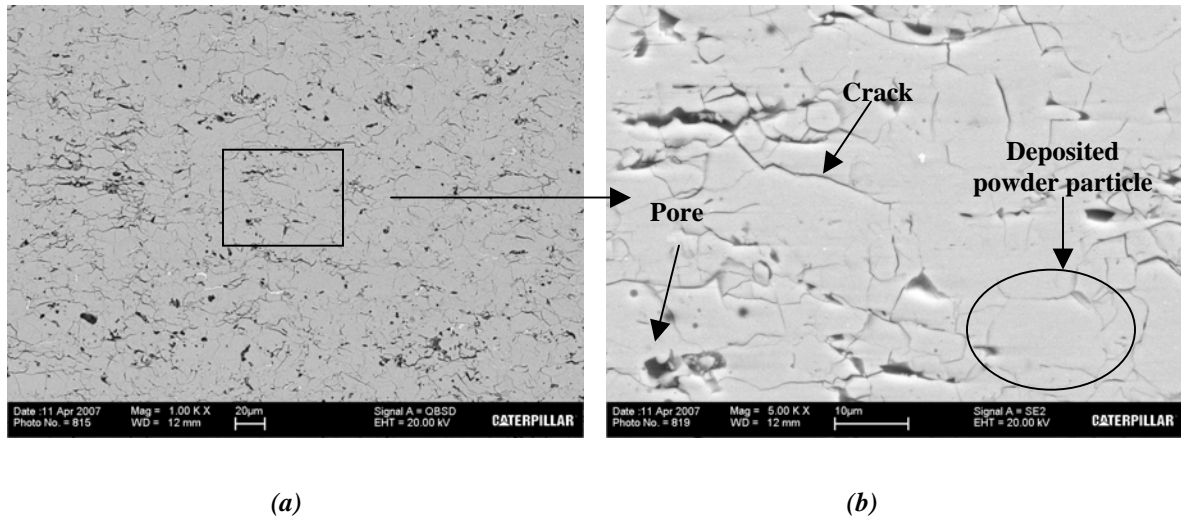
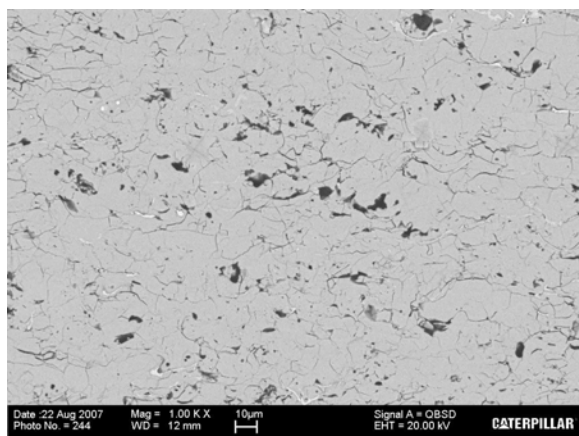
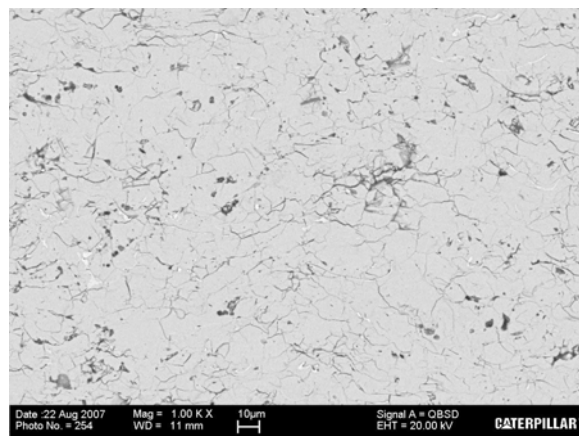


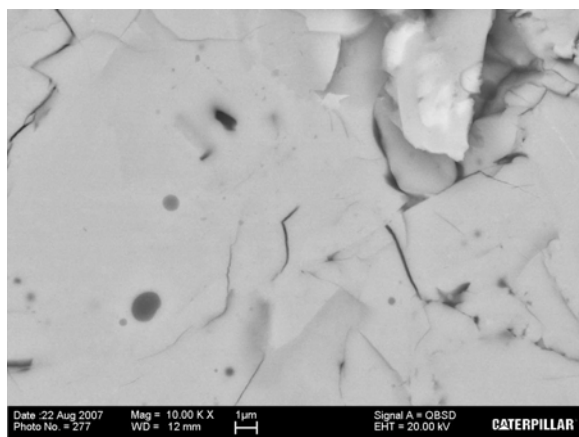
**Figure 5.3-1. BT1 QC coating microstructure sprayed with the selected HVOF parameters showing high density with microcracks typical of hard coating sprayed by HVOF. The coating features such as pores, microcracks and the deposited powder particles that comprise the lamellar coating structure are identified in (b).**



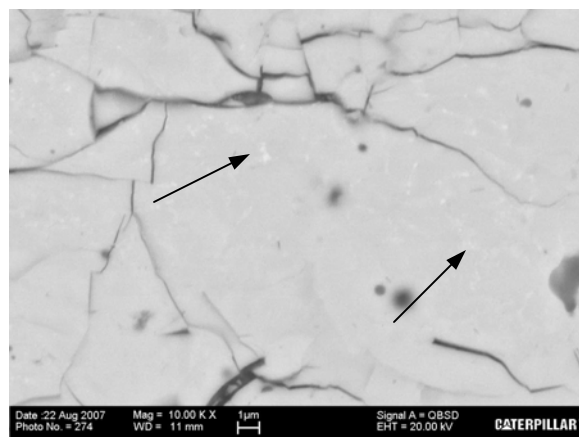
(a)



(b)



(c)



(d)

**Figure 5.3-2. Microstructure of BT1 QC coating exposed at 500 °C for 25 hours (a,c) and 500 hours (b,d) showing similar coating porosity and microcracking density to that of the as-sprayed coating. The 500 hour microstructure has precipitates which are attempted to be indicated by the arrows in (d). EDS analysis showed the precipitates to be higher in chrome and cobalt then the matrix of BT1 coating.**

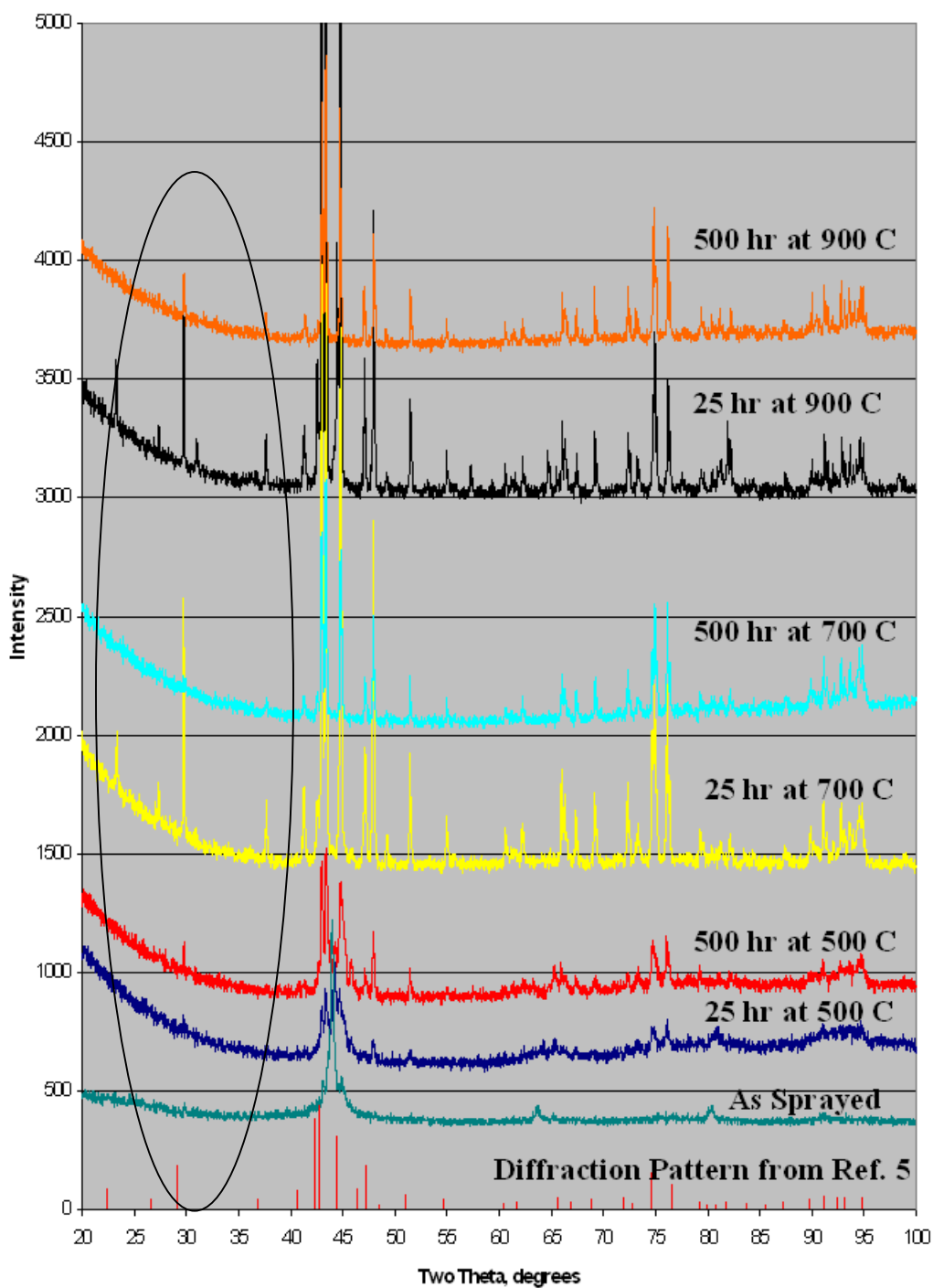


*Figure 5.3-3. XRD patterns for BT1 quasicrystal material are shown for the various diffusion couples after exposure at temperature. Note the peaks that begin to appear in the 500 hr at 500 °C scan in the 20 to 35 2-theta range. These peaks appear strongly in the 25 hr at 700 °C and 25 hr 900 °C samples but have nearly disappeared in the 500 hr 700 °C and 900 °C samples.*

Instrumented indentation hardness of the 500°C samples sprayed on the various substrates was lower than the starting powder, as shown in Figure 5.3-4, due to the coating structure (microcracks and porosity). The coating modulus measured with the Vickers indenter was close to the powder modulus at 25 hours, indicating the as-deposited BT1 QC material is similar to the starting powder. The magnitude increase of the Vickers modulus in the 100- hour samples is unexpected as it is higher than that of the powder or bulk material. This may be due to compositional changes to the BT1 resulting from the phase precipitation seen in the 500-hour sample (Figure 5.3-2e) that result in structure changes in the matrix. However, it is unclear as to why the modulus decreases at 500 hours to near the starting powder value.

700°C Samples – The microstructure of the BT1 QC coating with 25 hours of exposure at 700°C appeared to have fewer microcracks than the 500°C samples, as shown in Figure 5.3-5. At 500 hours of exposure there was a definite reduction in the amount of small microcracks and what appear to be a growth or consolidation of the lamellar coating structure, Figure 5.3-5b and d. A second phase could also be seen in the 500-hour microstructure at high magnification, similar to that seen in the 500°C sample, but the former being larger in size, Figure 5.3-5d. SEM EDS analysis of the precipitate again indicated high Cr and Co compared to the BT1 QC bulk analysis.

The results from hardness and modulus measurements on the 700°C samples are summarized in Figure 5.3-6. The hardness was close to that for the 500°C samples and is lower than the powder hardness due to the coating structure. The Vickers modulus at 25 hours was higher than the powder modulus just as the 100-hour samples at 500°C. This may be due to the initial precipitation of the phase visible in the 500-hour samples. The spherical indenter also gave a higher modulus for one 100-hour sample than the starting powder. The spherical modulus for the other 700°C samples were similar to the 500°C samples or slightly higher, as would be expected as the microcracking features were reduced.

The XRD patterns for the samples held at 700°C are shown in Figure 5.3-3. The 25-hour sample showed a pattern that is similar to the annealed powder and reference diffraction patterns, while for the 500-hour sample the peaks in the 20 to 40 2-theta range were reduced in intensity or disappeared. This may be due to the precipitation and growth of the precipitates seen in the SEM micrographs and correlates with the changes in Vickers hardness.

900°C Samples – At the 900°C exposure, considerable microstructural changes occurred particularly in the 500-hour samples as shown in Figure 5.3-7. At 25 hours the microcrack density was reduced and there appeared to be some consolidation of the

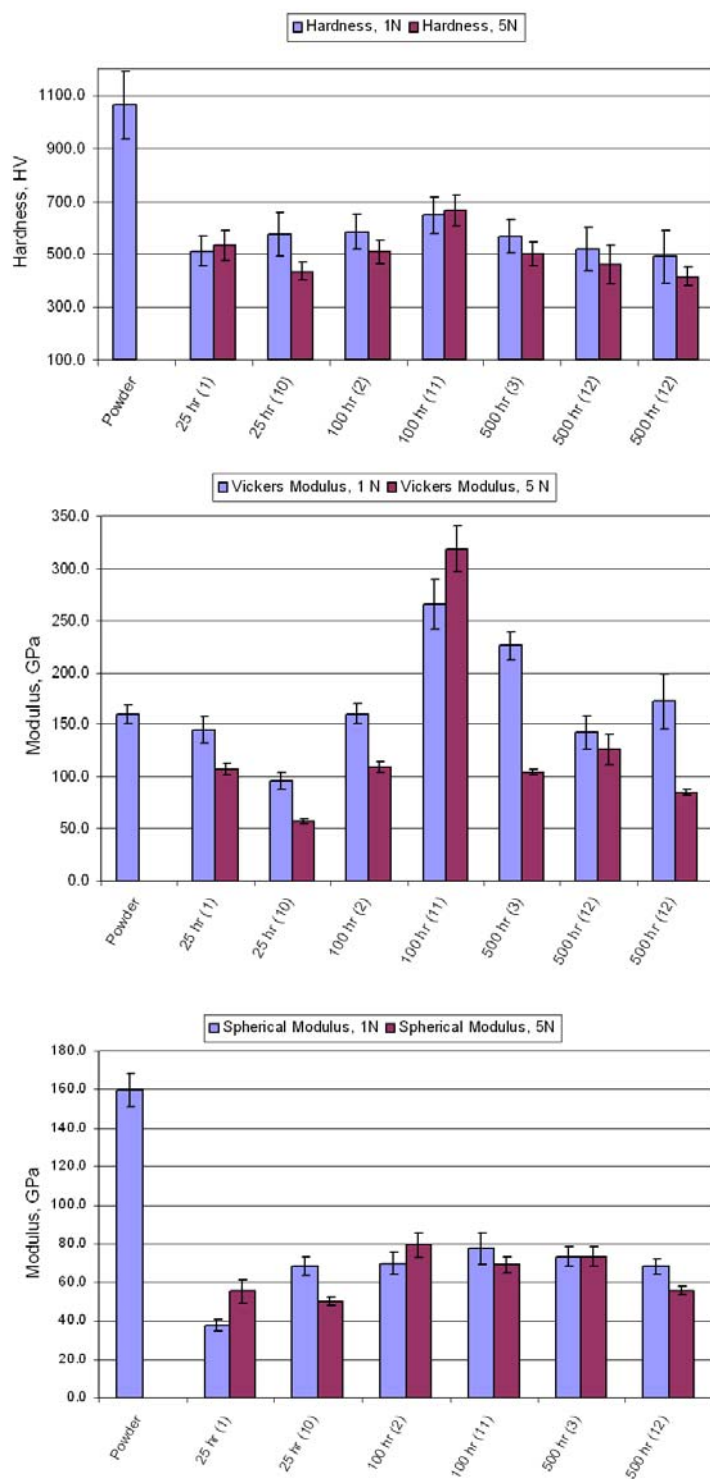
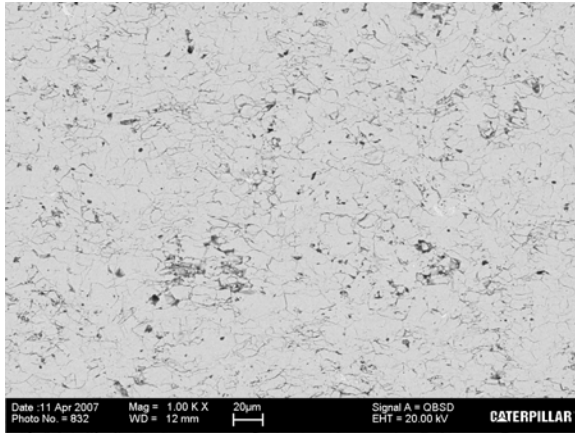
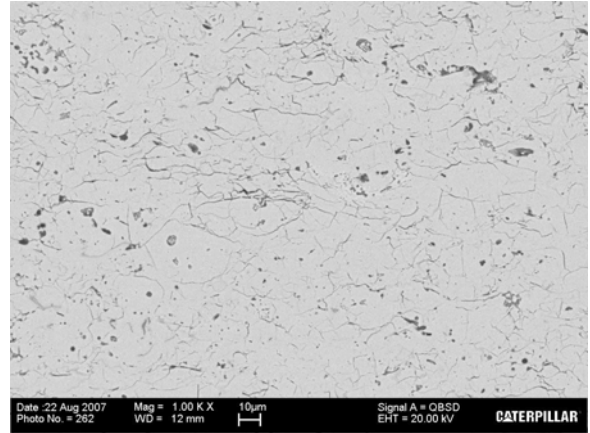


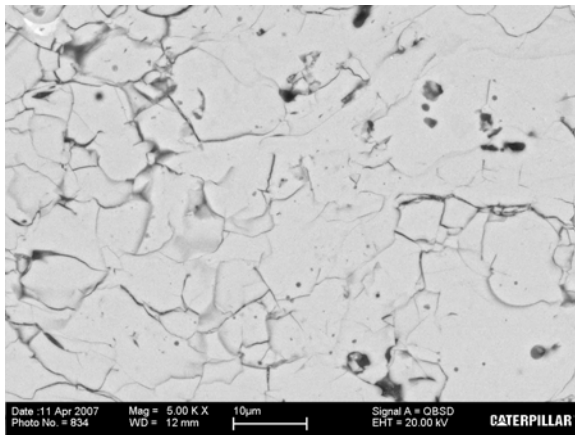
**Figure 5.3-4. Hardness (top), Vickers modulus (middle) and spherical modulus (bottom) of 500 °C BT1 QC coating samples measured by instrumented indentation are shown. Error bars indicate one standard deviation for the 10 measurements on each specimen.**



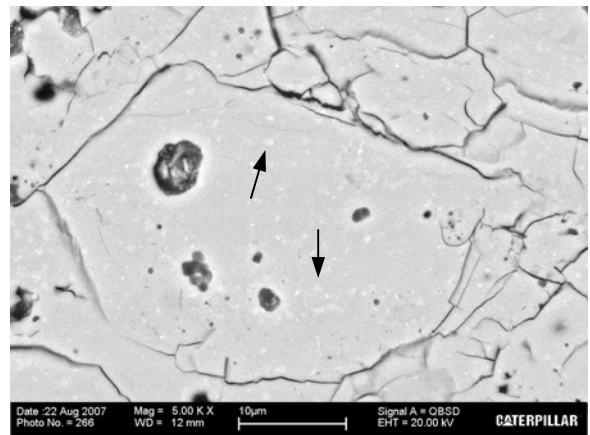
(a)



(b)



(c)



(d)

**Figure 5.3-5. Microstructure of BTI QC coating exposed at 700 °C for 25 hours (a,c) and 500 hours (b,d) showing porosity and microcracking density decreasing with increase time at temperature. The 500 hour microstructure has precipitates (indicated by arrows in d) similar to those in the 500 °C-500 hour sample but are large (visible at 5000X as compared to the 10,000X for the 500 °C sample in Figure 5.3-2).**

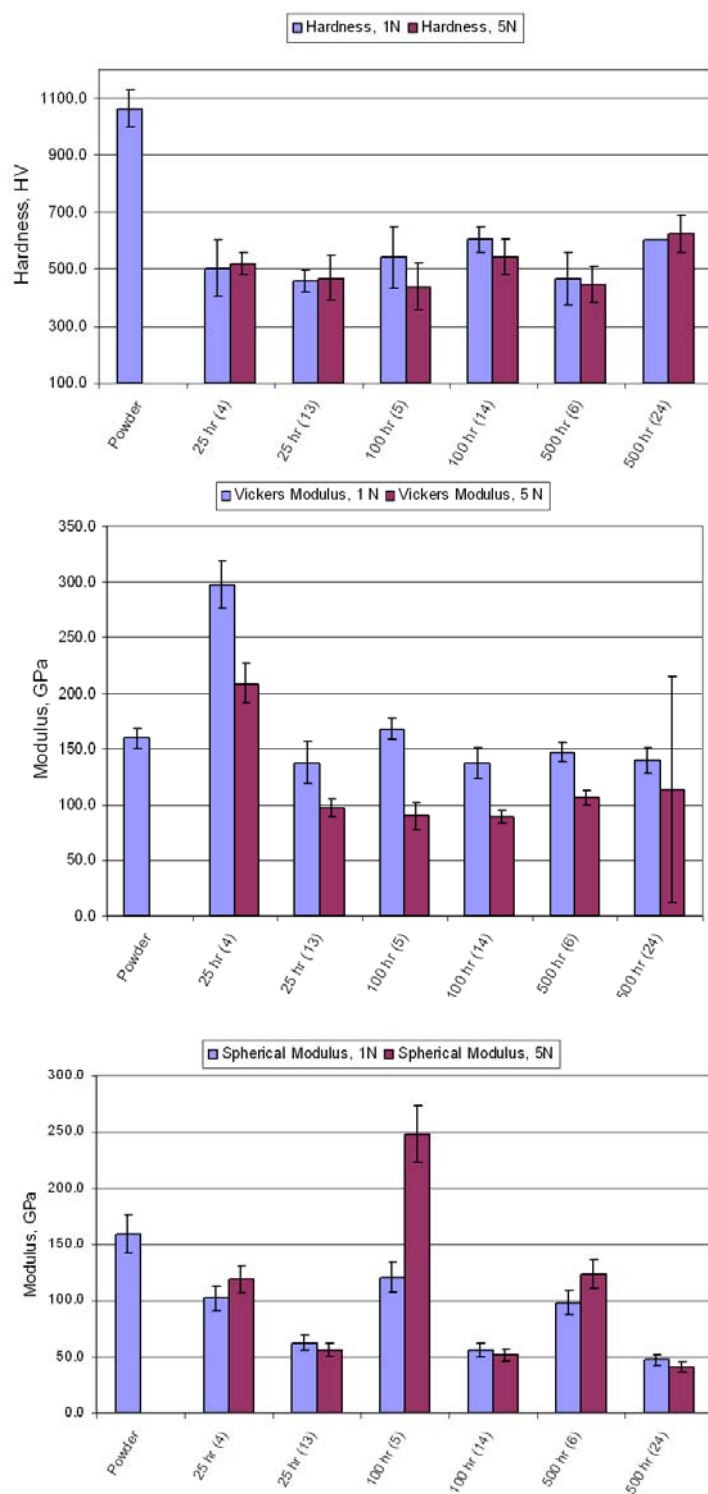
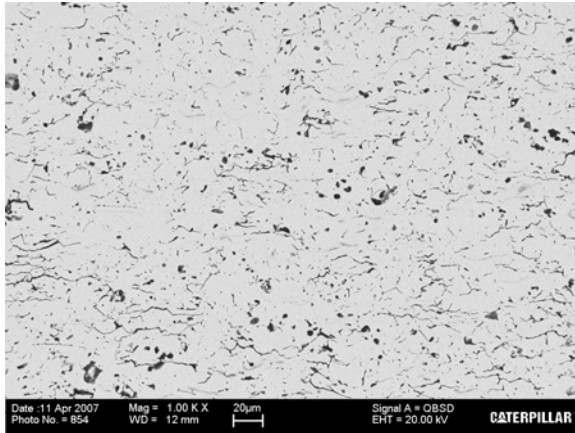
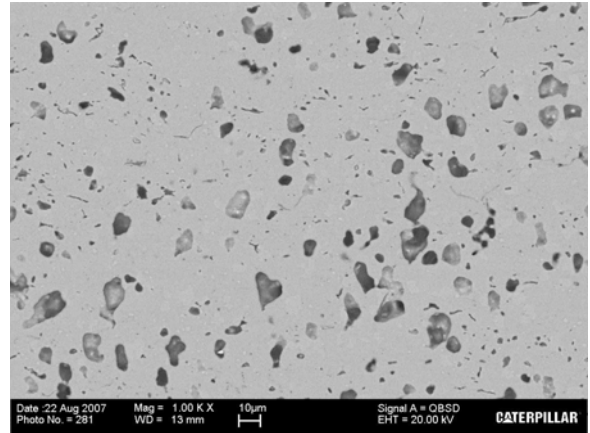


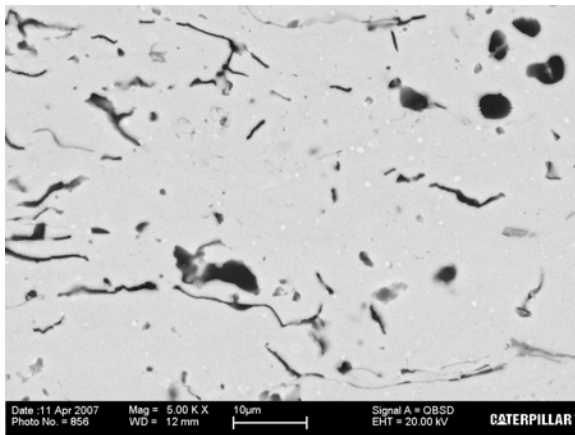
**Figure 5.3-6.** Hardness (top), Vickers modulus (middle) and spherical modulus (bottom) of 700 °C BT1 QC coating samples measured by instrumented indentation are shown. Error bars indicate one standard deviation for the 10 measurements on each specimen.



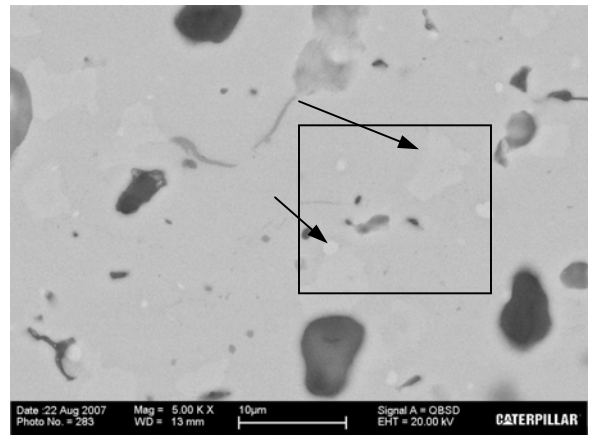
(a)



(b)



(c)

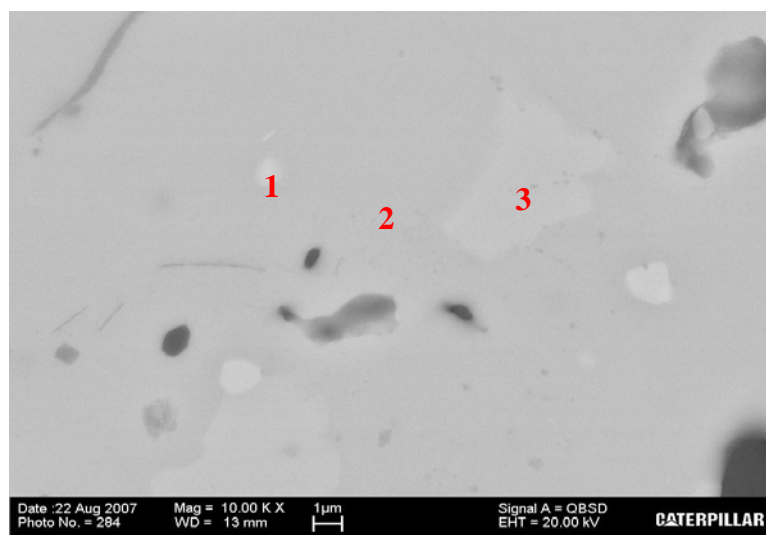


(d)

**Figure 5.3-7. Microstructure of BT1 QC coating exposed at 900 °C for 25 hours (a,c) and 500 hours (b,d) showing decrease porosity and microcracking density at 25 hour compared to the as-sprayed coating and nearly complete microcrack elimination at 500 hours with coalescences of the porosity (b,d). The 500 hour microstructure has precipitates (indicated by arrows in d) similar to those in the 500 °C-500 hour and 700C-500 hour sample but again are coarser than those at the lower temperatures.**

microcracks into round pores taking place. This was definitely evident in the 500-hour sample, where most of the microcracks had consolidated into round porosity and the lamellar structure of the coating was almost eliminated. The presence of large precipitates in the 500-hour microstructure were clearly evident and were large enough for quantitative analysis by SEM EDS. The resulting analysis is shown in Figure 5.3-8 and correlates with non-quantitative analysis of the small precipitates seen in the lower temperature microstructures.

As the phase precipitation did occur at the lower temperature as well as at 900°C complicates the interpretation of the hardness and modulus measured by the instrumented micro-indentation. The dramatic change in the coating structure at 900°C further complicates this interpretation. The hardness and modulus for the 900°C samples are shown in Figure 5.3-9. The hardness for the 900°C samples is slightly higher than the 500°C samples as a result of the microcrack elimination and the large porosity that is developed. The Vicker modulus again is higher than the starting powders at the low exposure times probably due to the phase precipitation. The spherical modulus reflects the high porosity developed in the coating microstructure and is similar to the 500°C samples.



<i>Location Number</i>	<i>Al at%</i>	<i>Cr at%</i>	<i>Fe at%</i>	<i>Co at%</i>
<i>Bulk BT1 QC composition</i>	71.5	7.8	7.8	12.9
<i>1</i>	56.25	31.19	5.11	7.45
<i>2</i>	70.48	6.68	8.79	14.05
<i>3</i>	57.27	29.45	5.15	8.13

**Figure 5.3-8.** Higher magnification of boxed area in Figure 5.3-9d showing location of EDS analysis shown in table. The lighter areas show an increase in chromium and a relative increase in iron and cobalt relative to the surrounding matrix.

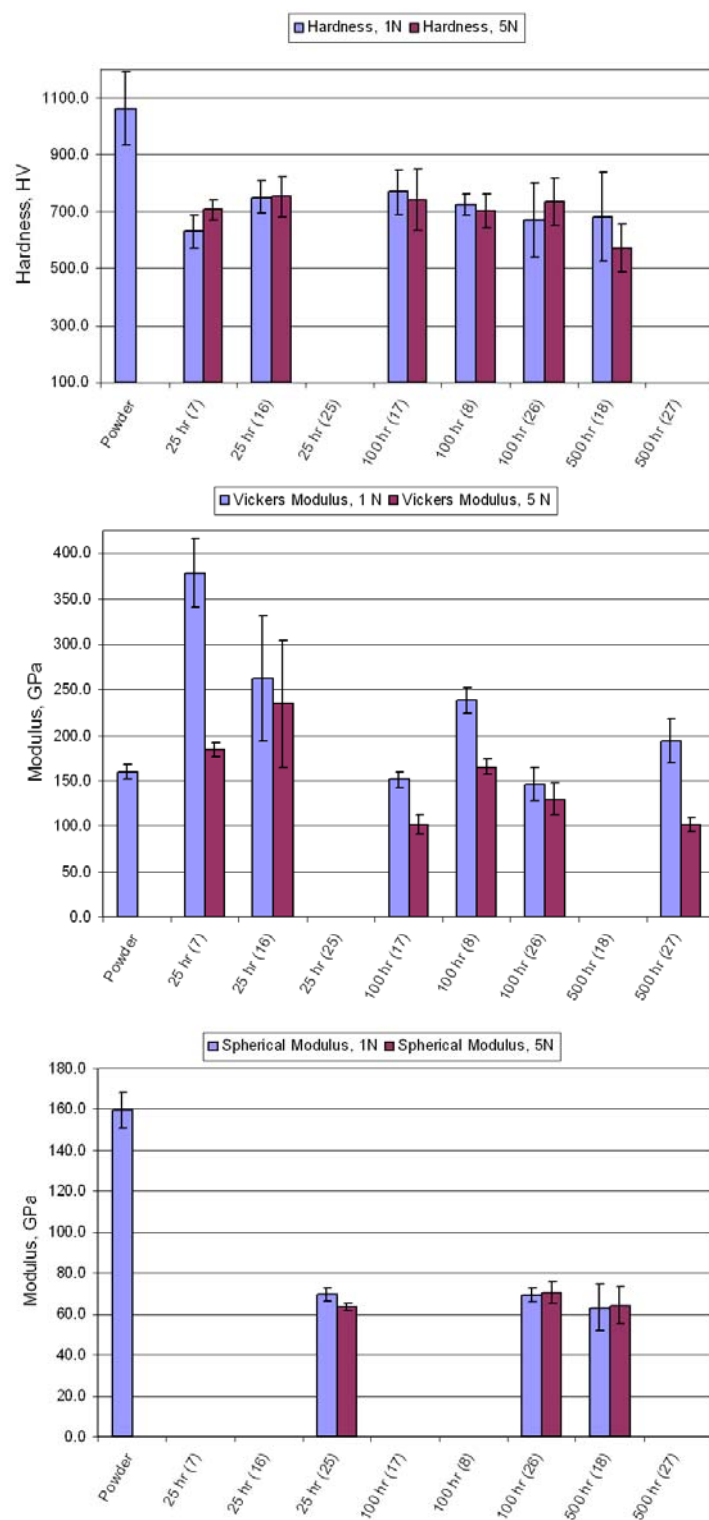


**Figure 5.3-9. Hardness (top), Vickers modulus (middle) and spherical modulus (bottom) of 900 °C BT1 QC coating samples measured by instrumented indentation are shown. Error bars indicate one standard deviation for the 10 measurements on each specimen.**

## 5.4 Quasicrystal and Substrate/Bond Coat Interaction

The two types of coating samples, BT1 QC on bond coat and BT1 QC on SAE 1040 (hereafter called diffusion couples), showed different behaviors at the 700°C and 900°C exposure temperatures. At 700°C and 900°C, all of the bond coat couples showed a significant interaction zone between the BT1 QC while the SAE 1040 couples showed little reaction zone at 700°C and a large reaction zone at 900°C. At 500°C the interface between the BT1 and both bond coats and SAE 1040 substrate showed little change. No analysis of the bond coat and steel substrate was done, as the BT1 QC interaction is the main interest of this study. Results for each diffusion temperature follows for the samples.

**500°C Diffusion Temperature** – The microstructure of the interface between the BT1 QC and SAE 1040 substrate and bond coats showed little change from the as-sprayed coating structure at 500 hours exposure, as shown in Figure 5.4-1.

Microprobe analysis at the interface between the BT1 QC coating and the SAE 1040 substrate and bond coats showed small diffusion distances of the species even after 500 hours, as shown in Figure 5.4-2. The average of the microprobe measurements through the thickness of the BT1 QC coating agreed well with the ICP chemical analysis for the starting powder, as shown in Table 5.4-1. The average of the measurements in the bond coatings and the SAE 1040 substrate also showed small variations from the nominal chemistries.

**Table 5.4-1. Average microprobe analysis (MP) of the BT1 QC, SAE 1040 substrate, and bond coat materials are shown. The BT1 QC microprobe analysis agrees well with the ICP analysis shown in Table 5.1-1 for the elements included in the analysis. The substrate and bond coat analysis also agrees well with the nominal compositions specified for the materials.**

Element	BT1 QC		Ni-17Cr-6Al-0.5Y		Ni-31Cr-11Al-0.6Y		Fe-26Cr-8Al-0.4Y		SAE 1040	
Wt%	IPC	MP	Nominal	MP	Nominal	MP	Nominal	MP	Nominal	MP
Al	54.2	51.53	6	5.91	11	11.03	8	7.72	-	0
Co	21.3	21.77	-	0.02	-	0.03	-	0.14	-	0.14
Fe	12.3	12.89	-	0.05	-	0.15	65.6	64.35	99.25	97.96
Cr	11.4	10.86	17	17.55	31	31.67	26	23.16		1.06
Ni	0.51	0.09	76.5	73.21	57.94	56.16	-	0.11		0.07
Mn	0.02	0.05	-	0.03	-	0.07	-	0.13	0.75	0.94

**700°C Diffusion Temperature** – A phase developed at the interface of the Fe26Cr8Al0.4Y-BT1 couple at 25 hours and thickened with increase exposure time as shown in Figure 5.4-3b, d, and f. No phase was seen in the SAE 1040-BT1 couple even after 500

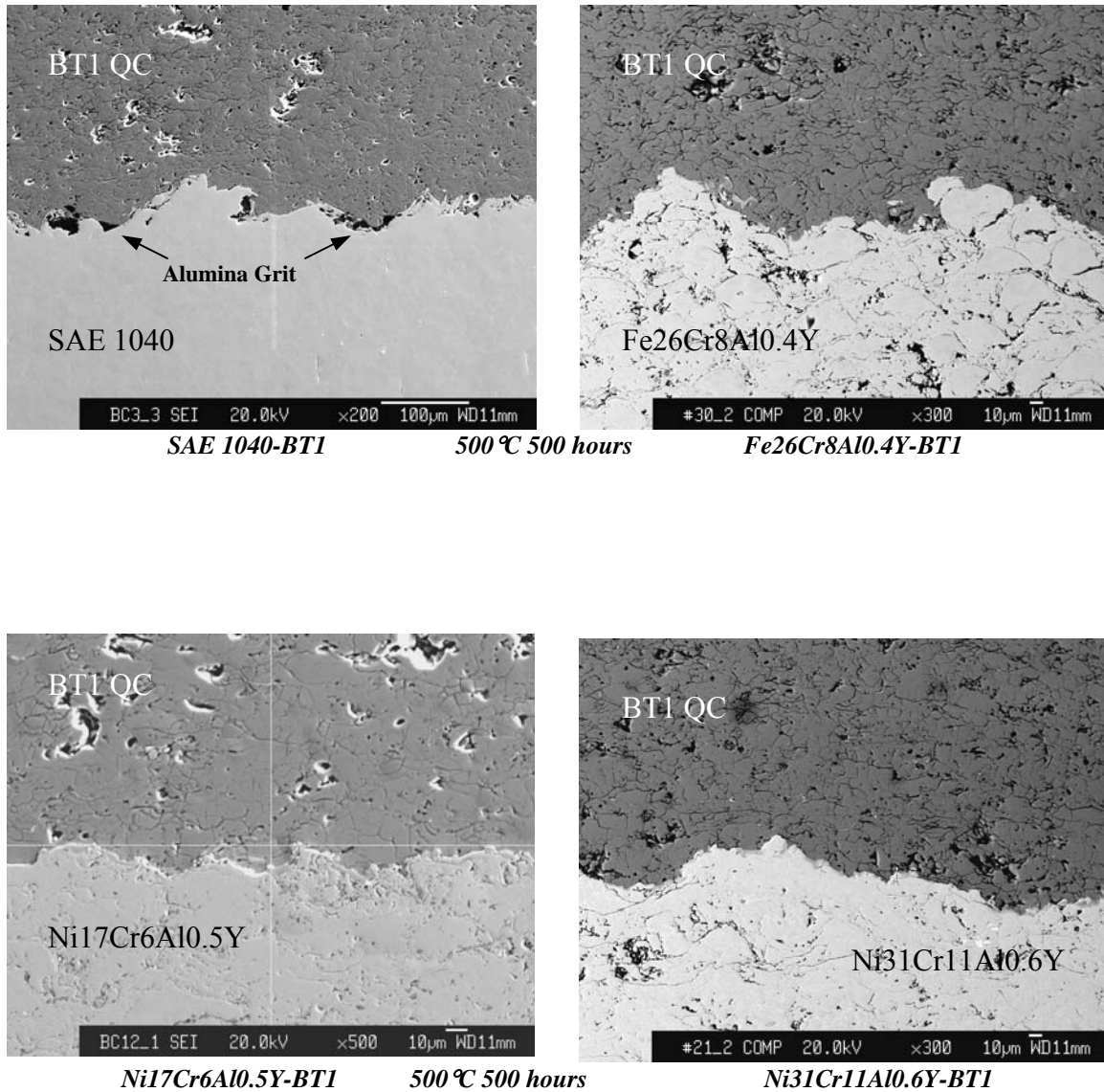


**Figure 5.4-1. Interface between the BT1 QC coating and the SAE 1040 steel substrate and bond coats showing little change after exposure at 500 °C for 500 hours. Embedded alumina grit from the surface prep is visible in the SAE 1040-BT1 couple. As the bond coats were not grit blasted prior to spraying the BT1 QC coating the interfaces of those couples do not have embedded grit.**

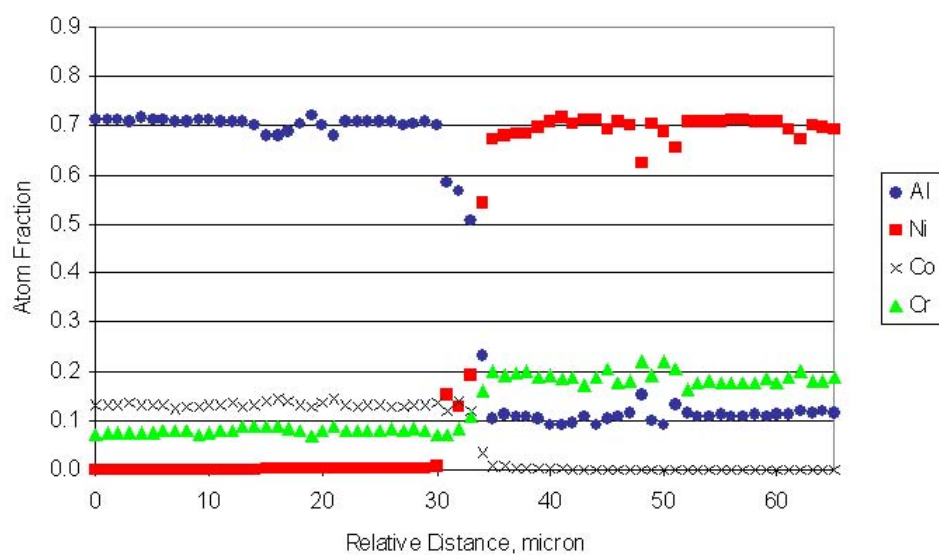
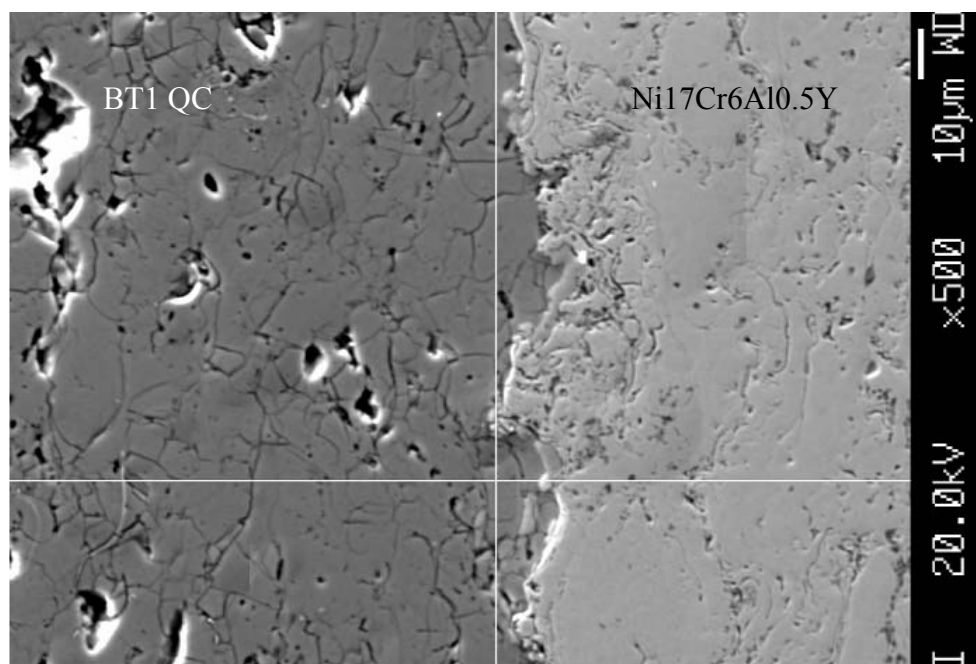


**Figure 5.4-2.** Microprobe concentration profile aligned with SEM image of microstructure of interface between the BT1 – Ni-17Cr-6Al-0.5Y bond coat at 500°C after 500 hours in showing the small diffusion at distances of the species. All of the couples showed similar small diffusion zones, on the order of 5 microns.

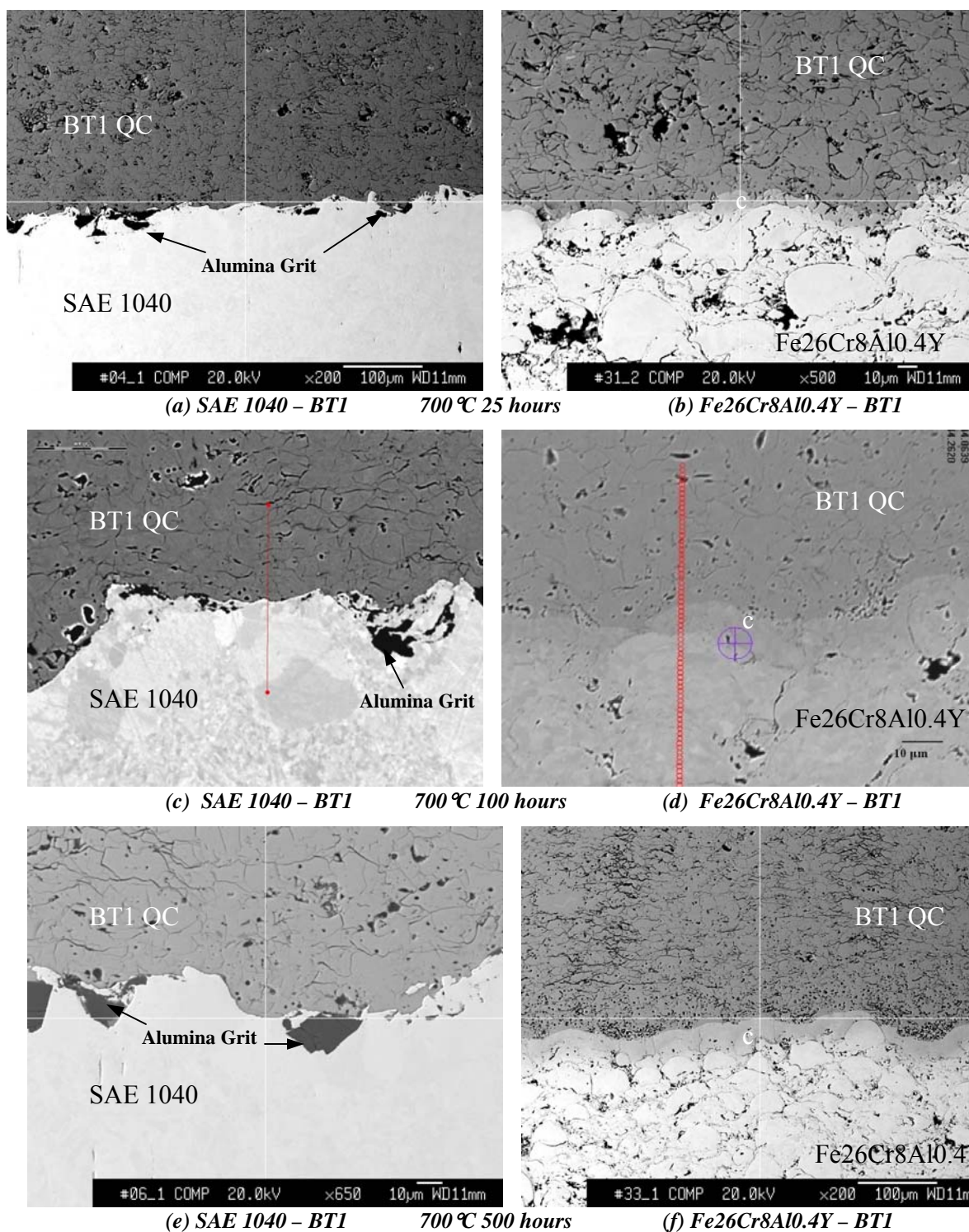


**Figure 5.4-3. Interface between the BT1 QC coating and the SAE 1040 steel substrate (left) and Fe<sub>26</sub>Cr<sub>9</sub>Al<sub>0.4</sub> bond coat (right) at 700 °C showing progression of interlayer phase in the Fe<sub>26</sub>Cr<sub>9</sub>Al<sub>0.4</sub>-BT1 couple (marked with "c" in photos). No interlayer phase is seen in the SAE 1040-BT1 couple even after 500 hours.**

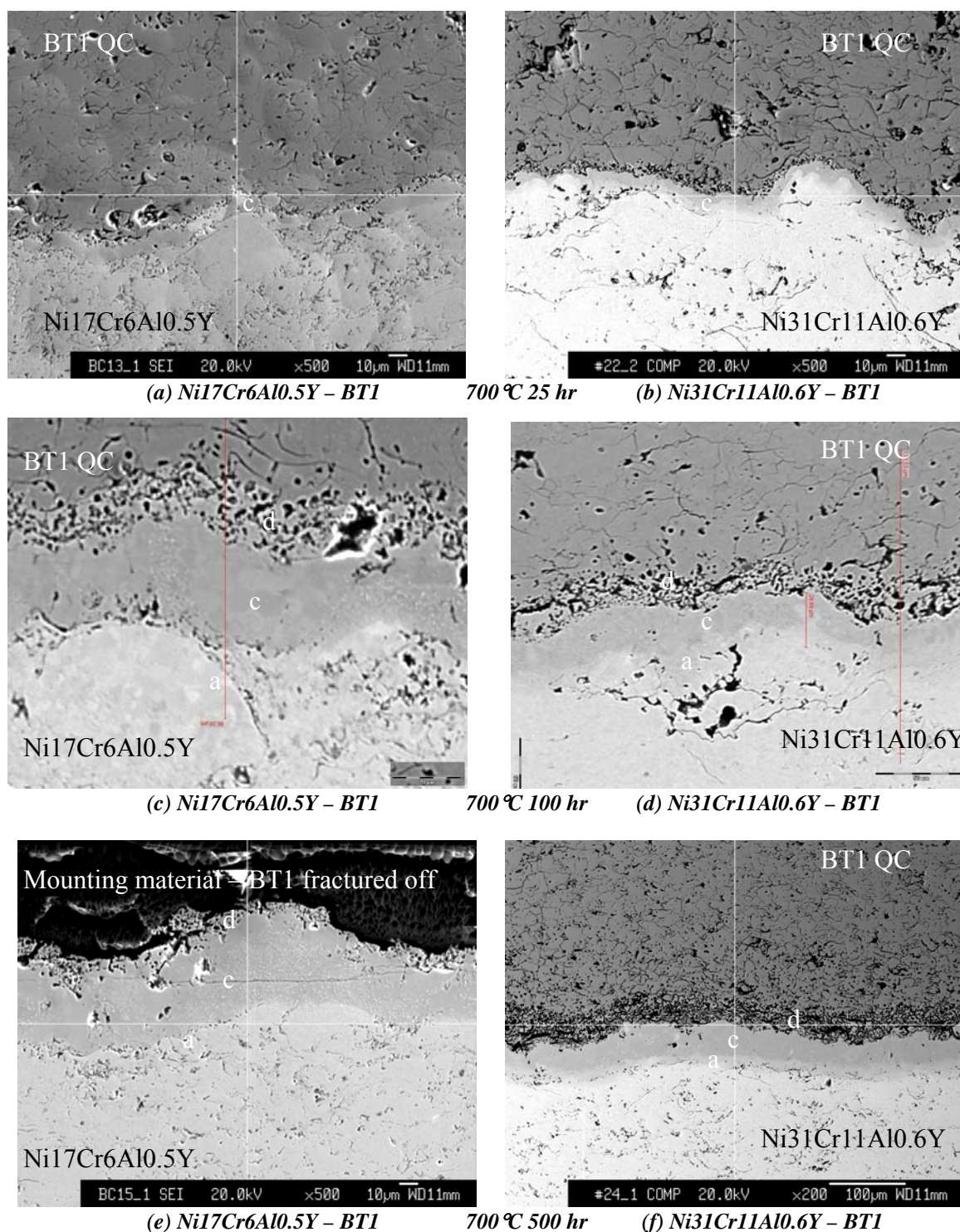


**Figure 5.4-4. Interface between the BT1 QC and the Ni17Cr6Al0.5Y (left) and Ni31Cr11Al0.6Y (right) bond coats at 700 °C showing progression of interlayer zone in both couples. An initial interlayer forms at 25 hours (c) that thickens with time. Kirkendall voids form on the BT1 side of the couples (d). A region appearing to be a diffusion zone (a) develops on the bond coat side of the couples.**

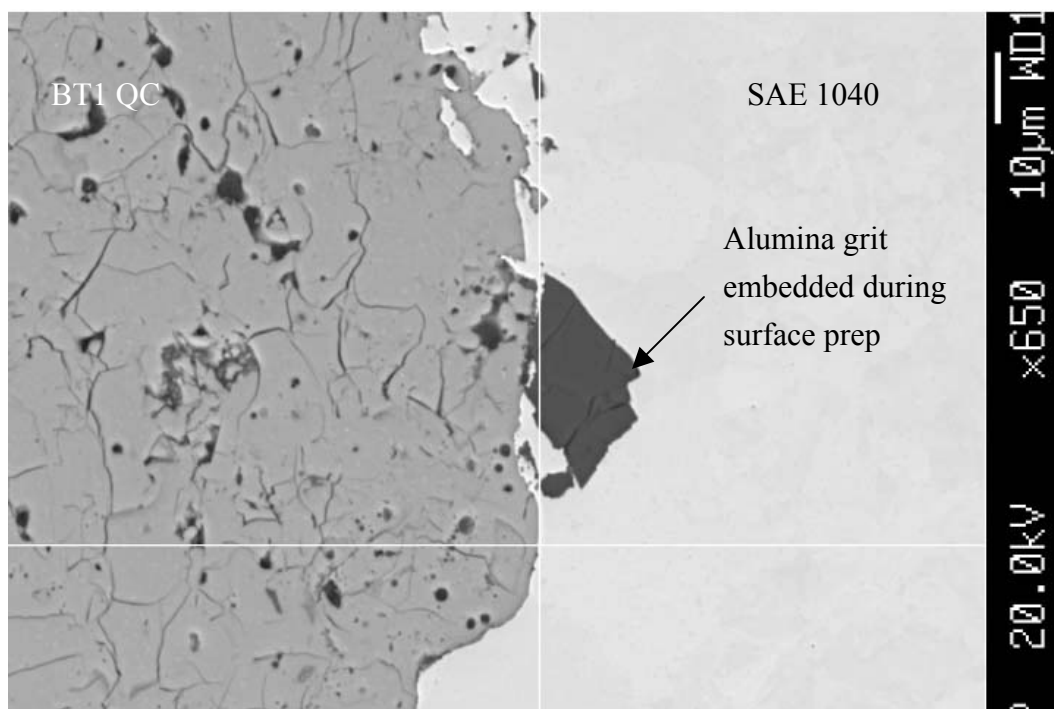
hours, Figure 5.4-3a, c, e. A similar phase developed in the Ni17Cr6Al0.5Y-BT1 and Ni31Cr11Al0.6Y-BT1 couples, Figure 5.4-4. In the Fe26Cr8Al0.4Y-BT1 couple, there appeared to be void formation in the 500-hour sample in the BT1 QC coating at the interface with the phase that had developed. In the Ni31Cr11Al0.6Y-BT1 couple shown in Figure 5.4-4b,f, voids appeared at 25 hours and progressively increased in number with time. There were indications of voids in the BT1 side of the interlayer in the 500-hour Ni17Cr6Al0.4Y-BT1 couple (Figure 5.4-4e), which may be why the BT1 QC coating fractured in this area on quenching from the 700°C exposure.

Microprobe analysis of the 700°C, 500-hour SAE 1040-BT1 couple shown in Figure 5.4-5 confirmed that there was no interface phase in this sample and that the diffusion distance for the species was similar to that of the 500°C SAE 1040-BT1 couple. The microprobe results for the 700°C, 500-hour Fe26Cr8Al0.4Y-BT1 couple shown in Figure 5.4-6 indicates that the interlayer phase ranges from ~40 to 50 at% aluminum. This would suggest that the phase is an iron aluminide, most likely FeAl<sub>2</sub>.

The microprobe analysis of the 700°C, 500-hour Ni17Cr6Al0.5Y-BT1 and Ni31Cr6Al0.6Y-BT1 couples shown in Figures 5.4-7 and 5.4-8 also indicate that the interlayer is ~50 to 55 at% aluminum with ~30 to 40 at% nickel. This would suggest that phase was NiAl. Cobalt increased in content at the interface of the phase that developed due to the decrease in aluminum content as it diffused into the interface phase as well as what appears to be diffusion up the cobalt concentration gradient, or “up-hill” diffusion.

900°C Diffusion Temperature – A phase developed at the interface of the SAE 1040-BT1 couple within the first 25 hours as shown in Figure 5.4-9a. Void formation was evident in the 25-hour microstructure of both the BT1 QC and the SAE 1040. Indications of aluminum diffusion into the steel can also be seen, feature “a” in Figure 5.4-9a,e. Specifically, the darker region below the interlayer indicated this diffusion region. This aluminum diffusion extended ~300 µm into the substrate after 500 hours. A phase also developed in the Fe26Cr8Al0.4Y-BT1 couple, but the void formation was mainly on the BT1 side of the phase that developed, Figure 5.4-9f. The void formation in the 500-hour BT1 coating in this couple probably led to the coating delamination when quenched from the 900°C exposure temperature.

Similar phase and void formation was seen in the Ni17Cr6Al0.5Y-BT1 and Ni31Cr11Al0.6Y-BT1 couples as shown in Figure 5.4-10. The void formation in the NiCr17Cr6Al0.5Y-BT1 couple was on both the BT1 and bond coat side of the interlayer phase while for the Ni31Cr11Al0.6Y-BT1 couple, the voids form only on the BT1 side of the phase. The interlayer phase had a composition on the bond coat side suggesting a β, NiAl



#6 substrate-BT1 700 deg 500 hrs

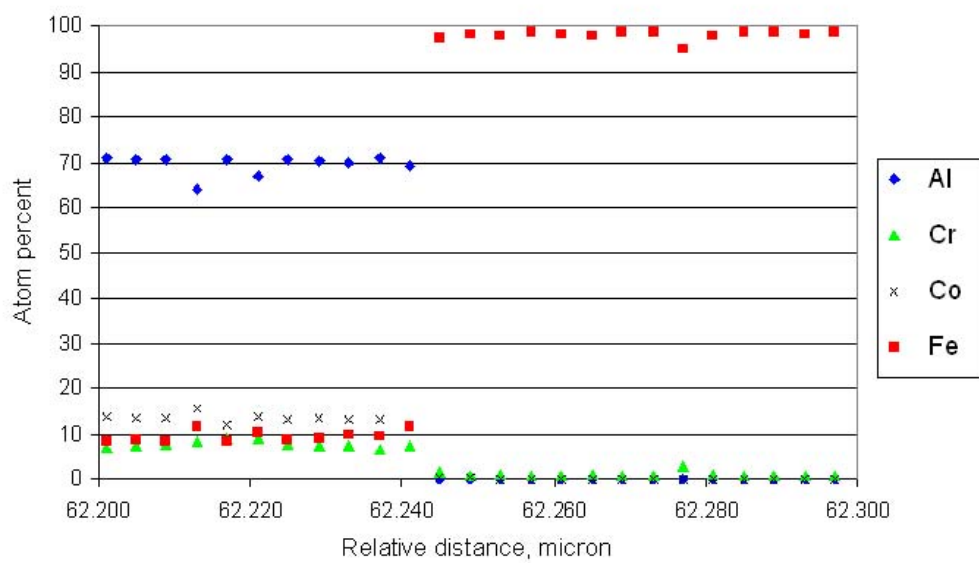


**Figure 5.4-5. Microprobe results for the 700 °C-500 hour SAE 1040-BT1 QC couple showing no interlayer phase and small diffusion distances for the species.**

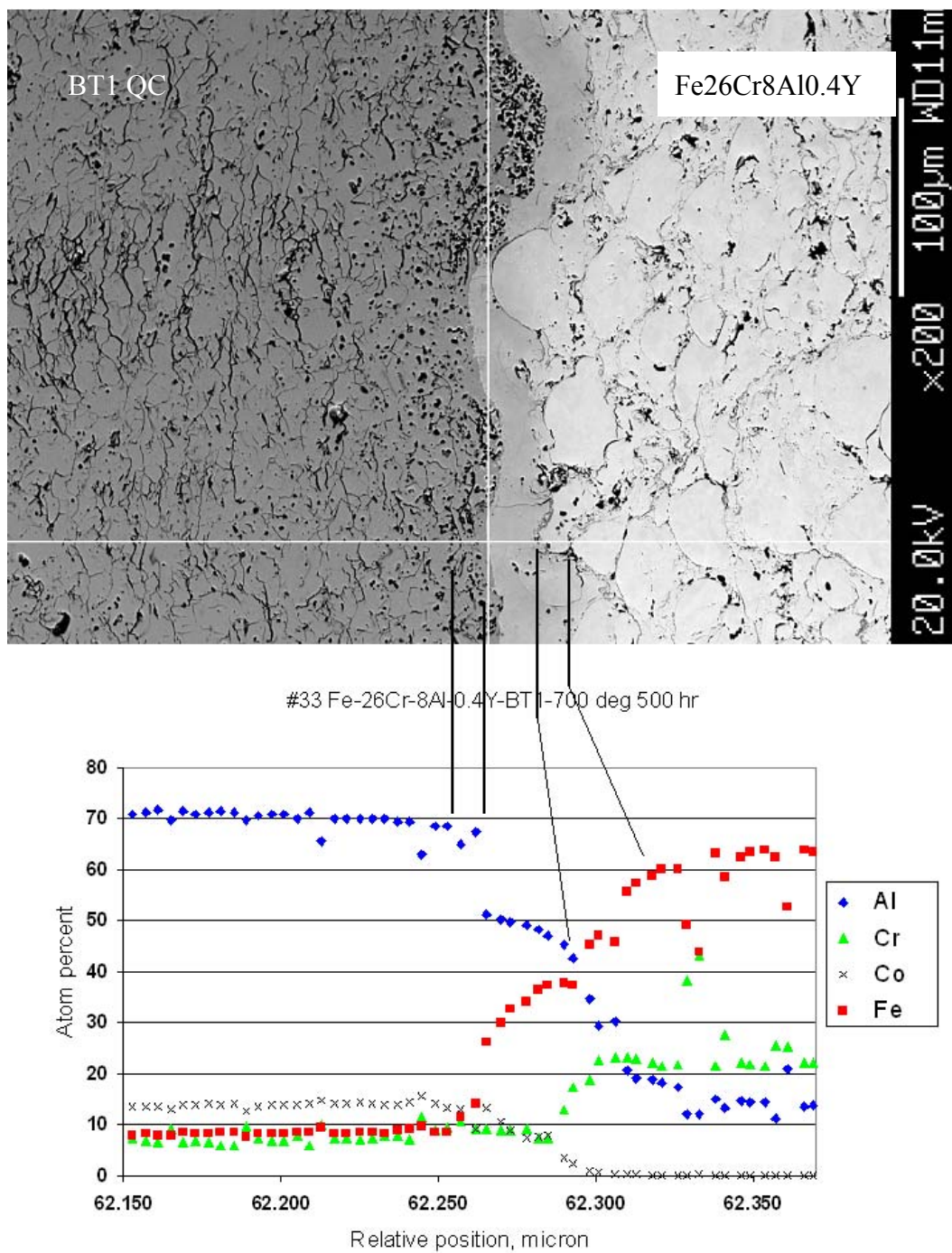


**Figure 5.4-6.** Microprobe analysis of the Fe26Cr8Al0.4Y-BT1 couple showing the interlayer phase to be aluminum and iron compound roughly equal to that of FeAl<sub>2</sub>.

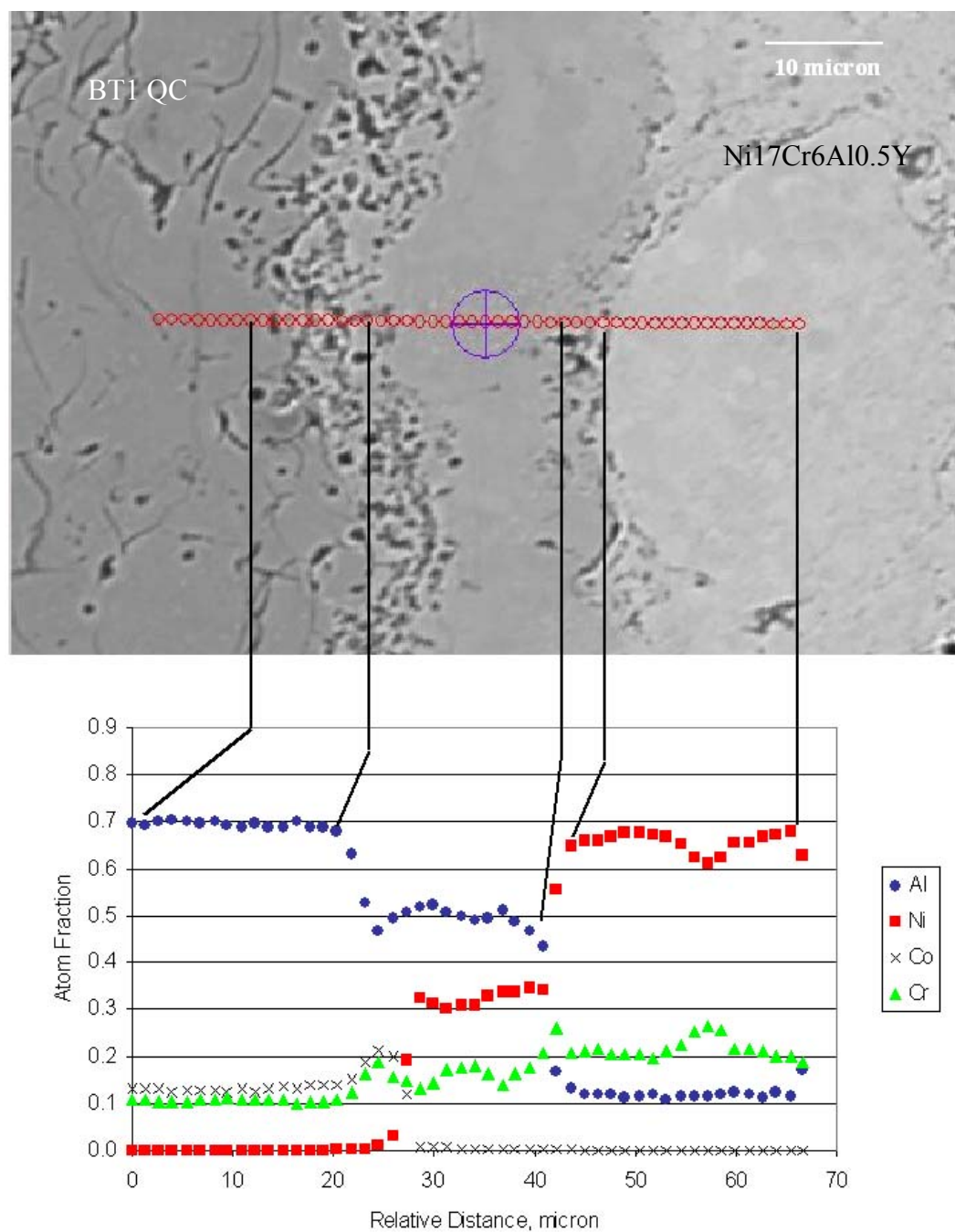


**Figure 5.4-7.** Microprobe concentration profile aligned with SEM image of microstructure of interlayer formed 700°C after 100 hours in BT1 – Ni17Cr6Al0.5Y bond coat showing how the concentration of aluminum and nickel align with the structure observed. The interlayer phase is seen to be primarily nickel and aluminum with a composition similar to  $Ni_2Al_3$ .

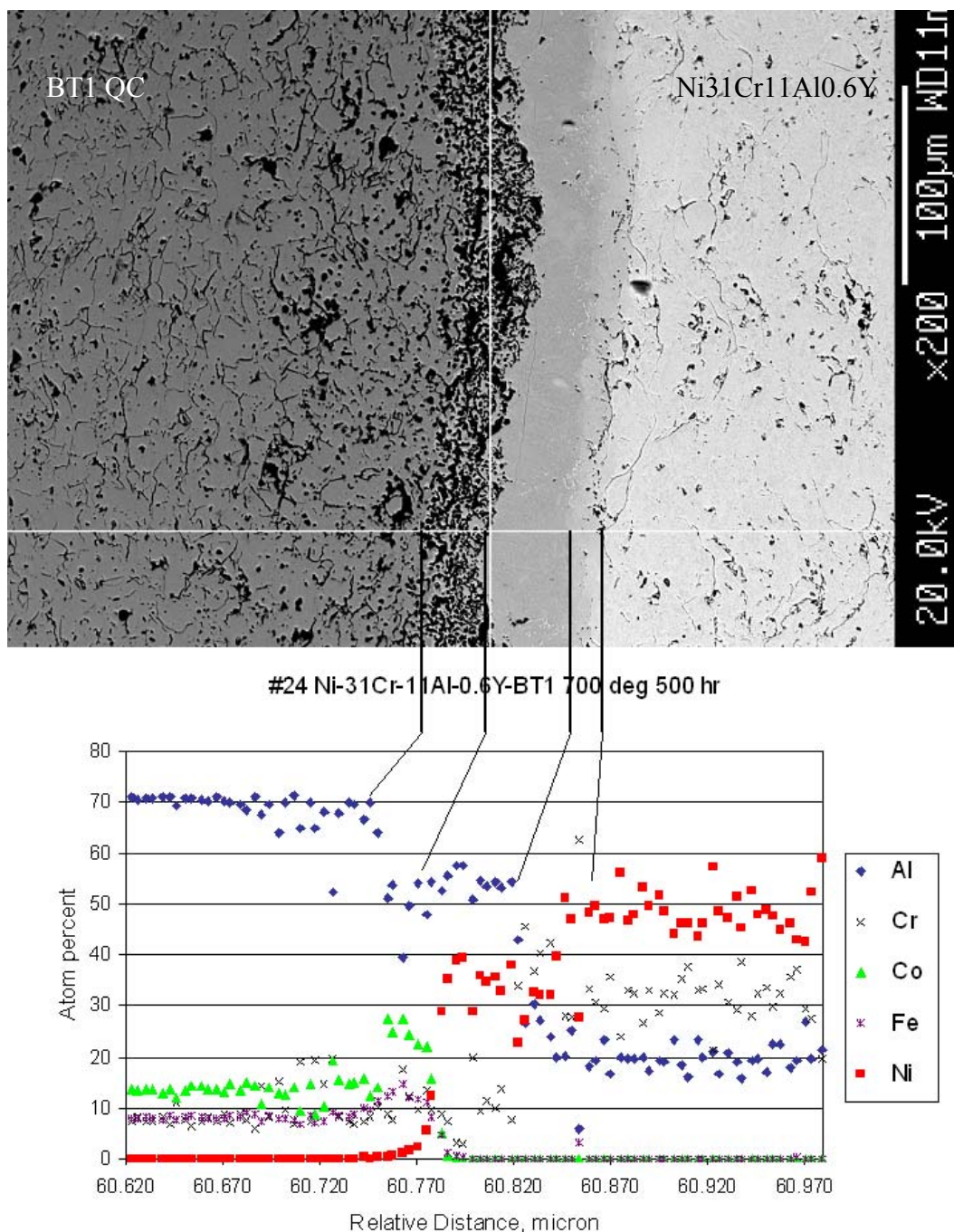


**Figure 5.4-8.** Microprobe concentration profile aligned with SEM image of microstructure of interlayer formed 700°C after 500 hours in BT1 – Ni17Cr6Al0.5Y bond coat showing how the concentration of aluminum and nickel align with the structure observed. The interlayer phase is seen to be primarily nickel and aluminum with a composition similar to  $\text{Ni}_2\text{Al}_3$ .

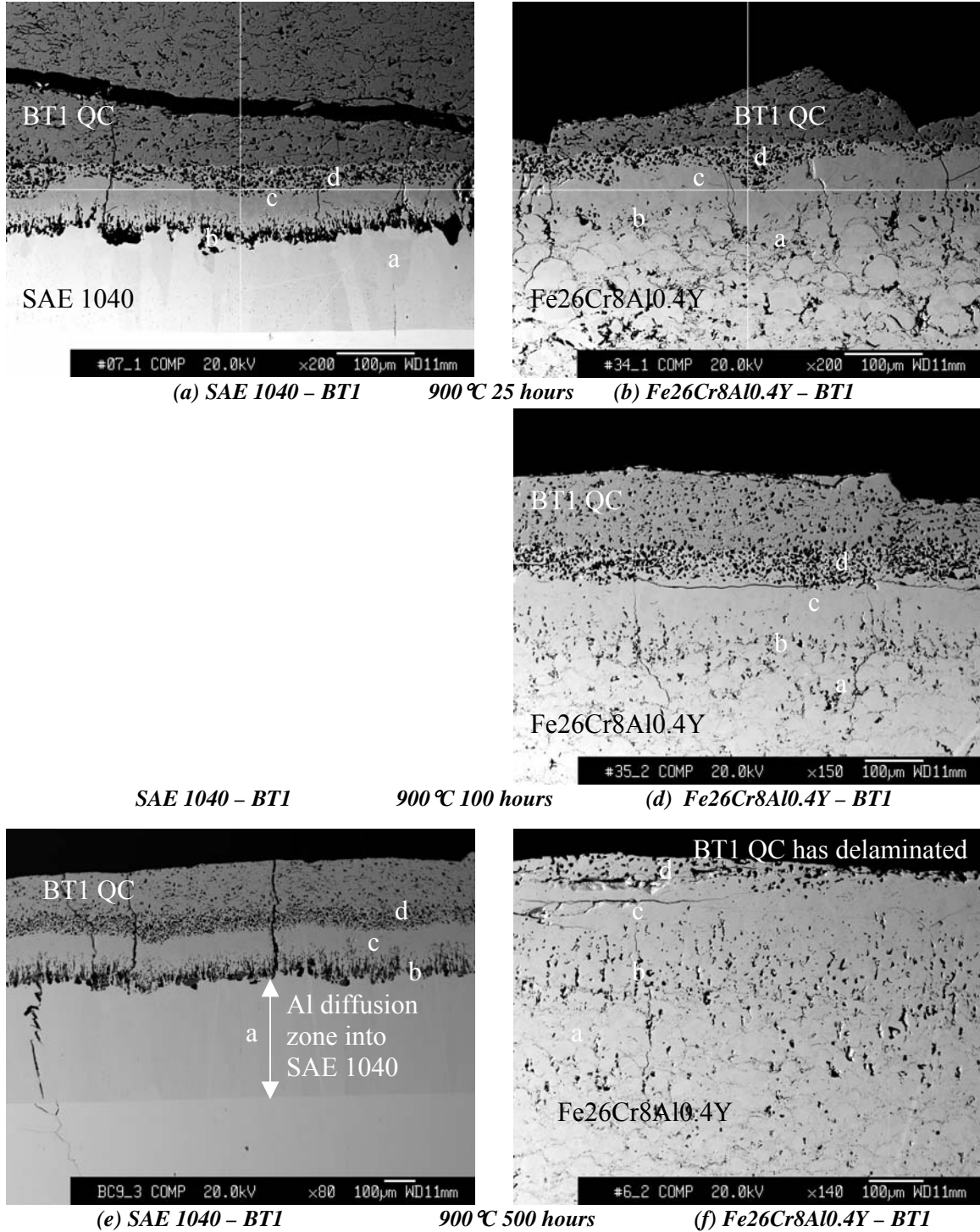


**Figure 5.4-9.** Interface between the BT1 QC and the SAE 1040 steel substrate (left) and Fe26Cr9Al0.4 bond coat (right) at 900 °C showing progression of interlayer zone in both couples. An initial interlayer develops in both couples at 25 hours that progressively thickens. Kirkendall voids developed on either side of the interlayer (b and d). A region appearing to be a diffusion zone (a) develops in both couples but is very visible in the SAE 1040 substrate.

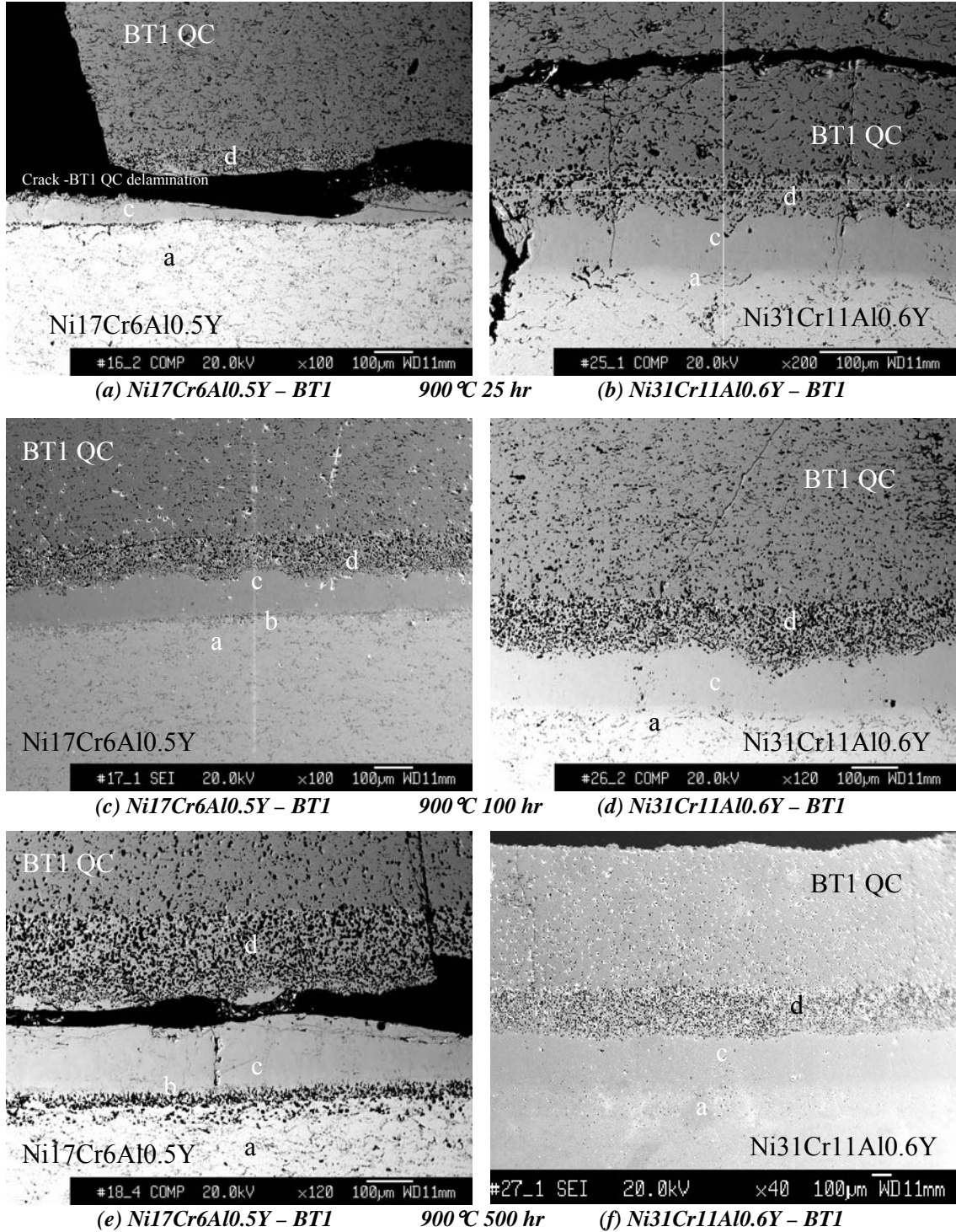


**Figure 5.4-10.** Interface between the BT1 QC and the Ni17Cr6Al0.5Y (left) and Ni31Cr11Al0.6Y (right) bond coats at 900 °C showing progression of interlayer zone in both couples. Both couples have an initial interlayer structure consisting of a solid layer with Kirkendall voids (d) in the BT1 QC. Voids also develop in the Ni17Cr6Al0.5Y bond coat (b) at the longer times but not in the Ni31Cr11Al0.6Y bond coat. A region appearing to be a diffusion zone (a) develops on the bond coat side of the couples.

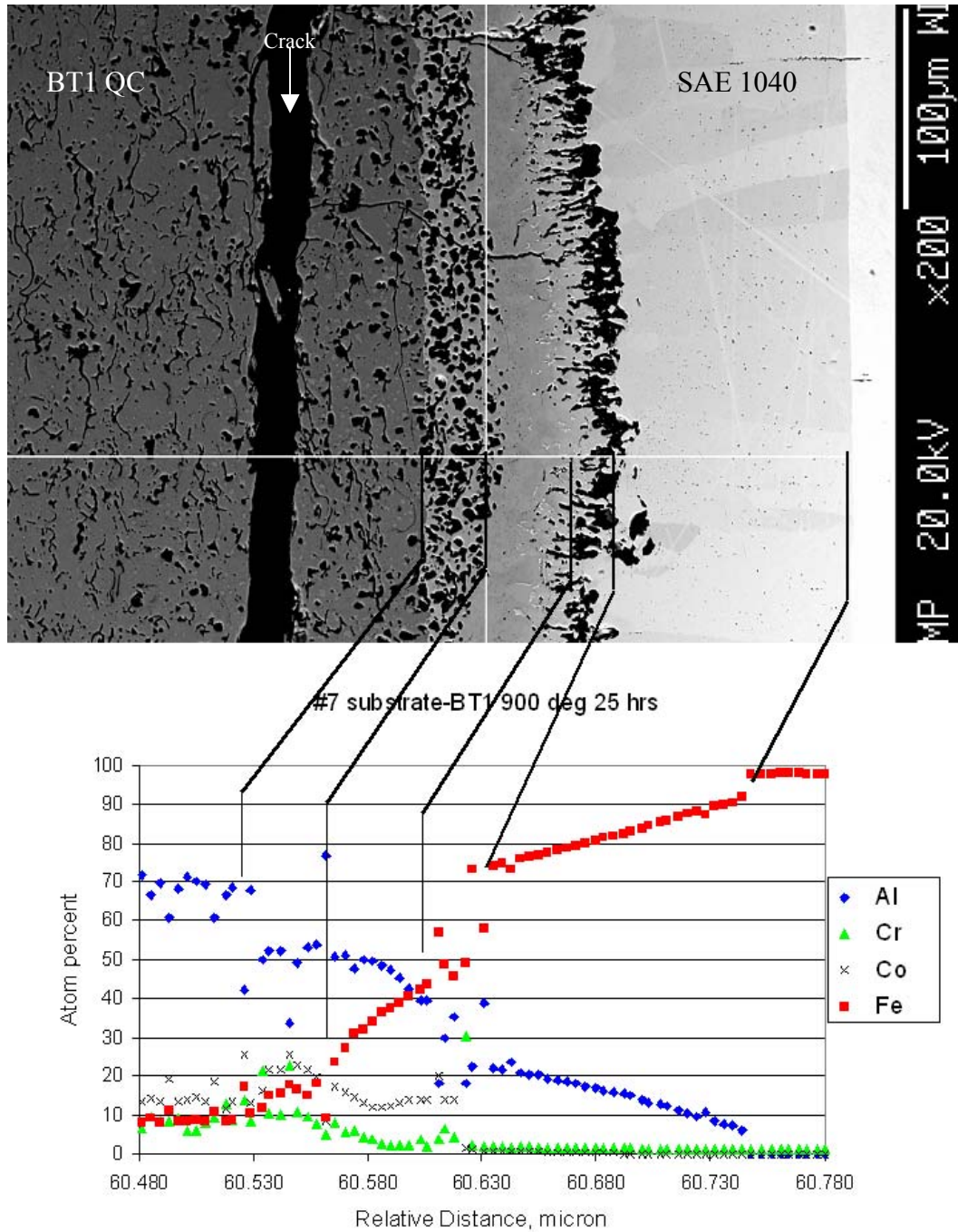


**Figure 5.4-11.** Microprobe concentration profile aligned with SEM image of microstructure of interlayer formed 900°C after 25 hours in SAE 1040-BT1 couple showing how the concentration of aluminum and iron align with the structure observed. The interlayer phase is seen to be primarily iron and aluminum with a composition similar to FeAl.

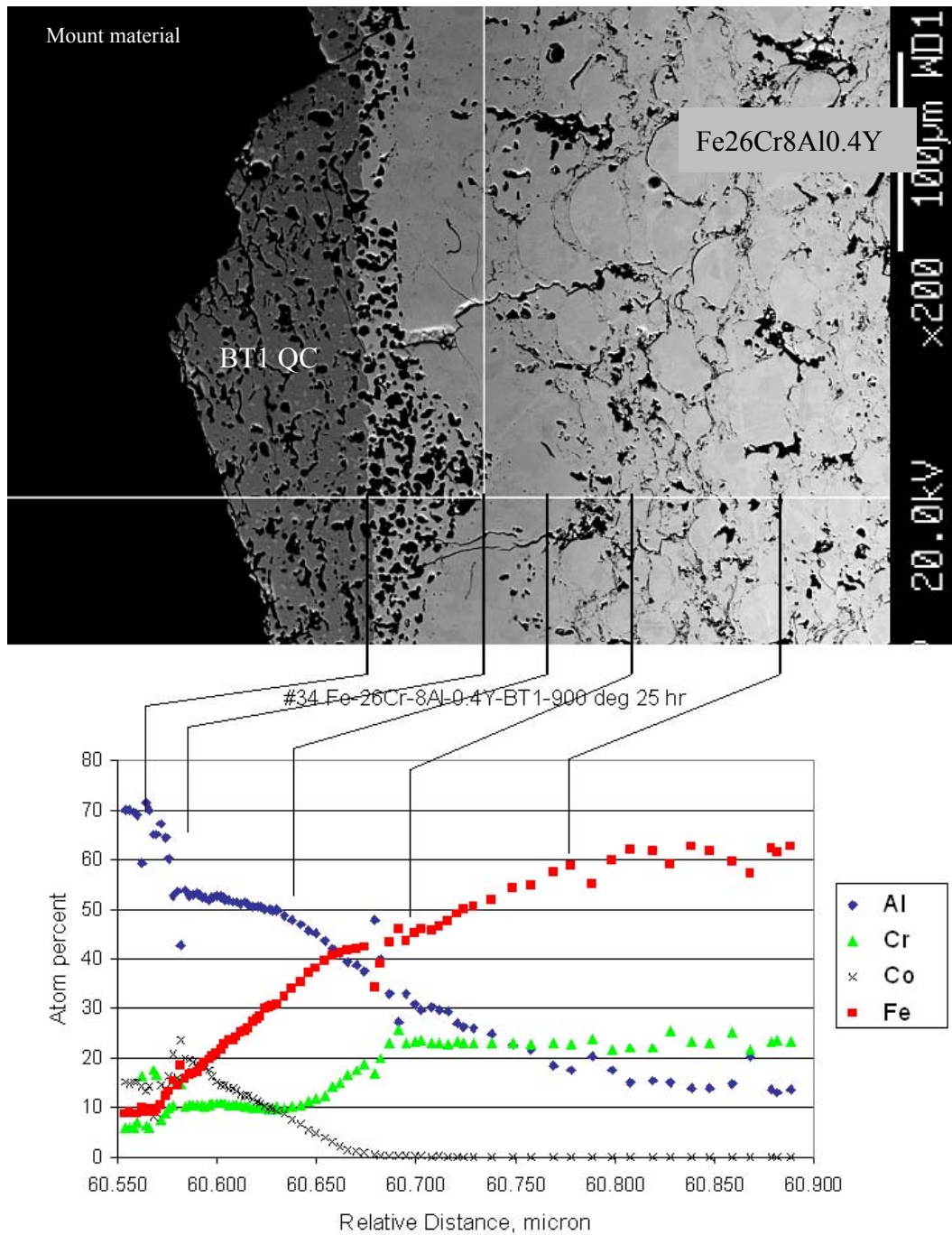


**Figure 5.4-12.** Microprobe concentration profile aligned with SEM image of microstructure of interlayer formed 900°C after 25 hours in Fe26Cr8Al0.4Y-BT1 couple showing how the concentration of aluminum and iron align with the structure observed. The interlayer phase is seen to be primarily iron and aluminum with a composition similar to FeAl.

phase while on the BT1 QC side in had a composition suggesting a  $\beta$  with (Co,Ni)Al composition.

Microprobe analysis of the 25-hour SAE 1040-BT1 and Fe26Cr8Al0.4Y-BT1 couples are shown in Figures 5.4-11 and 5.4-12. The analysis shows the interlayer phase in both couples contain ~40 to 50 at% aluminum and ~25 to 40 at% iron. This composition of suggests the FeAl aluminide phase. The cobalt content increased in the BT1 QC next to the interlayer phase. Microprobe analysis of the 25-hour Ni31Cr11Al0.6Y-BT1 couple is shown in Figure 5.4-13. The interlayer phase was ~125  $\mu\text{m}$  thick with voids formed in the BT1 QC. The composition of the solid portion of the interlayer contains ~55 at% aluminum and ~40 at% which indicates the phase to be NiAl. The portion of the interlayer next to the BT1 QC showed a decrease in nickel content with increasing cobalt, suggesting that this part of the interlayer phase is a combination of NiAl and CoAl.

Results from microprobe analysis of the 500-hour Ni31Cr11Al0.6Y-BT1 and Ni17Cr6Al0.5Y-BT1 samples are shown in Figures 5.4-14 and 5.4-15. Both profiles show similar interlayer phases of NiAl and (Co,Ni)Al compositions as the 25-hour Ni31Cr11Al0.6Y-BT1 sample. The Ni17Cr6Al0.5Y-BT1 sample showed void formation at both interfaces of the interlayer phase and the BT1 and the bond coat. Both samples also showed high scatter in the measurements due to the voids in the microstructure.

## 5.5 Interlayer Thickness Analysis

The total layer thickness or penetration into the BT1 QC and the bond coat or substrate was estimated from the SEM micrographs and the results are summarized in Table 5.5-1. The relative penetration into the aluminum-rich BT1 QC and the nickel/iron coatings gives an estimate of the mobility of the principal diffusing species. The depth of penetration for the aluminum and nickel was relatively equal for the NiCrAlY bond coat couples, indicating that the mobility of both the aluminum and nickel were relatively equal. In the case of the SAE 1040 and FeCrAlY bond coat couples, the penetration of the aluminum into the iron-base material was almost twice as high at 900°C, indicating higher aluminum mobility in the austenite iron. The relatively thin interlayer thickness found 500°C and 700°C indicates a change in the mobility with the austenite-ferrite phase change in the iron-based materials. This will be discussed in more detail in Section 6.

The layer thickness measured for the quasicrystal and bond coat/substrate side of the interlayer was somewhat subjective. The schematic in Figure 5.5-1 shows the major structures of the interlayer and how the measurements were taken. The dividing point for

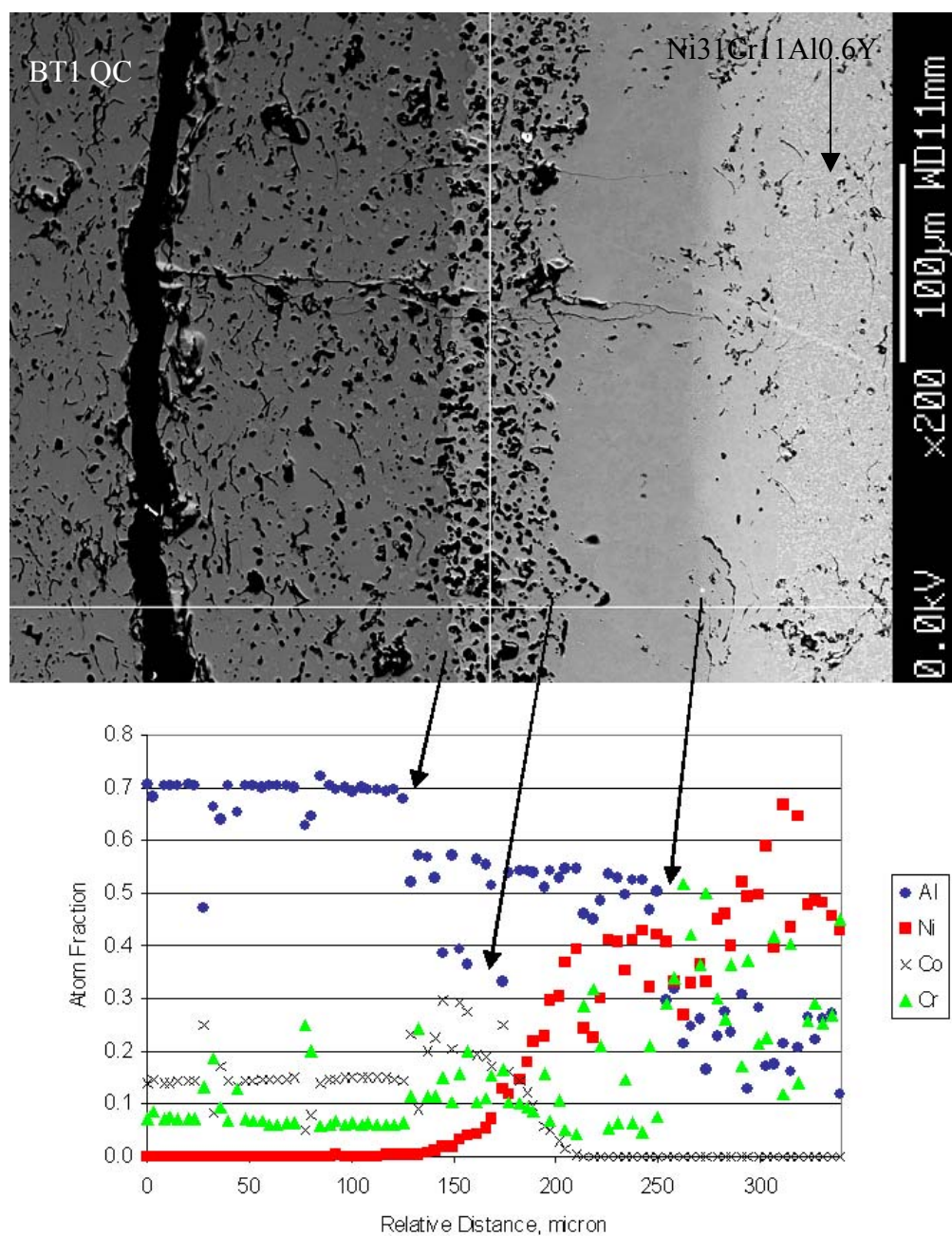


**Figure 5.4-13.** Microstructure of the Ni-31Cr-11Al-0.6Y and BT1 interface after holding for 25 hours at 900 °C. Note the formation of voids in the BT1 at the short diffusion time and the high scatter in the measured concentration of the nickel in the bond coat.

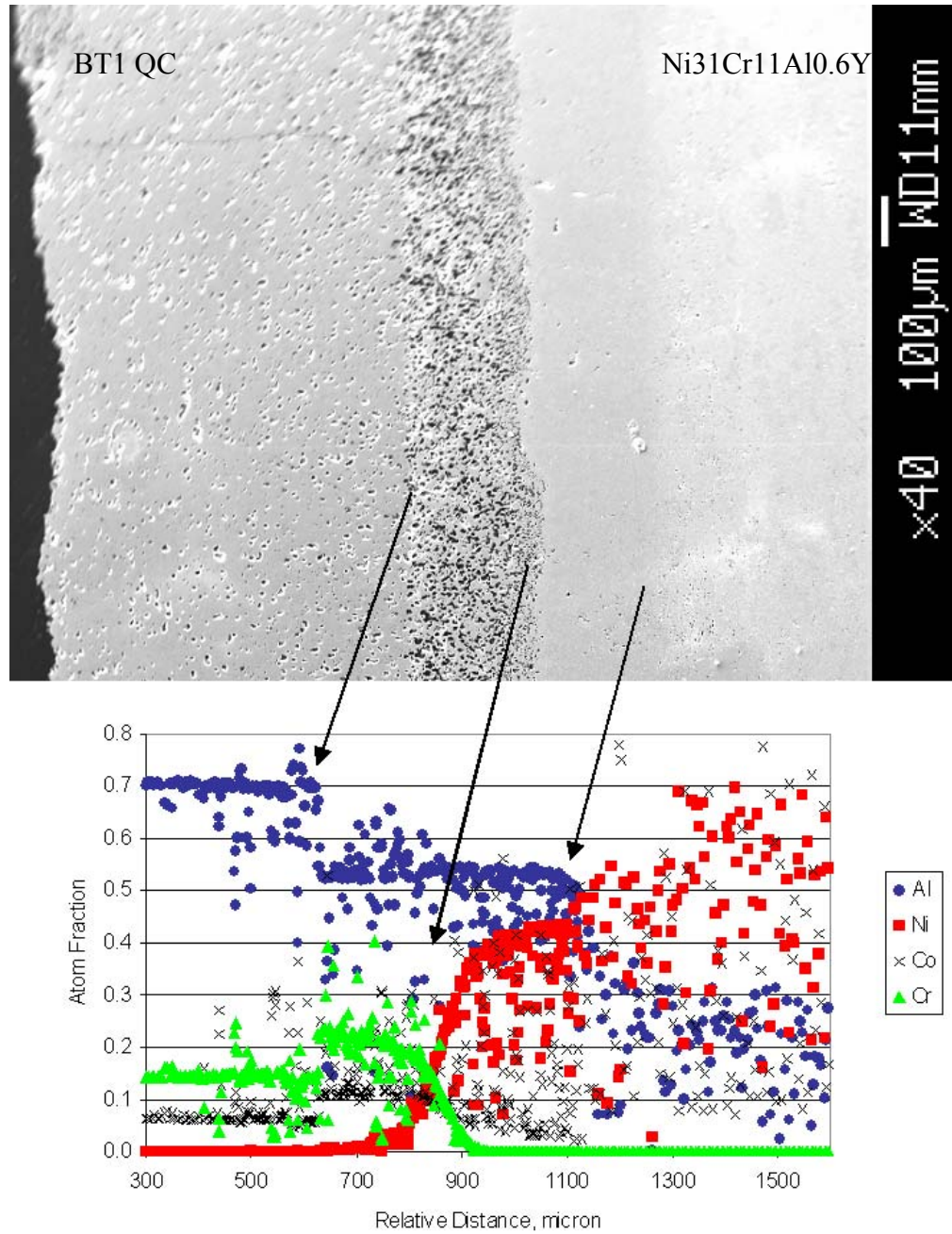


**Figure 5.4-14.** Microstructure of the Ni-31Cr-11Al-0.6Y and BT1 interface after holding for 500 hours at 900C. The scatter in the measured concentration of the nickel and aluminum in the bond coat is not related to the formation of voids as is the case in the BT1 concentration measurements.

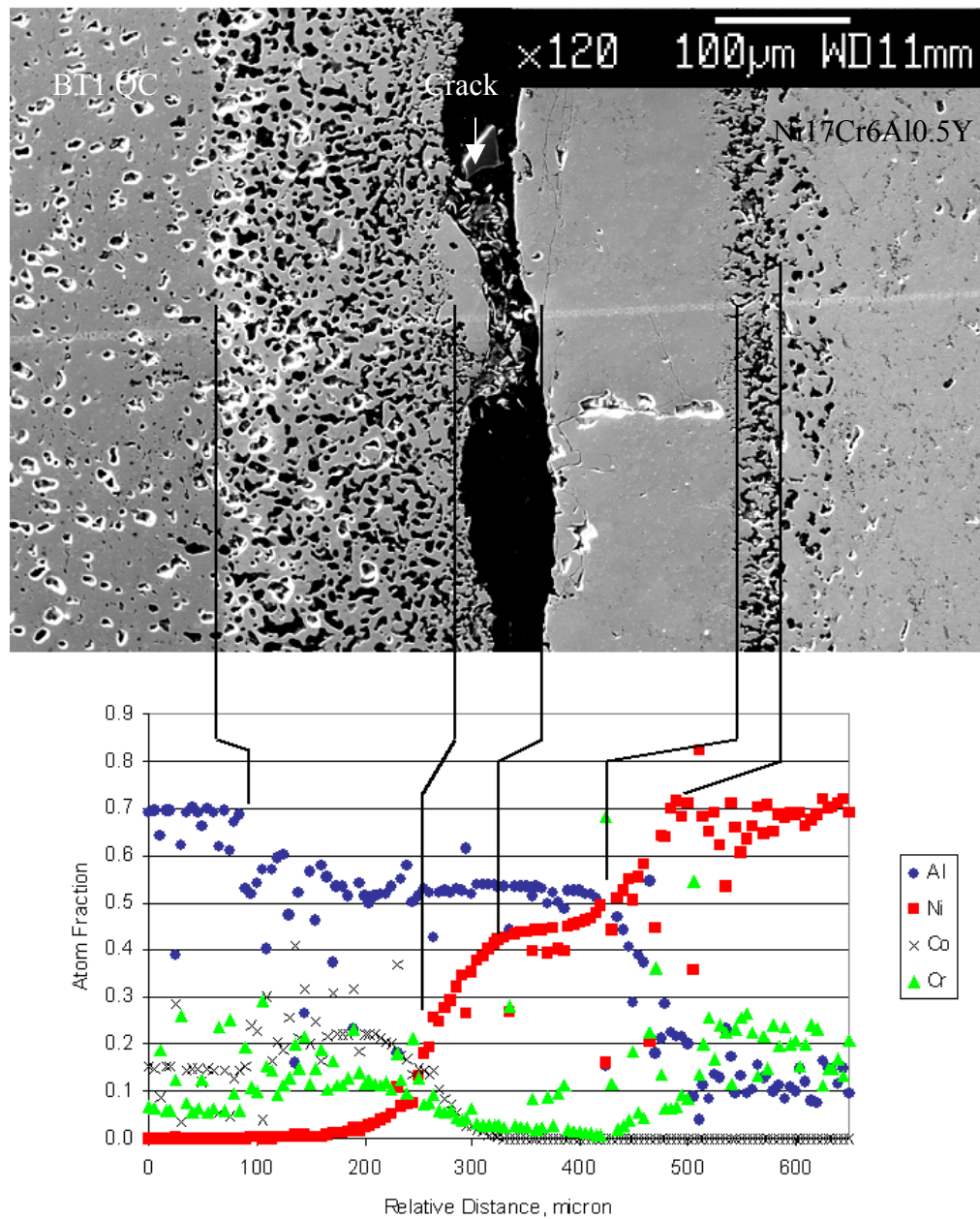


**Figure 5.4-15.** Microprobe concentration profile aligned with SEM image of microstructure of interlayer formed 900°C after 500 hours in BT1 – Ni-17Cr-6Al-0.5Y bond coat showing how the concentration of aluminum and nickel align with the structure observed.

*Table 5.5-1. Interlayer thickness measured from SEM photos at magnifications up to 300X.*

SampleType	Temperature, °C	Time, hr	Total Layer		Layer on Ni/Fe side
			Thickness	Layer on Al side	
SAE 1040	900	25	93.2	30.9	61.0
SAE 1040	900	500	235.1	74.5	163.3
Fe-26Cr-8Al-0.4Y	700	25	4.8		
Fe-26Cr-8Al-0.4Y	700	100	35.2		
Fe-26Cr-8Al-0.4Y	700	500	26.3		
Fe-26Cr-8Al-0.4Y	900	25	110.4	35.7	68.3
Fe-26Cr-8Al-0.4Y	900	100	172.3	55.7	118.8
Fe-26Cr-8Al-0.4Y	900	500			294.1
Ni-17Cr-6Al-0.5Y	700	25	11.3		
Ni-17Cr-6Al-0.5Y	700	100	39.8	16.0	27.4
Ni-17Cr-6Al-0.5Y	900	25	127.6	58.4	69.3
Ni-17Cr-6Al-0.5Y	900	100	209.0	97.7	116.3
Ni-17Cr-6Al-0.5Y	900	500	352.6	177.2	175.4
Ni-31Cr-11Al-0.6Y	500	500	3.3		
Ni-31Cr-11Al-0.6Y	700	25	15.8	6.2	8.9
Ni-31Cr-11Al-0.6Y	700	100	51.7	18.7	27.4
Ni-31Cr-11Al-0.6Y	700	500	87.0	38.6	55.5
Ni-31Cr-11Al-0.6Y	900	25	135.2	55.7	83.5
Ni-31Cr-11Al-0.6Y	900	100	243.7	119.4	120.7
Ni-31Cr-11Al-0.6Y	900	500	520.1	232.9	288.2

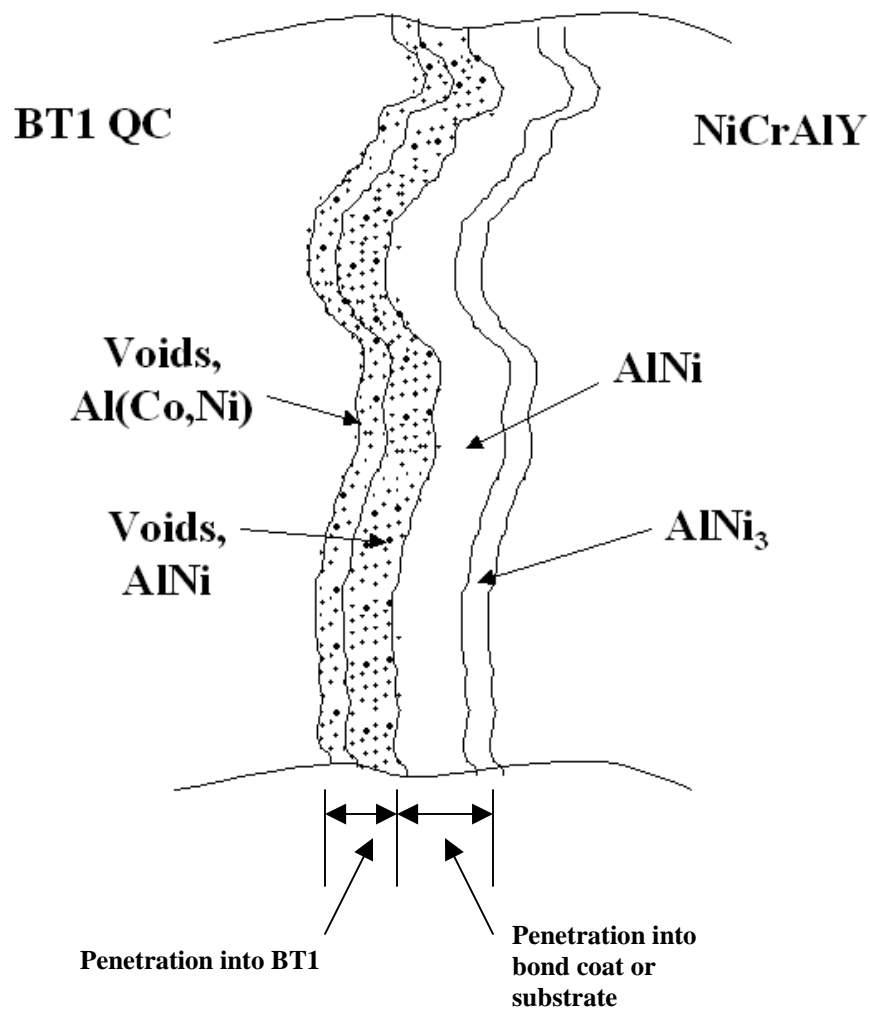


*Figure 5.5-1. Schematic of interlayer phases showing approximate locations for measurement of phase thickness.*

separation was taken to be the edge of the major porosity on the quasicrystal side. The depth of penetration into the bond coat/substrate was taken to be the limit of the high density in the bond coat or the visible change in the iron in the SAE 1040 at 900°C (see Figures 5.4-11). Layer thickness in the iron-based substrates was considerably deeper than in the nickel-based bond coatings. As there was virtually no layer detected at 700°C or lower in the SAE 1040 steel, higher aluminum mobility is indicated austenite phase versus the lower temperature alpha (ferrite) phase. The presence of the initial interlayer in the iron-based bond coating at 700°C and 500 hours, which was not seen in the SAE 1040 substrate, also suggests a higher mobility of the aluminum in the iron-base bond coat verse the SAE 1040. This may be due to either the high chromium content of the bond coating or a restriction of the mobility of

aluminum in the SAE 1040 for some reason. This will be discussed in more detail in Section 6.

The kinetics for the layer growth may be characterized by the relationship

$$x = \sqrt{K * t} \quad (1)$$

where  $x$  is the layer thickness,  $t$  time at temperature and  $K$  a constant for a given temperature [48]. Implicit in this relationship is that the kinetics are diffusion controlled. The lack of data at 500°C temperature and shorter times at higher temperature limits the usefulness of the penetration depths determined from the SEM images in evaluation of this relationship. To provide more information for this analysis, penetration depth of the aluminum was taken from microprobe analysis to better assess the effect of temperature and time on the layer growth.

The measured concentration profiles for aluminum, nickel, chromium, cobalt and iron were aligned with the interlayer reaction zones for the Ni-31Cr-10Al-0.4Y bond coating samples in Figures 5.4-13 and 5.4-14. As can be seen in these figures, the drop in aluminum content from the BT1 QC corresponds to the beginning of the visible interlayer. Likewise, the leveling of the aluminum content to that found in the bond coat corresponds to the edge of the interlayer in the bond coat. The resulting measured interlayer thicknesses are summarized in shown in Table 5.5-2 and compared to those measured by visual means. The interlayer thickness was higher using profiles, but this method of measurement did allow for a wider temperature range to be assessed using Equation 1. However, even using the microprobe data, the interdiffusion thickness at 500°C for the bond coat materials and the SAE 1040 substrate did not appear to show a consistent growth with time relationship. This is probably due to the relatively large increment of the measurement (2 to 4 micron spacing) compared to the interdiffusion zone, thus causing the actual limits of the concentration changes to be missed. The interlayer growth for the SAE 1040 700°C was also too small to show consistent results for the measurement resolution.

The measured interlayer thickness for the bond coat materials at 700°C and 900°C in Table 5.5-2 were fitted to Equation 1 at the various temperatures to determine the  $K$  for these temperatures. The fact that the interlayer would have zero thickness at time zero was also used as a data point. The resulting values for  $K$  and the extrapolated interlayer thickness at 10,000 hours are shown in Table 5.4-3. The predicted 10,000 hour layer thickness indicates the sensitivity of the species mobility to temperature. The lower interlayer thickness at

**Table 5.5-2. Interlayer thickness from microprobe analysis**

		SAE 1040		Fe-26Cr-8Al-0.4Y		Ni-17Cr-6Al-0.5Y		Ni-31Cr-11Al-0.6Y	
Time, hr	Temperature, °C	Total Interlayer thickness, micron							
		Probe	SEM	Probe	SEM	Probe	SEM	Probe	SEM
25	500	3		2	0	6	0	3	0
500	500	4		2		5		6	3.3
25	700	3		19	4.8	19	11.3	17	15.8
100	700	4.1		15	35.2	25	39.8	68	51.7
500	700	4		67	26.3			93	87.0
25	900	223	93.2	242	110.4	145	127.6	145	135.2
100	900			420	172.3	224	209.0	320	243.7
500	900	611	235.1			440	352.6	627	520.1

**Table 5.5-3. Fit of the Interlayer Thickness to Equation 1 and Extrapolation to 10,000 hours**

	Ni-17Cr-6Al-0.5Y	Ni-31Cr-11Al-0.6Y	Fe-26Cr-8Al-0.4Y
Temperature	K ( $\mu\text{m}^2/\text{sec}$ ) and $R^2$ fit of equation		
700°C	K=0.0047 $R^2=0.9766$	K=0.0051 $R^2=0.8416$	K=0.0024 $R^2=0.9878$
900°C	K=0.1091 $R^2=0.9890$	K=0.2210 $R^2=0.9945$	K=0.4995 $R^2=0.9878$
	Extrapolated interlayer thickness at 10,000 hours, $\mu\text{m}$		
700°C	411	428	294
900°C	1,982	2,821	4,240

700°C of 294  $\mu\text{m}$  compared to 4240  $\mu\text{m}$  at 900°C for the FeCrAlY bond coat confirms the sensitivity of the aluminum mobility in the austenite compared to the ferrite structure.

The extrapolated values at 10,000 hours are idealized values based on the assumption that the interface has infinite composition to draw from while in reality the thickness of the BT1 QC and bond coats are finite.

Based on the measured interlayer thickness and predicted thickness at 10,000 hours, the FeCrAlY bond coat material would appear to be best for use as a grading material with the BT1 quasicrystal. In order to better assess the interlayer growth at the lower temperatures of the diesel application, an extrapolation of these data to lower temperatures is desired. As

the rate constant  $K$ , in Equation (1) is directly related to the diffusion coefficients, it should follow an Arrhenius relationship, i.e.,

$$K = K_0 \exp \frac{Q}{RT} \quad (2)$$

The data in Table 5.5-3 were fit to Equation (2) and the resulting plots with fit equations are shown in Figure 5.5-2. It is important to keep in mind that the equations represent a two-point fit for each temperature in interpreting the extrapolated data. Predicted layer thickness for the three bond coat materials at 300°C and 400°C are shown in Table 5.5-4. The FeCrAlY bond coat again shows the smallest interlayer thickness at these temperatures, but the Ni-17Cr-6Al-0.5Y also show low growth. Keeping in mind the limited amount of data fit to the equations and the data being derived from 700°C and 900°C, this extrapolation has a large uncertainty. It does however indicate that the lower temperature interdiffusion at the extended 10,000 hour time will be on the order of the splat dimension of the thermal sprayed coating structure. Conclusions from this analysis would be that use of the BT1 QC above 300°C would need to be limited to non-graded coating architectures.

To have a better estimate of the lower temperature species mobility and to gain a better understanding of the interaction effects of the various species, estimates of the interdiffusion coefficients were made.

*Table 5.5-4. Extrapolated interlayer thickness at 300°C and 400°C*

	Ni-17Cr-6Al-0.5Y	Ni-31Cr-11Al-0.6Y	Fe-26Cr-8Al-0.4Y
Temperature	Extrapolated interlayer thickness at 10,000 hours, $\mu$ based on $K$ derived from fit of $K = K_0 \exp \frac{Q}{RT}$		
300°C	0.6	21	0.01
400°C	7	63	0.3

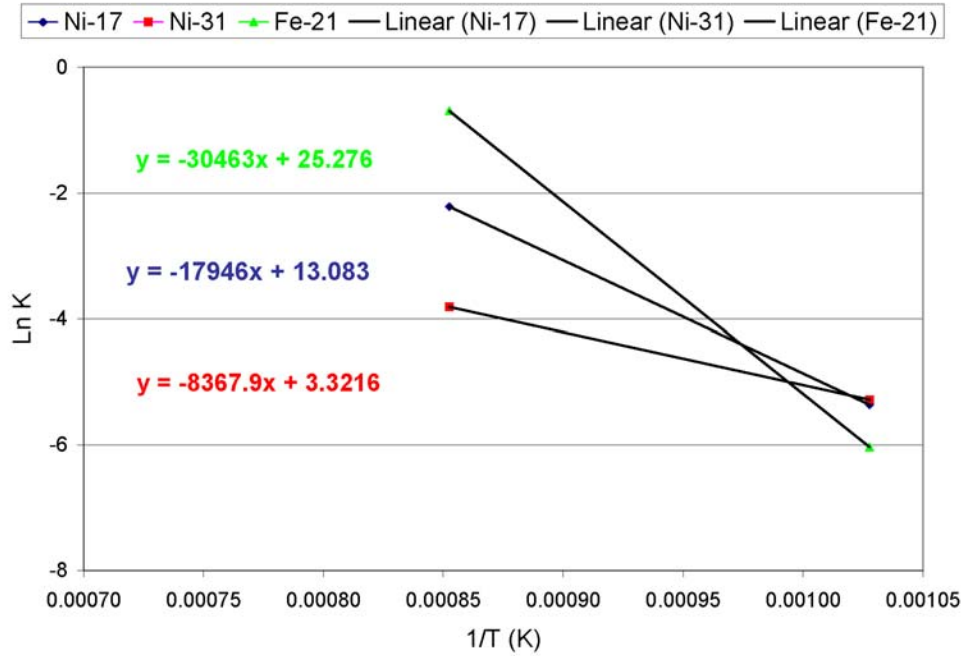


*Figure 5.5-2.  $K$  values for the interlayer thickness plotted as function of temperature to allow for extrapolation to lower temperature interactions.*

## 5.6 Estimation of Average Interdiffusion Coefficients

The diffusion flux for the various couples was calculated using the MultiDiFlux© program of Dayananda (see Section 4.5.) The resulting smoothed concentration profiles and interdiffusion flux profiles for the SAE 1040-BT1 and Fe26Cr8Al0.4Y-BT1 diffusion couples at the three diffusion temperatures are shown in Figures 5.6-1 to 5.6-3. The smoothed concentration profiles for the Ni-17Cr-6Al-0.5Y-BT1 and Ni31Cr11Al0.6Y-BT1 couples are shown in Figures 5.6-4 to 5.6-6. The need to calculate the smooth concentration profiles is evident from the scatter in the microprobe measurements seen at high temperatures for the bond coat materials (see Figures 5.4-11 to 5.4-15).

The average interdiffusion coefficients for the species were calculated from the smooth concentration profiles using the approach of Dayananda (see Section 4.5 for equations reference below). The average effective interdiffusion coefficients,  $D_{i,R}$  and  $D_{i,L}$ , for each species were evaluated on either side of the Matano plane using Eqs. (12) and (13). From Eq. (14), the average interdiffusion coefficient over the entire concentration range,  $D_{i,C}$  was also evaluated. Where possible, the average interdiffusion coefficient over the interlayer

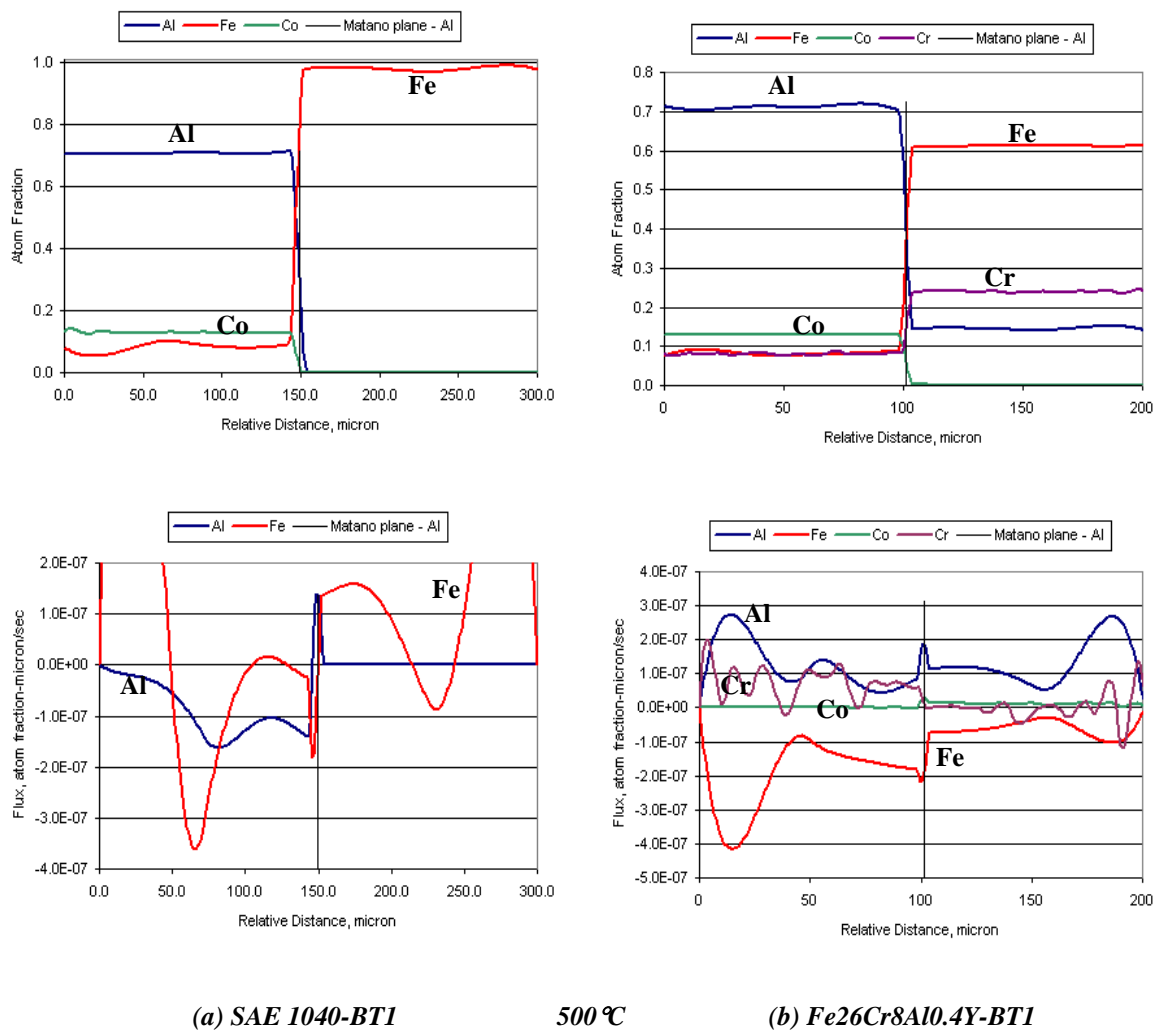


**Figure 5.6-1. Concentration and flux profiles for SAE 1040-BT1 and Fe26Cr8Al0.5Y-BT1 diffusion couples held at 500°C for 500 hours. The fluxes outside of the interlayer area are the result of the small concentration fluctuations.**

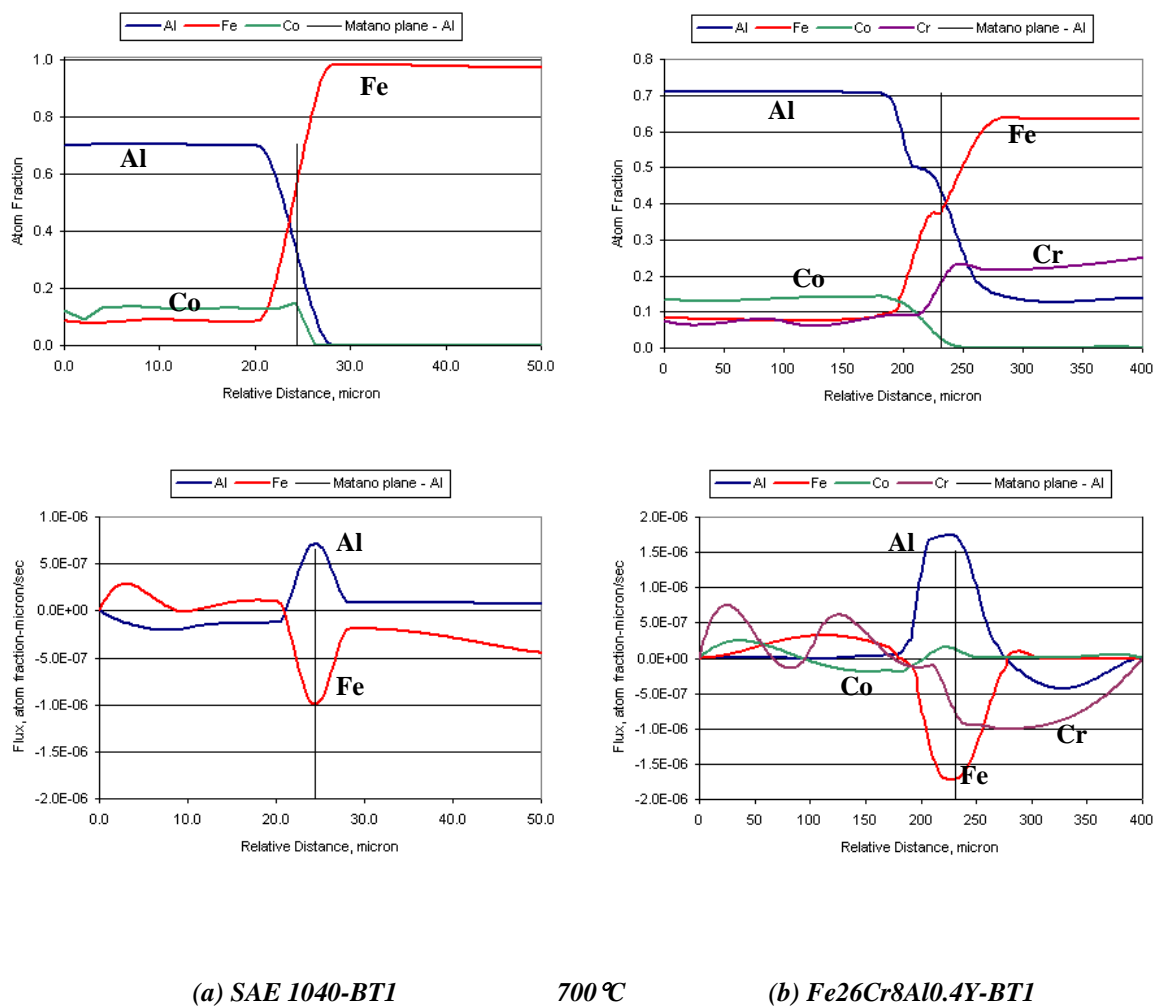


**Figure 5.6-2. Concentration and flux profiles for SAE 1040-BT1 and Fe26Cr8Al0.4Y-BT1 diffusion couples held at 700°C for 500 hours. Note the positive flux for cobalt diffusion in the Fe26Cr8Al0.4Y-BT1 couple in contrast to the for the Ni base bond coats. Note the lower aluminum flux in the SAE 1040-BT1 couple as well as the interlayer phase developing in the Fe26Cr8Al0.4Y-BT1 couple at ~50 atom fraction.**

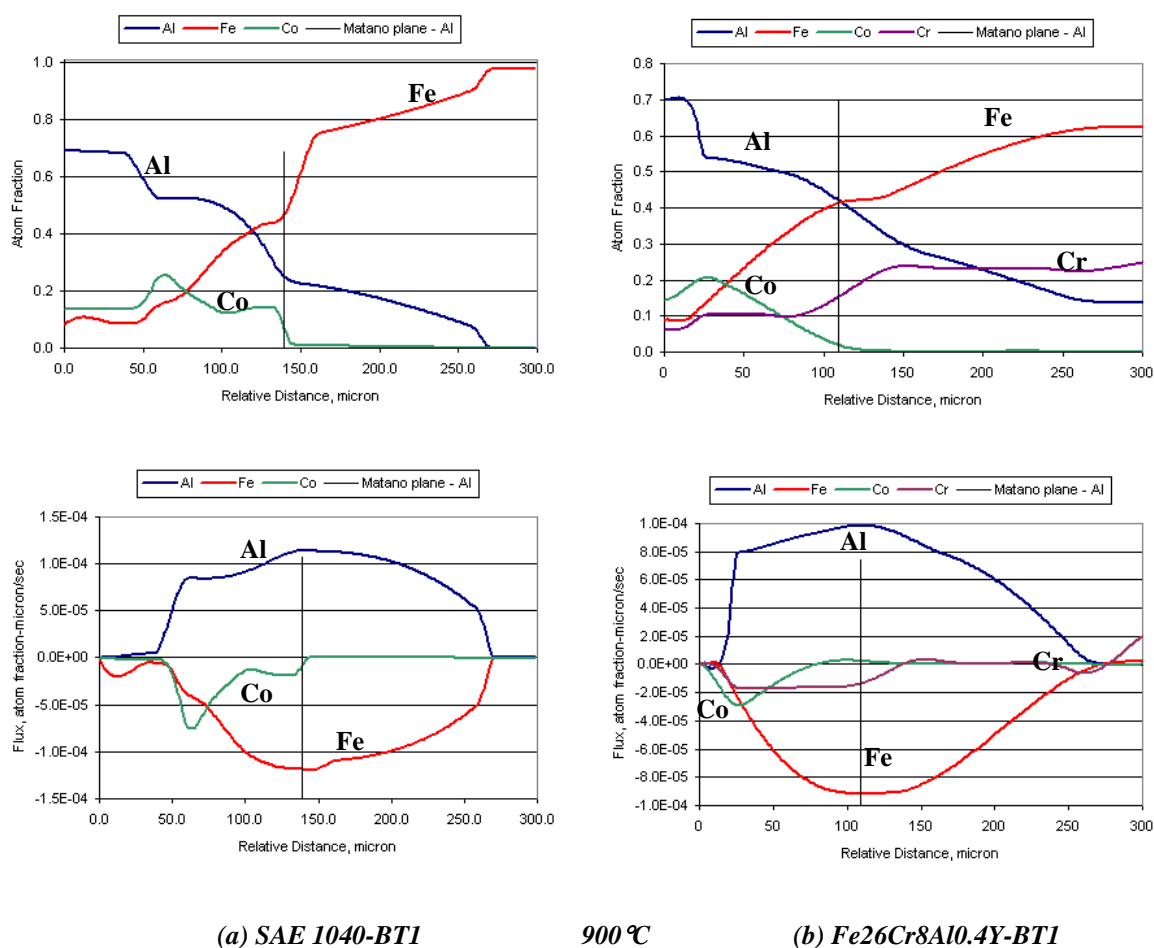


**Figure 5.6-3. Concentration and flux profiles for SAE 1040-BT1 and Fe26Cr8Al0.4Y-BT1 diffusion couples held at 900°C for 25 hours. The high mobility of the aluminum has consumed most of the bond coat thickness. Higher hours at 900C showed completed diffusion of the aluminum through the bond coat . The interlayer composition appears to be close to the FeAl compound and the cobalt flux is negative as in the Ni bond coats with a  $\text{Al}_3\text{Co}_2$  compound being formed.**

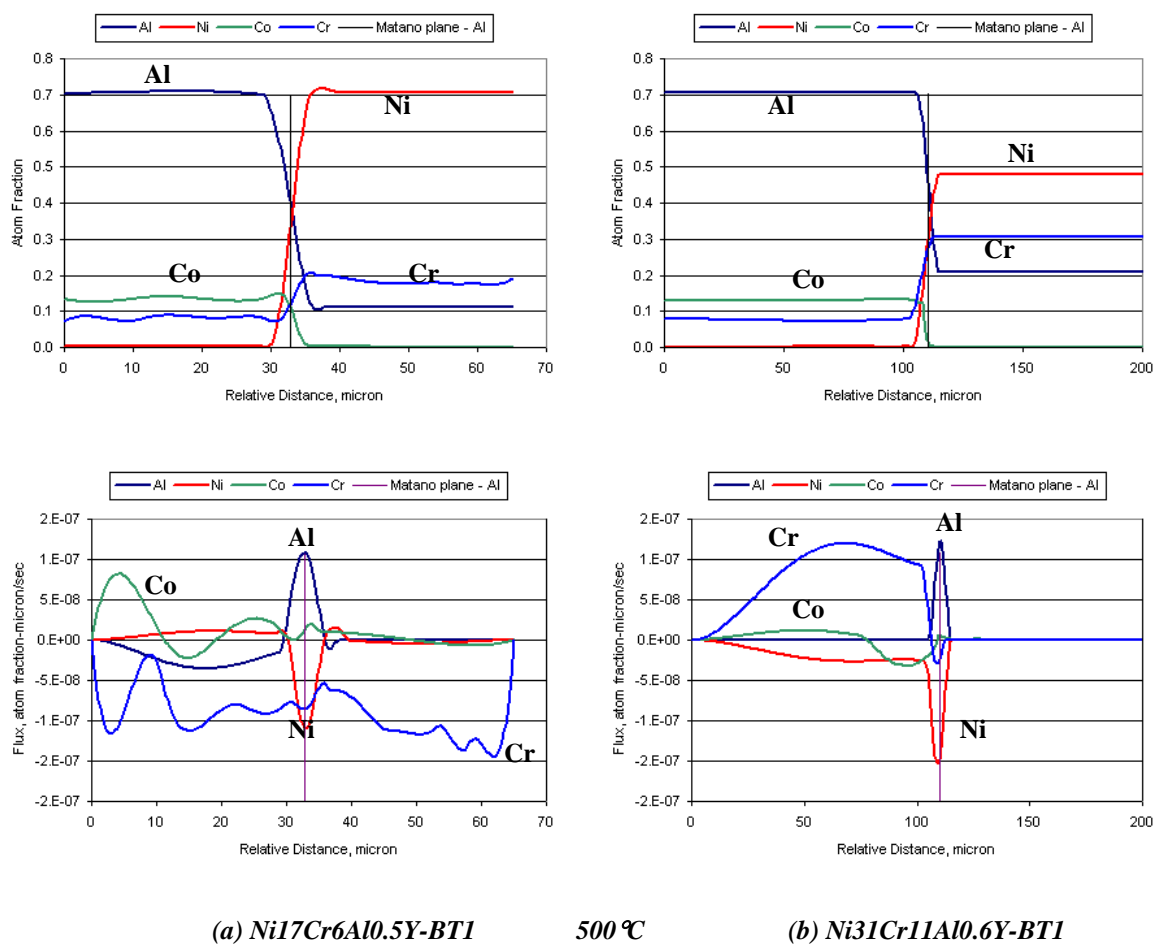
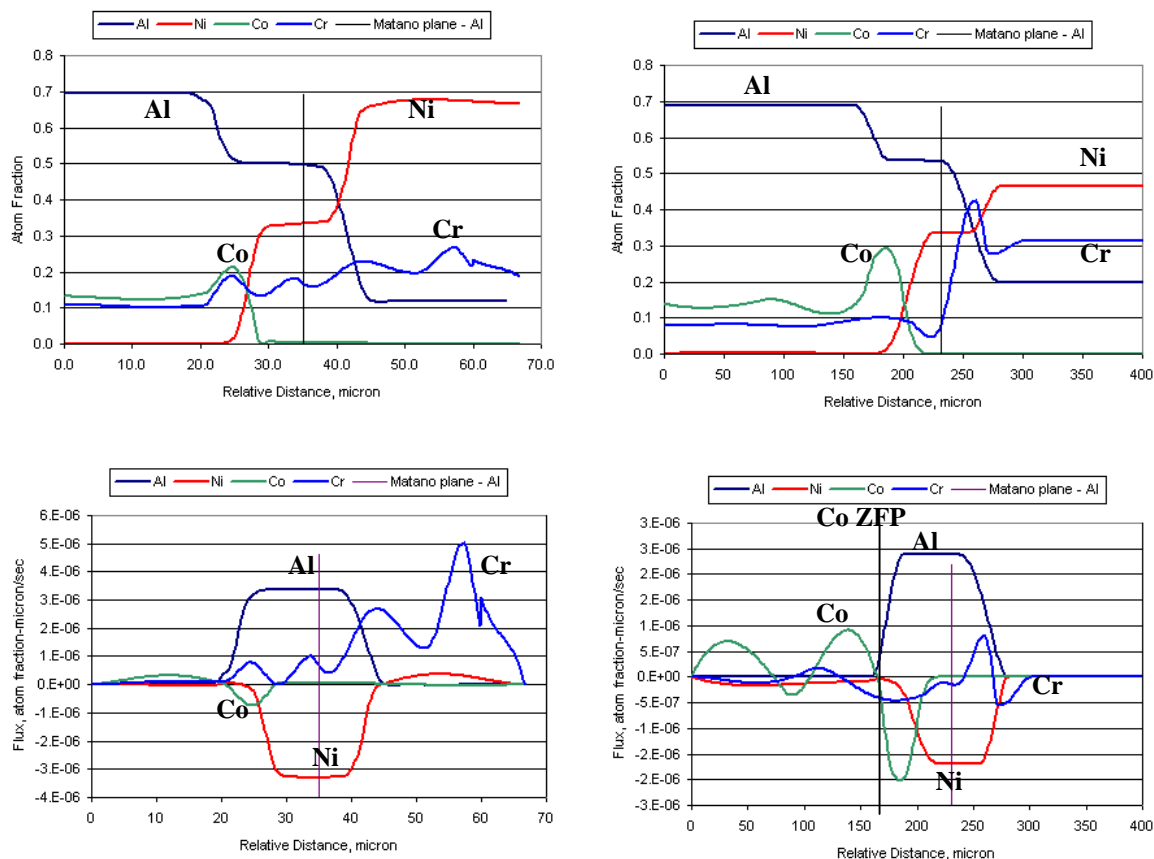


**Figure 5.6-4. Concentration and flux profiles for the Ni17Cr6Al0.5Y-BT1 and Ni31Cr11Al0.6Y-BT1 diffusion couples held at 500°C for 500 hours. The fluxes outside of the interlayer area are the result of the small concentration fluctuations**



(a) Ni17Cr6Al0.5Y-BT1

700 °C

(b) Ni31Cr11Al0.6Y-BT1

**Figure 5.6-5. Concentration and flux profiles for the Ni17Cr6Al0.5Y-BT1 diffusion couple held at 700°C for 100 hours and the Ni31Cr11Al0.6Y-BT1 diffusion couple held at 700°C for 500 hours. Note the negative flux for cobalt, diffusion to the left against the concentration profile. This is caused by the formation of CoAl compound in the interlayer zone next to the BT1 as well as the NiAl<sub>3</sub> next to the bond coat in each couple. Note the development of a zero flux plane for Co in the Ni31Cr11Al0.6Y-BT1 couple.**

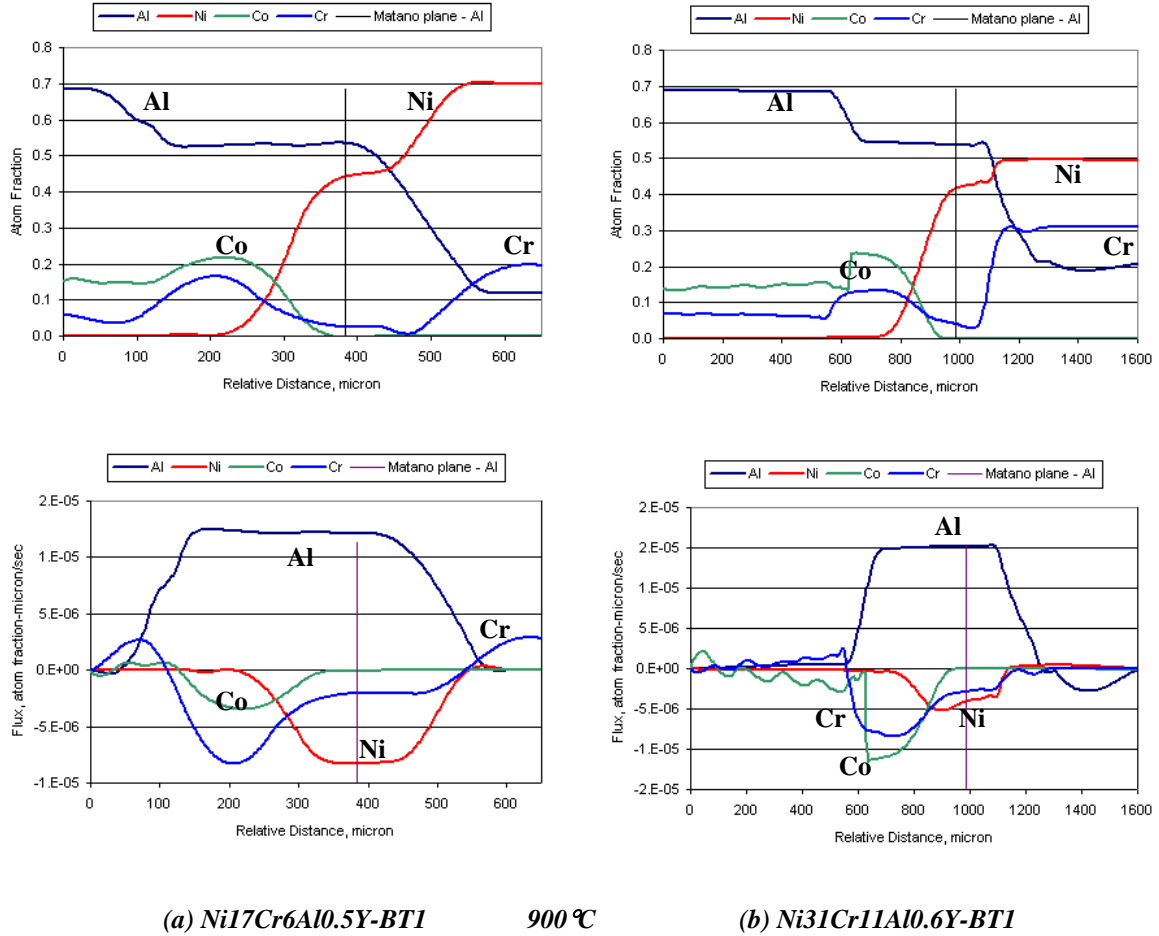


**Figure 5.6-6. Concentration and flux profiles for the Ni17Cr6Al0.5Y-BT1 and Ni31Cr11Al0.6Y-BT diffusion couples held at 900°C for 500 hours. Both cobalt and chromium show a negative flux, diffusion to the left against the concentration profile. The formation of CoAl and chromium-aluminum compounds in the interlayer zone next to the BT1. NiAl is formed next to the bond coat in each couple.**

region,  $\tilde{D}_{\text{NiAl}}$  or  $\tilde{D}_{\text{FeAl}}$ , was also evaluated using Eq. (11). The average interdiffusion coefficients ( $D_{i,R}$ ,  $D_{i,L}$ ,  $D_{i,C}$ ,  $\tilde{D}_{\text{NiAl}}$ ,  $\tilde{D}_{\text{FeAl}}$ ) for aluminum, nickel, cobalt and chromium for the four different diffusion couple types at the three temperatures and times are given in Table 5.6-1.

Not all time and temperature combinations were evaluated due to low interdiffusion at the low time/temperatures and due to spallation of some coatings. Also, the iron based bond coating was only sprayed to a thickness of 0.5 mm as compared to 1 mm for the nickel based bond coats. This resulted in penetration of the aluminum completely through the iron based bond coat for the 100 and 500 hours at 900°C making the analysis for the average diffusion coefficient invalid.

Several general observations can be made from the data in Table 5.6-1. First, the aluminum and nickel diffusion coefficients over the entire concentration range ( $\tilde{D}_C$ ) for the BT1 and nickel- or iron-based bond coat couples are of similar magnitude at each temperature. For the SAE 1040 substrate,  $\tilde{D}_C$  for the aluminum and nickel diffusion at 700°C is an order of magnitude lower than the bond coating couples, but similar at 500°C and 900°C.

The aluminum diffusion coefficient on the left side ( $\tilde{D}_L$ ) of the Matano plane (BT1 side) is higher by 4 to 6 times than on the right side of the Matano plane (substrate) for the nickel-based bond coat diffusion couples. For the iron-based bond coat and SAE 1040 couples, the aluminum diffusion coefficient is 50% higher on the right side ( $\tilde{D}_R$ ) compared to the left of the Matano plane ( $\tilde{D}_L$ ). At 900°C the  $\tilde{D}_L$  for aluminum is 2 to 4 times higher than  $\tilde{D}_R$  for the SAE 1040 substrate. The higher diffusion rate at 900°C for the SAE 1040 substrate and BT1 couple is one cause of the higher void formation in these couples (Figure 5.4-9). The  $\tilde{D}_C$  diffusion coefficients of the cobalt and chrome are negative in the areas of the “up hill” diffusion, indicating the direction of movement is against the concentration gradient.

The diffusion coefficients can be plotted as a function of temperature using the equation:

$$\tilde{D}_i = D_0 \exp \frac{Q}{RT} \quad (22)$$

**Table 5.6-1. Average interdiffusion coefficients for the four types of diffusion couples at the three temperatures and three times.**

Diffusion Couple	Component		500°C	700°C	700°C	700°C	900°C	900°C	900°C
			500 hr	25 hr	100 hr	500 hr	25 hr	100 hr	500 hr
Average Effective Interdiffusion Coefficients (m <sup>2</sup> /s)x10 <sup>17</sup>									
Ni17Cr6Al0.5Y-BT1	Al	$\tilde{D}_L$	0.396	58.1	22.1		2920	3640	2390
		$\tilde{D}_R$	0.202	15.6	5.8		503	616	358
		$\tilde{D}_C$	0.304	10.5	11.4		1210	1450	886
		$\tilde{D}_{NiAl}$		296.0	254.0		49600	44100	11700
	Ni	$\tilde{D}_L$	0.275	21.2	7.2		258	448	158
		$\tilde{D}_R$	0.172	17.1	7.7		716	735	397
		$\tilde{D}_C$	0.222	24.6	7.5		441	566	251
		$\tilde{D}_{NiAl}$		167.0	163.0		4170	2210	1610
	Co	$\tilde{D}_L$	0.345	-11.8	-2.4		-1850		-312
		$\tilde{D}_R$	0.179	9.9	7.5		159		-12
		$\tilde{D}_C$	0.264	-7.2	2.2		-115		-298
		$\tilde{D}_{NiAl}$							
	Cr	$\tilde{D}_L$	0.162	-104.0	-23.5		13		-5340
		$\tilde{D}_R$	0.120	43.5	-12.1		-176		6
		$\tilde{D}_C$	0.139	-20.3	-11.7		-345		944
		$\tilde{D}_{NiAl}$	0.396						
Ni31Cr11Al0.6Y-BT1	Al	$\tilde{D}_L$	0.130	27.2		92	3680	3480	3770
		$\tilde{D}_R$	0.113	0.5		21	775	1360	807
		$\tilde{D}_C$	0.121	24.9		43	1690	2060	1740
		$\tilde{D}_{NiAl}$		80.8		2310	8630	25400	51000
	Ni	$\tilde{D}_L$	0.111	8.8		11	303	318	138
		$\tilde{D}_R$	0.144	18.1		57	863	910	430
		$\tilde{D}_C$	0.127	12.1		25	513	557	265
		$\tilde{D}_{NiAl}$		101.0		1150	8380	7570	1840
	Co	$\tilde{D}_L$	-0.470	-10.2		-41	-644		322
		$\tilde{D}_R$	0.040	2.0		-4	4		377
		$\tilde{D}_C$	-0.389	-5.3		-42	-667		326
		$\tilde{D}_{NiAl}$							-3940

**Table 5.6-1. Average interdiffusion coefficients for the four types of diffusion couples at the three temperatures and three times. (continued)**

Diffusion Couple	Component		500°C	700°C	700°C	700°C	900°C	900°C	900°C
			500 hr	25 hr	100 hr	500 hr	25 hr	100 hr	500 hr
Average Effective Interdiffusion Coefficients (m <sup>2</sup> /s)x10 <sup>17</sup>									
Ni31Cr11Al0.6Y-BT1	Cr	$\tilde{D}_L$	0.050	-3.2		171	3750		-6660
		$\tilde{D}_R$	0.074	-14.3		0	48		74
		$\tilde{D}_C$	0.094	-6.1		2	387		1230
		$\tilde{D}_{NiAl}$				-2	-5510		
Fe26Cr8Al0.6Y-BT1	Al	$\tilde{D}_L$	0.054	16.6	3.7	25	2890		
		$\tilde{D}_R$	0.028	17.2	1.9	11	3320		
		$\tilde{D}_C$	0.041	16.9	2.9	17	3100		
		$\tilde{D}_{FeAl}$		42.3		138	4730		
	Fe	$\tilde{D}_L$	0.033	13.9	4.9	1	1870		
		$\tilde{D}_R$	0.081	18.0	4.1	38	4020		
		$\tilde{D}_C$	0.071	15.7	4.1	29	2710		
		$\tilde{D}_{FeAl}$		39.9		940	13100		
	Co	$\tilde{D}_L$	0.085	10.3	3.4	8	-897		
		$\tilde{D}_R$	0.031	9.5	0.8	5	158		
		$\tilde{D}_C$	0.061	10.0	2.0	6	-681		
		$\tilde{D}_{FeAl}$		11.7					
	Cr	$\tilde{D}_L$	0.134	1.7	3.1	184	3020		
		$\tilde{D}_R$	0.000	0.9	1.2	-137	392		
		$\tilde{D}_C$	0.123	1.4	1.7	40	1460		
		$\tilde{D}_{FeAl}$		4.2			25900		
SAE 1040	Al	$\tilde{D}_L$	0.187		0.6		1820		597
		$\tilde{D}_R$	0.093		0.1		4640		2210
		$\tilde{D}_C$	0.143		0.5		2880		1180
		$\tilde{D}_{FeAl}$					2710		2060
	Fe	$\tilde{D}_L$	0.065		0.6		1680		388
		$\tilde{D}_R$	0.159		0.3		2340		1810
		$\tilde{D}_C$	0.132		0.5		2030		849
		$\tilde{D}_{FeAl}$					1390		2950

**Table 5.6-1. Average interdiffusion coefficients for the four types of diffusion couples at the three temperatures and three times. (continued)**

			500°C	700°C	700°C	700°C	900°C	900°C	900°C
Diffusion Couple	Component		500 hr	25 hr	100 hr	500 hr	25 hr	100 hr	500 hr
Average Effective Interdiffusion Coefficients (m <sup>2</sup> /s)×10 <sup>17</sup>									
SAE 1040	Co	$\tilde{D}_L$	0.028				-2170		-239
		$\tilde{D}_R$	0.277				1780		48
		$\tilde{D}_C$	0.266				-2010		-156
		$\tilde{D}_{FeAl}$					-1010		-1150
	Cr	$\tilde{D}_L$	-1.580				-1680		
		$\tilde{D}_R$	0.202				282		
		$\tilde{D}_C$	0.265				-1280		
		$\tilde{D}_{FeAl}$					-418		

Plots for the average diffusion coefficient for the aluminum and nickel or iron are shown in Figures 5.6-7 and 5.6-8. It can be readily seen that the diffusion coefficients of the nickel- and iron-bond coat couples are similar in magnitude at all temperatures. For the SAE 1040 couple, the diffusion coefficients for aluminum and iron are considerably different than that for the bond coat couples at 700°C. Linear equation fits with correlation  $R^2$  fitting parameters are given in Table 5.6-2.

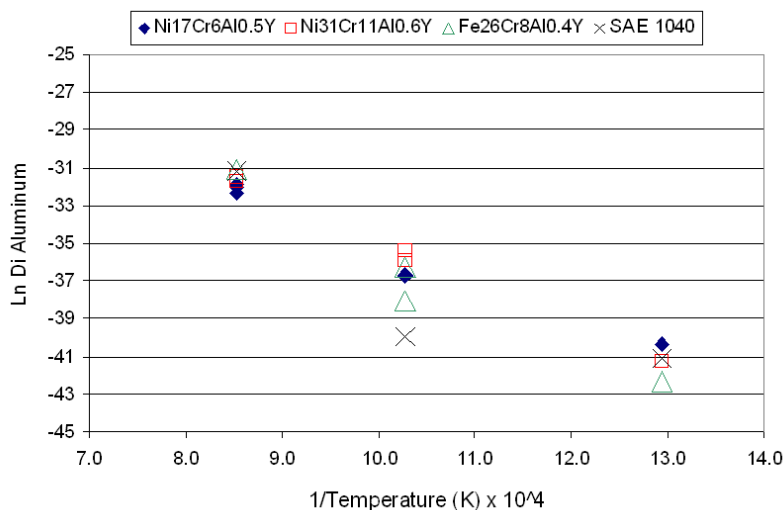


**Figure 5.6-7. The average diffusion coefficient ( $D_{i,c}$ ) for aluminum plotted as a function of temperature using Eq. (22). Note the lower diffusion coefficient for the SAE 1040-BT1 and Fe26Cr8Al0.4Y-BT1 couples at 700°C.**

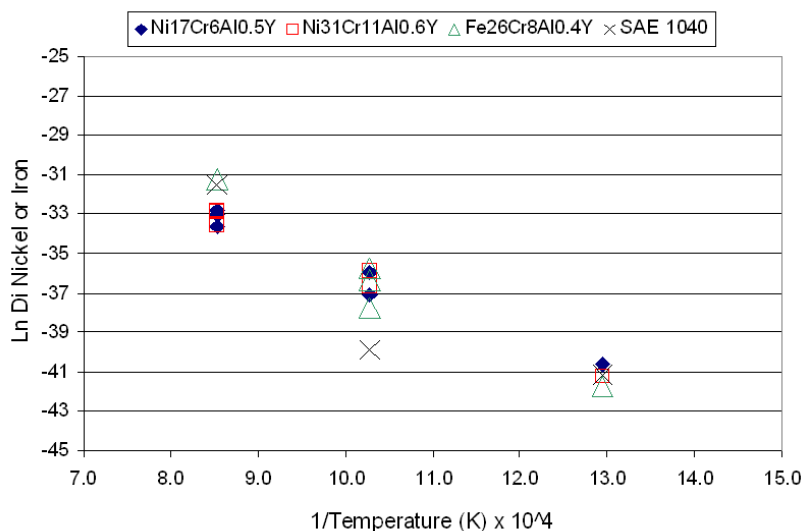


**Figure 5.6-8.** The average diffusion coefficient ( $D_{i,c}$ ) for nickel or iron plotted as a function of temperature using Eq. (22). Note lower diffusion coefficient for the SAE 1040-BT1 and Fe26Cr8Al0.4Y-BT1 couples at 700°C.

**Table 5.6-2.** Linear equation fits to the diffusion data in Figure 5.6-7 and 5.6-9 are shown below. The second equation for the aluminum diffusion coefficient in the SAE 1040 couple represents the fit for the 500°C to 700°C only.

Aluminum		
Ni17Cr	$y = -1.9484x - 15.837$	$R^2 = 0.9568$
Ni31Cr	$y = -2.1921x - 12.999$	$R^2 = 0.9970$
Fe 26Cr	$y = -2.4767x - 10.921$	$R^2 = 0.9371$
SAE 1040	$y = -2.0987x - 15.200$	$R^2 = 0.7394$
SAE 1040*	$y = -0.4311x - 35.512$	$R^2 = 1$
Nickel or Iron		
Ni 17Cr	$y = -1.7207x - 18.594$	$R^2 = 0.9726$
Ni 31Cr	$y = -1.8366x - 17.430$	$R^2 = 0.9883$
Fe 26Cr	$y = -2.3274x - 12.247$	$R^2 = 0.9354$
SAE 1040	$y = -2.0474x - 15.860$	$R^2 = 0.7560$

\*Fit of data at 500°C and 700°C only.

## 5.7 Root-Mean-Squared Penetration Depths

By using the average interdiffusion coefficients over the entire concentration range,  $D_{i,C}$ , the effective or root-mean-squared (r.m.s.) penetration depths,  $x_{i,C}$ , component  $i$  may be calculated using Eq. (21). By using the values of  $D_{i,C}$  calculated from the equations from Table 5.6-1, predicted penetration depths at lower temperatures can be extrapolated. Calculated penetration depths for the aluminum at 500 and 10,000 hours are summarized in Table 5.7-1. Aluminum was chosen for this calculation as it extends throughout the concentration gradient for all species in the couples. The r.m.s. depth does not reflect the full penetration of the speci. The r.m.s. depth calculated for 500 hours compares well with that found from the measurement of interlayer thickness by SEM and microprobe (Table 5.5-2). The 10,000 hour extrapolate thickness represent an idealized case as the analysis depends on infinite dimensions for the BT1 and substrate materials while in the actual coated components there will be finite thickness to the coatings.

**Table 5.7-1. Aluminum penetration depths calculated from predicted  $D_{i,C}$  compared with measured penetration depth at 500 hours measured by SEM photomicrographs.**

Diffusion Couple	Temperature	Predicted $D_{c,Al}$	r.m.s. Penetration Depth at 500 hours, micron	Measured Penetration Depth at 500 hours by SEM	r.m.s. Penetration Depth at 10,000 hours, micron
Ni17Cr6Al0.5Y-BT1	900°C	8.09605E-15	120.7	352.6**	539.9
	700°C	2.66365E-16	21.9		97.9
	600°C	2.68721E-17	7.0		31.1
	550°C	6.92522E-18	3.5		15.8
	500°C	1.49756E-18	1.6	0	7.3
	400°C	3.53862E-20	0.3		1.1
	300°C	2.2623E-22	0.0		0.1
	220°C	9.08232E-25	0.0		0.01
Ni31Cr11Al0.6Y-BT1	900°C	1.73189E-14	176.6	520.1	789.6
	700°C	3.71757E-16	25.9	87.0	115.7
	600°C	2.81505E-17	7.1		31.8
	550°C	6.123E-18	3.3		14.8
	500°C	1.09329E-18	1.4	3.3	6.3
	400°C	1.6171E-20	0.2		0.8
	300°C	5.49541E-23	0.0		0.0
	220°C	1.10641E-25	0.0		0.0

**Table 5.7-1 (continued). Aluminum penetration depths calculated from predicted  $D_{i,C}$  compared with measured penetration depth at 500 hours measured by SEM photomicrographs.**

Fe26Cr8Al0.4Y-BT1	900°C	1.22257E-14	148.3	172.3**	663.4
	700°C	1.59376E-16	16.9	26.3	75.7
	600°C	8.63258E-18	3.9		17.6
	550°C	1.54029E-18	1.7		7.4
	500°C	2.19902E-19	0.6	0	2.8
	400°C	1.88211E-21	0.1		0.3
	300°C	3.05768E-24	0.0		0.0
SAE1040-BT1*	700°C	4.49922E-18	2.8	0	12.7
	600°C	2.70848E-18	2.2		9.9
	500°C	1.42983E-18	1.6	0	7.2
	400°C	6.24306E-19	1.1		4.7
	300°C	2.04124E-19	0.6		2.7

*\* $D_{i,C}$  extrapolated from 700°C and below data fit*

*\*\*Penetration depth at 100 hours*

## 6.0 Discussion

Technical barriers to be addressed for application of the BT1 QC coating as a TBC for diesel engine components are the stability of the mechanical properties of the QC material and the impact of diffusion interactions between the QC coating and bond coating or substrate. Assessment of couplings between the BT1 QC and substrates provided an initial understanding of these issues. Two types of assessment were done. One was of the BT1 QC coating without regard to interface reactions with the bond coat or substrate and the second was of the interface interactions.

Summary of BT1 QC coating property changes - The stability of the BT1 QC coating assessed without regard to interface reactions was done by the following three methods: evaluation of the coating hardness and modulus as measured by instrumented indentation technique; analysis of XRD diffraction patterns for the BT1 QC structure; and tracking of the coating microstructural changes through SEM metallography.

The bulk modulus of 213 to 320 GPa measured via the instrumented indentation (using the Vickers indenter) for some of the thermal-exposed coatings were higher than that for the starting powder, 159 GPa. This suggests there were changes in the BT1 QC constitution during thermal exposure. The dramatic changes in the BT1 QC bulk modulus correlated with changes in the XRD pattern of the coating and the precipitation of phases that occurred with exposure to temperature. At long time at temperature, the bulk modulus of the coating approached that for the starting powder.

The coating modulus (measured using the spherical indenter) of 53 GPa was initially lower than the bulk BT1 QC modulus of 159 GPa due to the effects of coating structure, i.e. microcracks and pores. The coating modulus increased to 70-80 GPa with time at temperature as the microcracks and pores consolidated, but did not increase to the bulk modulus value due to the porosity remaining in the coating.

The changes to the bulk modulus of the coating indicated that the BT1 QC coating structure underwent changes with exposure to high temperature. These changes apparently stabilized after the initial 500 hours of exposure at each temperature studied. The changes to the coating structure as indicated by the spherical modulus, were temperature and time dependent, and relate to the presence of coating microcracks and pore consolidation. This is similar to that which occurs in a zirconia-based TBC system exposed to high temperatures, although the temperature range of exposure is much higher. This was not surprising given that the melting point of the BT1 QC (1120°C) compared to the exposure temperature (500°C).

to 900°C) was similar to that for the zirconia-based systems being tested at the higher temperatures.

Summary of interface phase development - The interface phase formations in the diffusion couples are summarized in the schematic shown in Figure 6-1. All of the couples showed similar behavior with an AlNi- or AlFe-type compound forming at the interface. The thickness of the interlayer phase was larger in the Ni31Cr11Al0.5Y-BT1 couple than the Ni17Cr6Al0.6Y-BT1 couple, which is probably due to the higher aluminum content of the Ni31Cr11Al0.5Y reducing the amount of aluminum being required to diffuse into the bond coat to form the AlNi phase. It is unclear why, but the SAE 1040 couple did not show phase formation at the interface at 700°C, as was found for the Fe26Cr6Al0.4Y couple. This may be due to the contamination of the surface of the SAE 1040 by the grit blasting done prior to spraying. The interface between the bond coatings and the BT1 coating were not grit blasted as this was done only to the SAE 1040 prior to depositing all the coatings. At the 900°C, the higher mobility of the species would overcome this barrier.

## 6.1 Mechanical Properties

No prior studies of the mechanical properties for the BT1 CQ material were found. To provide some understanding of the mechanical behavior of the bulk material and the coatings, instrumented micro-indentation was used. For initial bulk property data, hardness and modulus of the starting annealed powder was measured.

The instrumented indentation method used to assess the BT1 QC coating properties provided three useful pieces of information, i.e., hardness, bulk modulus of the BT1 QC (Vickers modulus), and the coating modulus (spherical modulus) that was dependent on the porosity and microcrack structure of the coating. The hardness of the coating is a composite property of the bulk material hardness and the influences of structural parameters such as microcracks and pores. The two measurements of coating modulus using the Vickers and spherical indenters provided a means to separate the bulk material properties from the coating structure. The Vickers modulus provides an estimation of the bulk properties of the coating material while the modulus measured using the spherical indenter includes to some extent the influence of the coating structure.

This interpretation of the information from the two indenter types has been proposed by others [63] and fits the model proposed by Rejda et al. (see Section 2.5), as summarized in Figure 6.1-1. The smaller area of interaction for the Vickers indenter (see Section 4.6) results in a decrease in  $V_{\text{OPEN}}$  and  $V_{\text{SLIDING}}$  (the volume of cracks and pores that open and slide

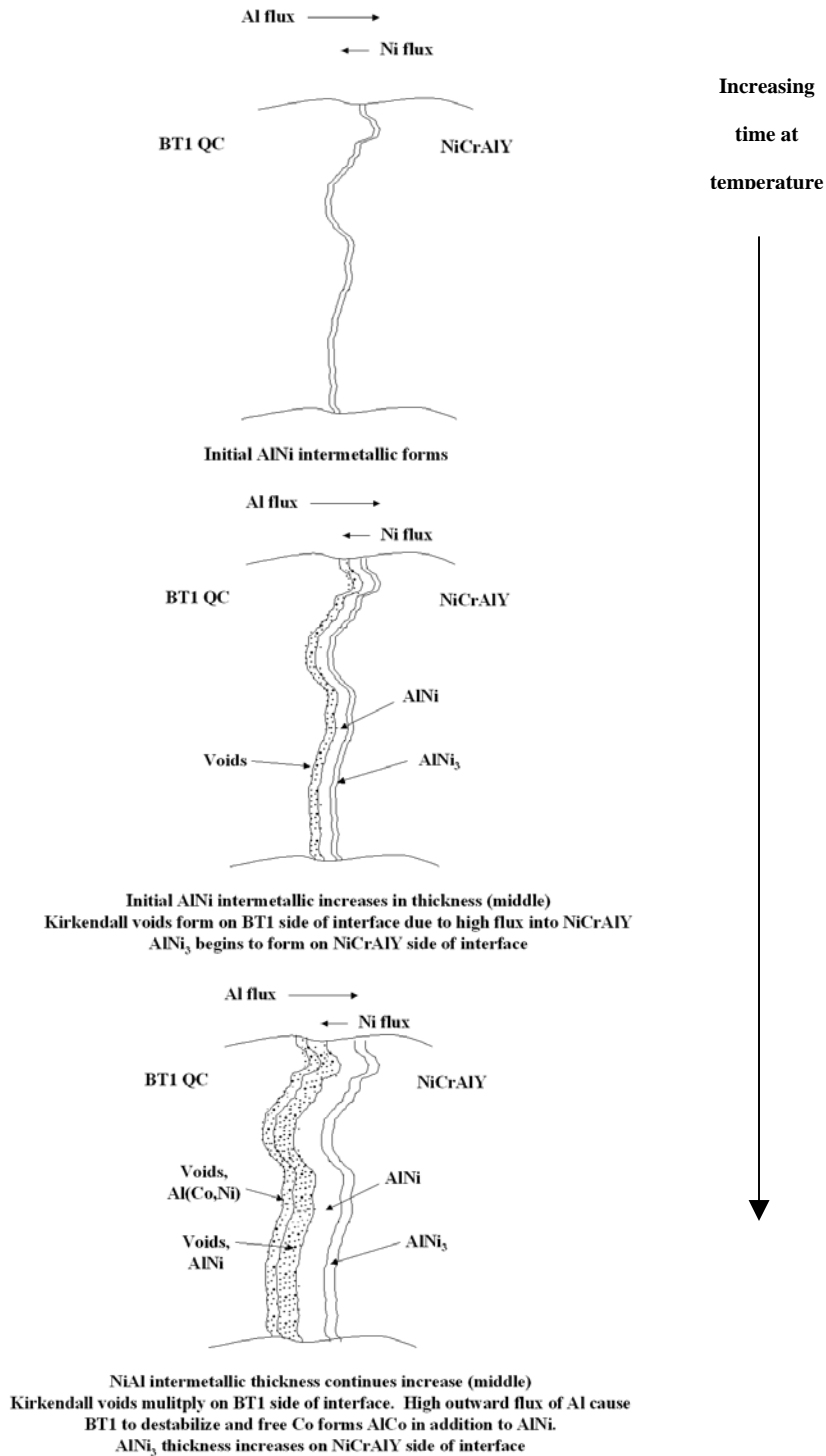


**Figure 6-1.** Schematic of the phase development at the interface between the BT1 QC and NiCrAlY bond coats is shown. The nickel flux into the BT1 QC is less than that of the aluminum flux into the bond coat which results in Kirkendall void formation in the BT1 QC. The iron-based bond coat showed similar behavior at both 700 °C and 900 °C while the SAE 1040 substrate only should interface phases at 900 °C.

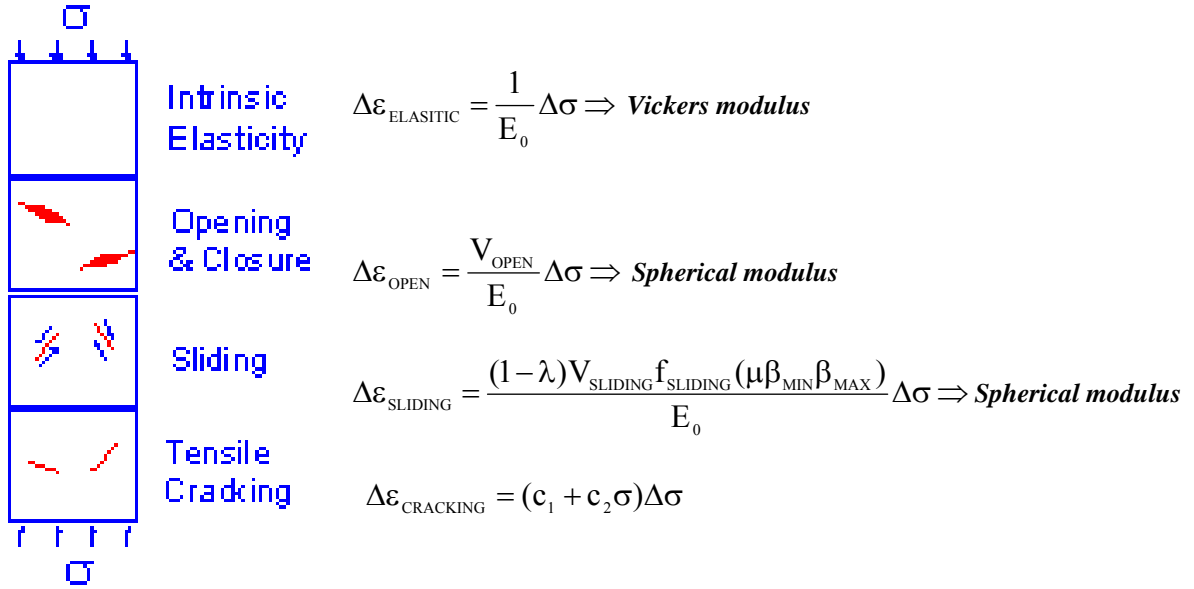


**Figure 6.1-1.** Deformation model proposed by Redja, et. al. [28] showing relationship between model parameters and the Vickers and spherical moduli measured in this study.

under load, see Section 2.5) with a corresponding decrease in  $\Delta \epsilon_{\text{OPEN}}$  and  $\Delta \epsilon_{\text{SLIDING}}$ . The decrease in strain for a given load results in an increase in the modulus. As the indentation load is decreased, the modulus approaches that of the bulk material,  $E_0$ . In this study, the Vickers indenter modulus at a low load such as 1N is assumed to represent the bulk modulus ( $E_0$ ) of the BT1 QC material. The larger area of contact for the spherical indenter increases  $V_{\text{OPEN}}$  and  $V_{\text{SLIDING}}$  resulting in a lower modulus, particularly for coating structures with high amounts of microcracks and pores.

The ten measured values for each BT1 QC sample showed a standard deviation of ~10% (see Figures 5.3-4, 6, and 9). The difference between any two samples that were exposed to the same temperature and time was much higher (25-30%). As each set of samples (SAE 1040-BT1, Fe26Cr8Al0.4Y-BT1, Ni17Cr6Al0.5Y-BT1, Ni31Cr11Al0.6Y-BT1) was sprayed with different setups, small variations in the spray parameters may have occurred. The large variation in the indentation moduli measured indicates that the indentation method is sensitive to minor coating variations caused either by the variation in the coating process during application or due to the interaction between the BT1 QC coating and substrate/bond coats due to the difference in thermal expansion of the iron-base ( $\sim 12 \times 10^{-6}$  mm/mm-°K) and nickel-base substrates ( $\sim 15 \times 10^{-6}$  mm/mm-°K) compared to the BT1 QC

( $\sim 14.5 \times 10^{-6}$  mm/mm-°K). To have a complete understanding of the BT1 QC mechanical behavior, a large number of samples sprayed at different times would be required. For the following analysis, the average of the 1N load measurement for all specimens exposed to the same condition was used and should be taken as trends only. The 5N load measurement show similar trends to the 1N load measurement.

**500°C Samples** – The initial hardness of the BT1 QC was approximately 544 HVN, half of the powder hardness (see Figure 5.3-4). After 100 hours, the hardness increased to 616 HVN and after 500 hours it decreased to 526 HVN.

The Vickers and spherical indentation results provide insight to the changes to the BT1 QC coating that influence this hardness change. The relative changes in the coating structure model parameters are summarized in Table 6.1-1, which shows how the changes in average moduli are related to the model parameters of Redja et al [28].

The Vickers modulus was initially 121 GPa, lower than the powder modulus of 159 GPa. This indicates that the modulus of the BT1 QC bulk material ( $E_0$ ) in the as-sprayed coating is lower than that of the annealed powder. The Vickers modulus then increased to 213 GPa after 100 hours followed by a decrease to 180 GPa after 500 hours. These changes

**Table 6.1-1. The relationship of the Vickers and spherical moduli to changes in the model parameters  $E_0$ ,  $V_{OPEN}$ , and  $V_{SLIDING}$ . The modulus shown is the average of all samples at each temperature.  $E_0$  affects the Vickers modulus while both  $V_{OPEN}$ , and  $V_{SLIDING}$  affect the spherical modulus.**

1N load values	25 hour	100 hour	500 hour
500°C	↓ $E_0$ , $V_{OPEN}$ , $V_{SLIDING}$	↑ $E_0$ , $V_{OPEN}$ , ↓ $V_{SLIDING}$	$E_0$ , $V_{OPEN}$ , ↓ $V_{SLIDING}$
Vickers E, GPa	121	213	180
Spherical E, GPa	53	74	71
Hardness, HVN	544	616	526
700°C	↑↑ $E_0$ , $V_{OPEN}$ , ↓ $V_{SLIDING}$	$E_0$ , $V_{OPEN}$ , ↓ $V_{SLIDING}$	$E_0$ , $V_{OPEN}$ , ↓ $V_{SLIDING}$
Vickers E, GPa	218	153	143
Spherical E, GPa	82	88	73
Hardness, HVN	480	572	532
900°C	↑↑ $E_0$ , ↓ $V_{OPEN}$ , ↓ $V_{SLIDING}$	↑ $E_0$ , ↓ $V_{OPEN}$ , ↓↓ $V_{SLIDING}$	↑ $E_0$ , ↓ $V_{OPEN}$ , ↓↓ $V_{SLIDING}$
Vickers E, GPa	320	192	193
Spherical E, GPa	70	69	63
Hardness, HVN	690	720	682

**$E_0=159$  GPa, HVN=1063 (powder properties)**

in the BT1 QC bulk modulus with time are probably the result of the crystal structure changes that are evident from the XRD diffraction patterns shown in Figure 5.3-3, as well as due to the precipitation of a phase as seen in the coating microstructures shown in Figure 5.3-2d. The EDS analysis of the phase in Figure 5.3-2f of 56-57 at% Al and 29-32 at% Cr was close to that for the  $\text{Al}_9\text{Cr}_4$  phase, which was reported by Sánchez et al. [4]. As the accuracy of the EDS is not high, these precipitates could also be  $\text{Al}_{86}\text{Cr}_{14}$  or  $\text{Al}_{80}\text{Cr}_{20}$ , as reported by Reyes-Gasga et al. [66,67]. These phases are the quasicrystalline part of the approximant and would probably have a high modulus. The changes in the volume percent of these precipitates detected via the XRD patterns and in the SEM micrographs tracked with the changes in Vickers modulus.

The strengthening affect conferred by the precipitate phase is higher just after initial formation and reduced as the phase grew. The precipitation probably occurred at ~100 hours, where the maximum stiffening is detected and the large phase seen at the 500 hours has “over ripened” and lost much of the strengthening affect.

The spherical modulus started at 53 GPa at 25 hours and increased to 74 GPa after 100 hours and remained at 71 GPa after 500 hours. This indicates changes in the coating structure that reduce the volume of cracks that are able to slide,  $V_{\text{SLIDING}}$ . The coating microstructure shown in Figure 5.3-2 shows some indications of microcrack consolidation with time.

700°C Samples – The 480 HVN hardness at 25 hours was lower than that at 500°C. It increased to 572 HVN at 100 hours and then decreased to 532 HVN.

The Vickers modulus showed a large increase to 218 GPa at 25 hours, which is much higher than that of the annealed powder. At 100 hours, the Vickers modulus decreased to 153 HVN and showed only a small decrease to 143 HVN at 500 hours. The changes in the Vickers modulus again tracked with the changes in the BT1 QC crystal structure, as indicated by the changes in the XRD diffraction pattern shown in Figure 5.3-3 as well as the phase precipitation, as shown in Figure 5.3-5d. The initial precipitation of this phase occurred earlier at this temperature resulting in a higher stiffness at 25 hours, which then decreased with the growth of the precipitates, observed within 500-hour microstructure.

The spherical modulus at 25 hours was 82 GPa, slightly higher than that at 500°C/500 hours, and remained relatively constant up to 500 hours. The microcrack density was lower and the porosity had started to consolidate at the 700°C exposure temperature, as shown in Figure 5.3-5. The resulting main effect would be a decrease in  $V_{\text{SLIDING}}$  and a smaller decrease in  $V_{\text{OPEN}}$ , the number of open cracks which can close under load. The decrease in

the open crack volume was probably offset by the pores that are generated by the microcrack consolidation, as some pores would contribute to  $V_{\text{OPEN}}$ .

900°C Samples – The Vickers hardness was high at all times at this temperature, ranging from 690 HVN at 25 hours to 720 HVN at 100 hours and 682 HVN at 500 hours. This range in hardness is not significant when compared to the variation in the measurement (+/- 40 to 60 HVN).

The Vickers modulus was 320 GPa, double that of the annealed powder. It decreased to 192 GPa at 100 hours and remained at this level through to 500 hours. The changes in the constitution and, hence, local chemistry of the BT1 QC, as discussed previously would contribute to the higher Vickers modulus at 25 hours. Both the changes in the XRD pattern and phase precipitation occur at this temperature. There may be additional microstructural changes not seen at the lower temperature that contributed to the significantly higher modulus at 25 hours. As the annealed powder was treated for 1 hour at 900°C, the maximum strengthening was indicated to occur between 1 and 25 hours for this temperature.

The spherical modulus was 70 GPa at 25 hours and remained at this level at 100 and 500 hours. As can be seen in Figure 5.3-7, the microstructure at 25 hours showed evidence of both microcrack consolidation and pore growth, which reduced both  $V_{\text{OPEN}}$  and  $V_{\text{SLIDING}}$ . As the microstructure evolved with time, the relative volume of the pores and sliding cracks remained relatively constant, resulting in little change to the spherical modulus. Thus, most of the significant changes to the coating structure due to microcrack and pore consolidation occurred in the first 25 hours.

As can be seen from this analysis, the instrumented indentation technique provided useful insight into the changes to the coating's mechanical properties. Moreover, the method appears to be sensitive to phase and microstructural changes that are not readily evident in the microstructure, such as phase precipitation. This initial study has provided some understanding of the BT1 QC coatings mechanical property stability with time at temperature, but more detailed property evaluation will be required to fully understand the impact of the coating changes on durability.

## 6.2 Interface Diffusion Interactions

The use of a metallic bond coat not only provides for oxidation protection to the substrate material, but it also should serve to increase the BT1 QC coating adherence by providing a strain compliance between the substrate and QC coating. Differences in thermal expansion between the iron-based substrates used for diesel engine components and the

aluminum-based BT1 QC are also reduced by the use of a nickel-based bond coat that has a thermal expansion coefficient near that of the BT1 QC. The temperature at the bond coat and top coat (BT1 QC) interface for advanced TBC designs in the diesel engine is expected to be in the range of 400°C to 600°C, therefore an understanding of the diffusion interactions between the bond coat and BT1 QC is required.

The diffusion interaction will also impact the durability of graded coating designs that use mixtures of a metallic material (such as the bond coat) to provide strengthening and toughening to the coating, such as that shown in Figure 1-1. Work by Schurack et al. [37] has shown that a combination of QC materials within a ductile metallic skeleton can increase the room-temperature ductility of the composite material by a factor of six. TBCs sprayed with mixtures of metallic bond coat and ceramic have also been demonstrated to have significant increases in strength over the monolithic TBCs [24]. The use of a graded coating design could provide the desired ductility and strength in the QC coating layers. However, this will be limited by the stability of the QC material at high temperatures when in contact with the combined metallic material. The surface temperature of a highly insulating TBC design can be over 800°C at maximum operating conditions. The rapid reaction seen in the BT1 diffusion couples in this study at temperatures above 700°C showed that any graded layer of BT1 QC with the bond-coat compositions studied could not be exposed in this temperature range, i.e., the top layer of the TBC could not contain the metallic material.

A major issue found in prior QC TBC studies was the stability of the coating with respect to diffusion of aluminum from the quasicrystal into the nickel substrate [5, 47]. The initial work by Sanchez et al. [5] using the BT1 QC as a TBC showed that additions of ceramic oxides to metallic bond coatings provided benefit in preventing diffusion of the QC components to the substrate. Although a limited study was done to show the effect of high-temperature exposure on the resulting diffusion between the QC coating and bond coatings, no quantitative analysis of the diffusion process was undertaken.

Standard MCrAlY bond coatings have been extensively studied for the effect of aluminum additions on oxidation. These coatings contain a sufficient aluminum content to form a protective alumina layer in service. Higher aluminum contents (up to 11 wt%) in the MCrAlY bond coating may aid in slowing the extent of the interdiffusion, similar to what was done by Sanchez et al. through the addition of yttria to the bond coating. As the diffusion couples were sealed in quartz containers under vacuum, any effect of that might come from aluminum oxidation in the bond coat was not a factor in this study.

For this investigation, two NiCrAlY and one FeCrAlY bond coatings (see Table 4.1-1 in Section 4.1) were used, as they have been extensively investigated in prior studies and

have been shown to provide the oxidation life required in both cyclic and isothermal testing [9, 40]. The aluminum and chromium contents in these alloys vary and provide an opportunity to assess the influence of these elements on the diffusion interaction between the quasicrystal and bond coating layers. Samples were also tested that were sprayed directly on the SAE 1040 substrate without a bond coat.

At both 700°C and 900°C the bond coat-containing systems developed a phase at the interface between the BT1 QC and the bond coat. The SAE 1040 substrate only developed a phase at the interface with the BT1 QC at 900°C. Based on the binary phase diagrams for nickel-, cobalt-, and iron-aluminum shown in Figures 6.2-1 to 6.2-3, the initial phase at the interface is expected to be an aluminide of either nickel, cobalt or iron.

The interdiffusion fluxes for the various couples are summarized in Table 6.2-1. These results will be discussed in more detail later.

**Table 6.2-1. Interdiffusion flux nickel, iron and aluminum for the couples are shown for selected temperatures and times. A negative flux represents movement toward the BT1 and a positive flux is toward the bond coat or substrate.**

Diffusion Couple	Temperature- Time, hr	Nickel or Iron flux, at%- $\mu\text{m}/\text{sec}$	Aluminum flux, at%- $\mu\text{m}/\text{sec}$
Ni17Cr6Al0.5Y-BT1	700°C, 25 hr	$-1.2 \times 10^{-5}$	$1.1 \times 10^{-5}$
	700°C, 100 hr	$-3.3 \times 10^{-6}$	$3.4 \times 10^{-6}$
	900°C, 25 hr	$-5.0 \times 10^{-5}$	$6.8 \times 10^{-5}$
Ni31Cr11Al0.6Y-BT1	700°C, 25 hr	$-5.6 \times 10^{-6}$	$1.9 \times 10^{-5}$
	700°C, 500 hr	$-1.7 \times 10^{-6}$	$2.4 \times 10^{-6}$
	900°C, 25 hr	$-3.0 \times 10^{-5}$	$7.0 \times 10^{-5}$
Fe26Cr8Al0.4Y-BT1	700°C, 25 hr	$-7.7 \times 10^{-6}$	$8.0 \times 10^{-6}$
	700°C, 500 hr	$-1.7 \times 10^{-6}$	$1.8 \times 10^{-6}$
	900°C, 25 hr	$-9.2 \times 10^{-5}$	$9.8 \times 10^{-5}$
SAE 1040	700°C, 100 hr	$-9.9 \times 10^{-7}$	$7.2 \times 10^{-7}$
	900°C, 25 hr	$-1.2 \times 10^{-4}$	$1.1 \times 10^{-4}$

Interface phase development in 700°C diffusion couples - For the nickel-based bond coats, the phase at the interface at 25 hours contained ~33 atom% nickel with aluminum ranging from 30 atom% to 55 atom%, as shown Figure 6.2-4. This compositional range is consistent with that for AlNi when converted to at% and normalized to just aluminum and nickel as the constituents. The voids in the BT1 QC indicate a high flux of the aluminum

### Al-Ni (Aluminum - Nickel)

P. Nash, M.F. Singleton, and J.L. Murray, 1991

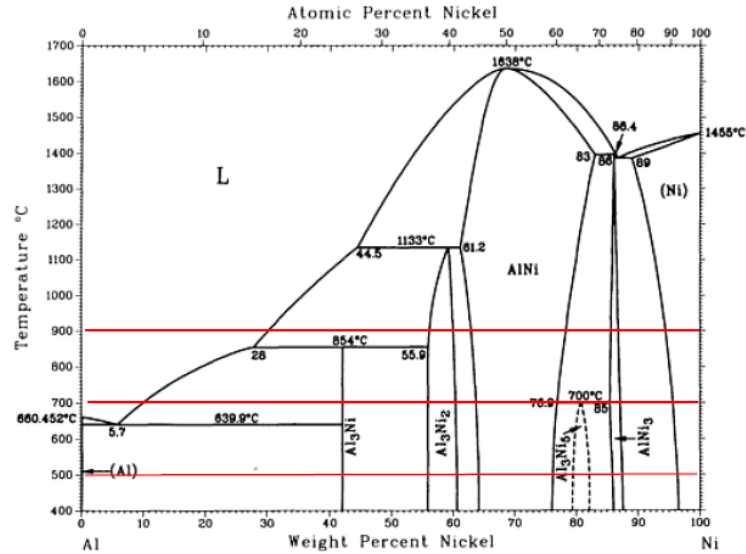


Figure 6.2-1. Phase diagram for aluminum and nickel with the three exposure temperatures indicated by the horizontal lines. [55]

### Al-Co (Aluminum - Cobalt)

A.J. McAlister, 1989

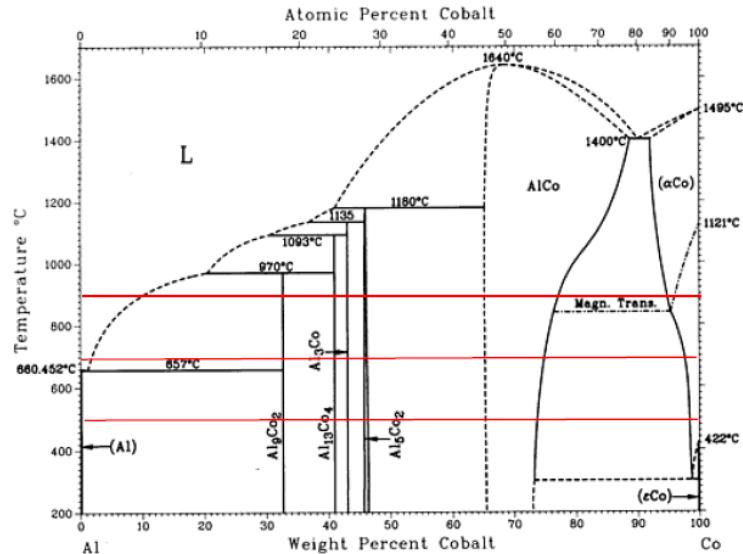
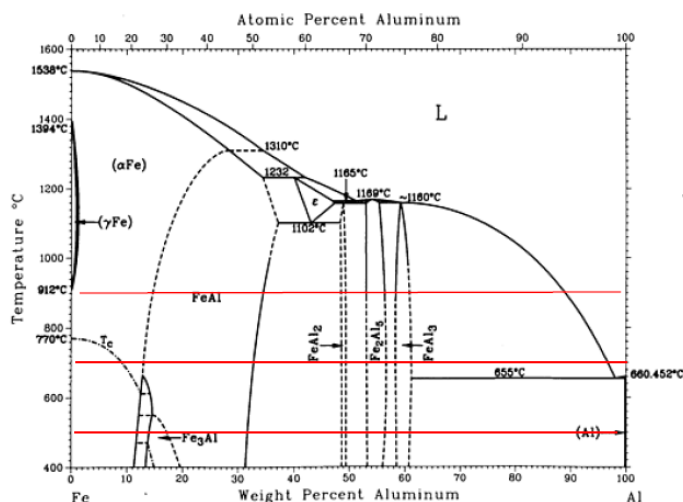


Figure 6.2-2. Phase diagram for aluminum and cobalt with the three exposure temperatures indicated by the horizontal lines. [55]

**Al-Fe (Aluminum - Iron)**

U.R. Kattner and B.P. Burton, 1992



**Figure 6.2-3. Phase diagram for aluminum and iron with the three exposure temperatures indicated by the horizontal lines. [55]**

into the interlayer. For the Ni31Cr11Al0.6Y-BT1 couple the aluminum flux of  $2.4 \times 10^{-6}$  at%· $\mu\text{m}/\text{sec}$  is approximately 40% higher than the nickel flux at  $-1.7 \times 10^{-6}$ . Thus, a flux imbalance existed for the formation of Kirkendall voids. The flux imbalance between aluminum and nickel or iron was not as high in the other couples, but that may be due to the accuracy of the estimated fluxes. There is also a density change from the BT1 QC to the intermetallic compounds at the interface that would promote the void formation. The void formation in the couples are most likely primarily Kirkendall voids.

The relative cobalt content in the BT1 QC increases slightly due to the decrease in aluminum. In addition, the presence of a zero flux plane for the cobalt is clearly present in the Ni31Cr11Al0.6Y-BT1 couple at 500 hour (see Figure 5.6-5). Zero flux planes of this type are common in multicomponent diffusion systems. The diffusion of the Co against its compositional gradient is also a result of the multicomponent system and has been reported by others [49, 50]. This behavior in the diffusion of the components illustrated the complex chemical interactions in this system, which affect non-linear changes in the local chemical potentials.

The lighter phase seen around the voids could be AlCo, as this would be consistent from the aluminum-cobalt phase diagram. The composition of the lighter phase to the right of the AlNi fits that of AlNi<sub>3</sub>.

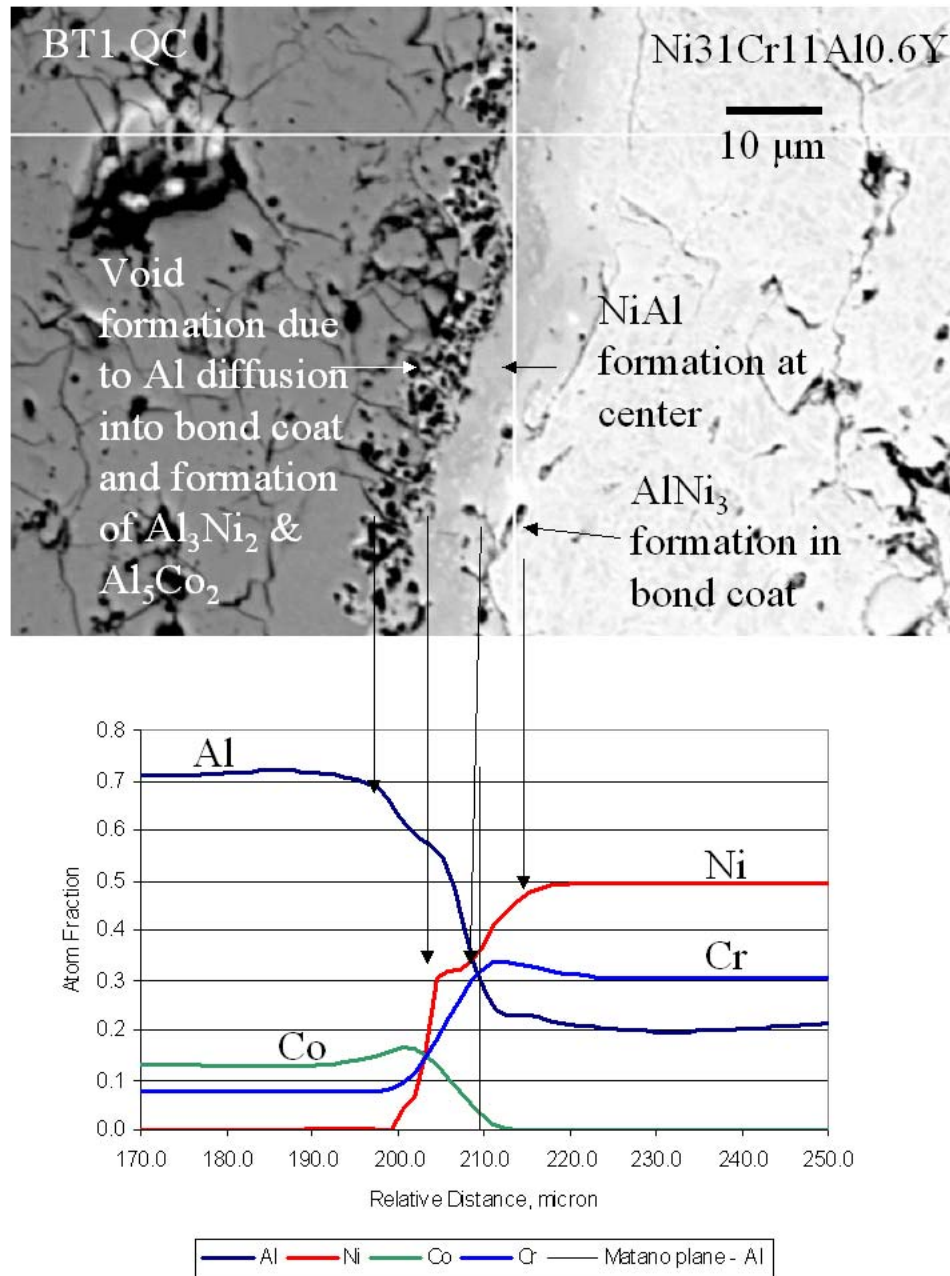


**Figure 6.2-4.** Microstructure of Ni31Cr11Al0.6Y-BT1 diffusion couple after initial 25 hours at 700 °C showing the development of the phases at the interface. The NiAl intermetallic phase initially forms at the interface with  $\text{Al}_3\text{Ni}_2$  and  $\text{Al}_5\text{Co}_2$  forming to the left of the interface as the Al diffuses into the bond coat and a  $\text{NiAl}_3$  forming to the right.

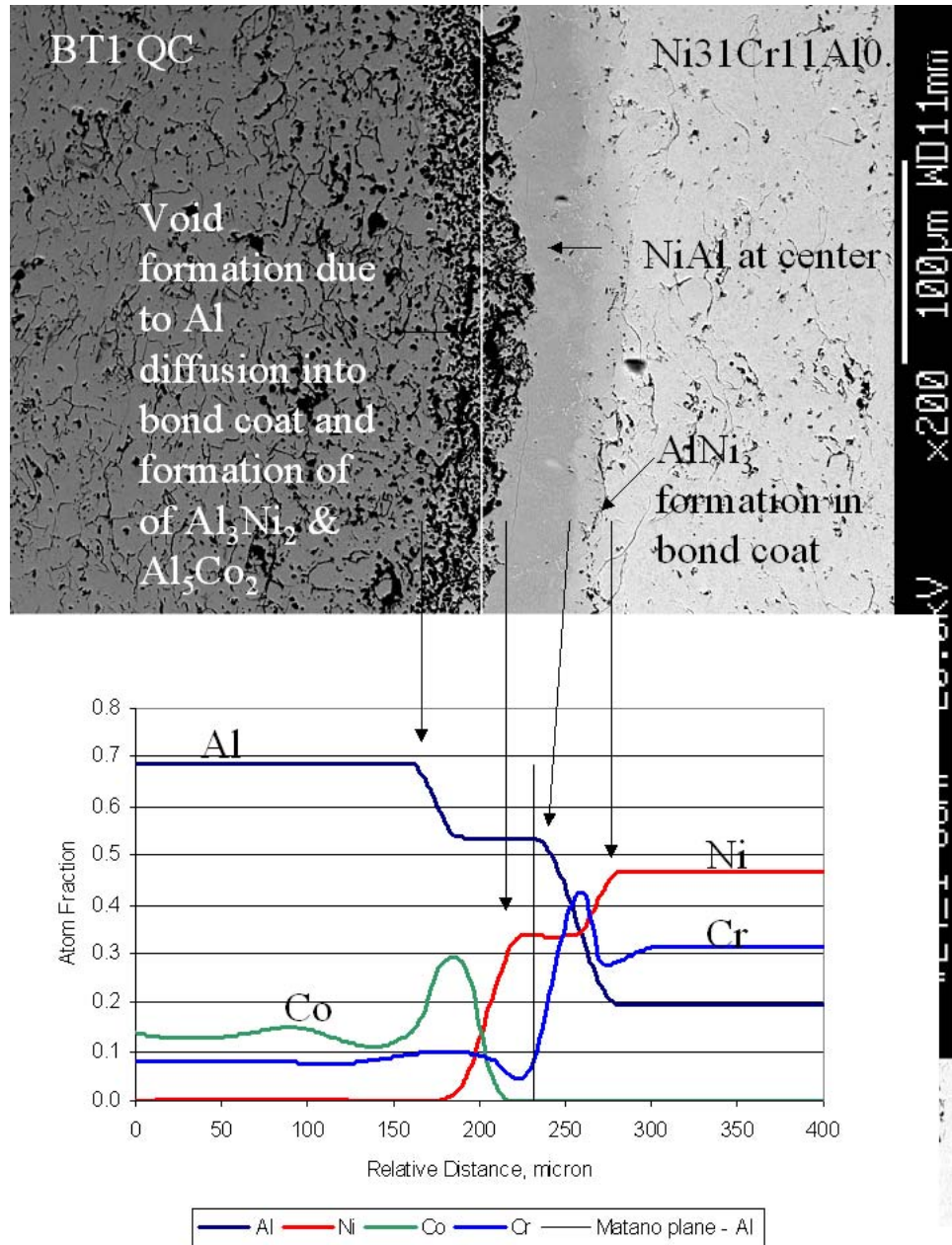


**Figure 6.2-5.** Microstructure of Ni31Cr110.6Y-BT1 diffusion couple after 500 hours at 700 °C showing the development of the phases at the interface. The NiAl intermetallic phase has thickened with Co substituting into the structure on the BT1 QC side of the interface and  $\text{Al}_3\text{Ni}_2$  and  $\text{Al}_5\text{Co}_2$  forming in the void area.  $\text{NiAl}_3$  on the right side of the interface has also thickened and Cr has increase due to the reduction in Ni as it diffuses into the interface.

At 500 hours, these initial observations are in accordance with what is shown Figure 6.2-5, with the AlNi phase growth in the center of the interlay and having a uniform composition of ~55 atom% aluminum and ~35% atom% nickel, indicating the phase to be on the aluminum-rich side of the AlNi field and possibly containing  $\text{Al}_3\text{Ni}_2$  in the structure. The Kirkendall void area increased and the cobalt content increased with the depletion of aluminum into the nickel-rich phase. The aluminum and cobalt contents in this region, with the lighter phase present around the voids indicate AlCo phase formation. A combination of AlCo and AlNi phases eventually transitions into the AlNi phase on the MCrAlY side. A similar transition zone was seen on the bond-coat side of the interlayer, where  $\text{AlNi}_3$  is believed to have formed. The increase in chromium content was similar to that of the cobalt, due to the nickel flux into the interlayer.

The interlayer thickness for the Ni17Cr6Al0.5Y-BT1 couple is less at 100 hours (25  $\mu\text{m}$ ) than for the Ni31Cr11Al0.6Y-BT1 couple (68  $\mu\text{m}$ ) even though the diffusion coefficients and fluxes are nearly the same. The increase in the thickness for the Ni31Cr11Al0.6Y-BT1 is probably due to the higher starting Al content of the bond coat that reduces the amount of Al required to form the intermetallic. This is indicated in Figure 6.2-6, which shows the positions of the two compositions with respect to the  $\text{AlNi}_3$  phase field.

The Fe26Cr6Al0.4Y-BT1 diffusion couple behaved in a similar manner as the nickel-based bond coats, as shown in Figure 6.2-7. The initial phase that developed after 25 hours at the interface was ~40 to 50 atom% aluminum, indicating this to be the FeAl phase. The transition phases into the BT1 QC appeared to have the composition of  $\text{FeAl}_2$ . The cobalt in the BT1 QC diffused into the iron-base bond coat more than in the case of the nickel-based bond coat and did not appear to form AlCo in the BT1 QC. The aluminum diffused into the bond coat as a solid solution. These observations were confirmed in the 500-hour sample, as shown in Figure 6.2-8. The thickness of the phase in the interface increased and the composition indicated it to be a combination of FeAl and AlCo. The composition on either side of the phase was consistent with that at 25 hours. As stated previously, no phases developed in the SAE 1040-BT1 couple at the 700°C temperature.

Interface phase development in 900°C diffusion couples - The phase development in both the nickel- and iron-based bond coat diffusion couples were consistent with what was observed at 700°C, as shown in Figures 6.2-9 and 10. Phases were also seen in the SAE 1040 diffusion couple at the 900°C and were similar to those in the iron-based bond coat, as shown in Figure 6.2-11. The SAE 1040 couple differed in that there were Kirkendall voids

formed at the steel interface. These were probably due to the high rate of aluminum diffusion,  $1.1 \times 10^{-4}$  at%- $\mu\text{m}/\text{sec}$  into the iron which is an order of magnitude higher than that for the bond coats.

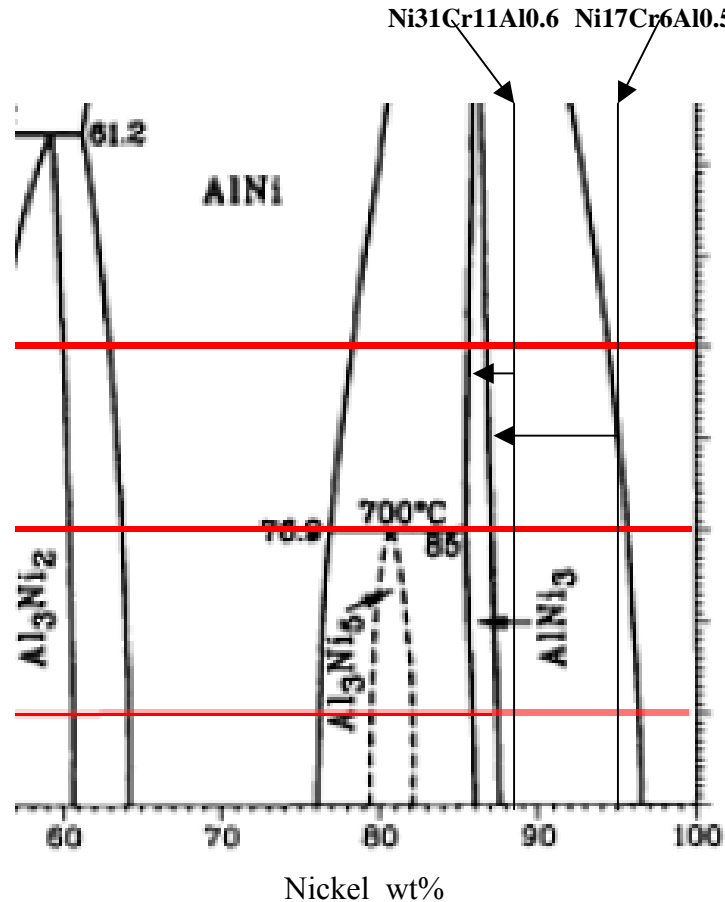


*Figure 6.2-6. Nickel-aluminum phase diagram on the nickel rich side showing the relative location of the aluminum content for the Ni17Cr6Al0.5Y bond coat relative to the Ni31Cr11Al0.6Y bond coat. Note the lower amount of aluminum that would need to be transported to the Ni31Cr11Al0.6Y bond coat to begin the formation of the intermetallic phase at the interface with the BT1 QC.*

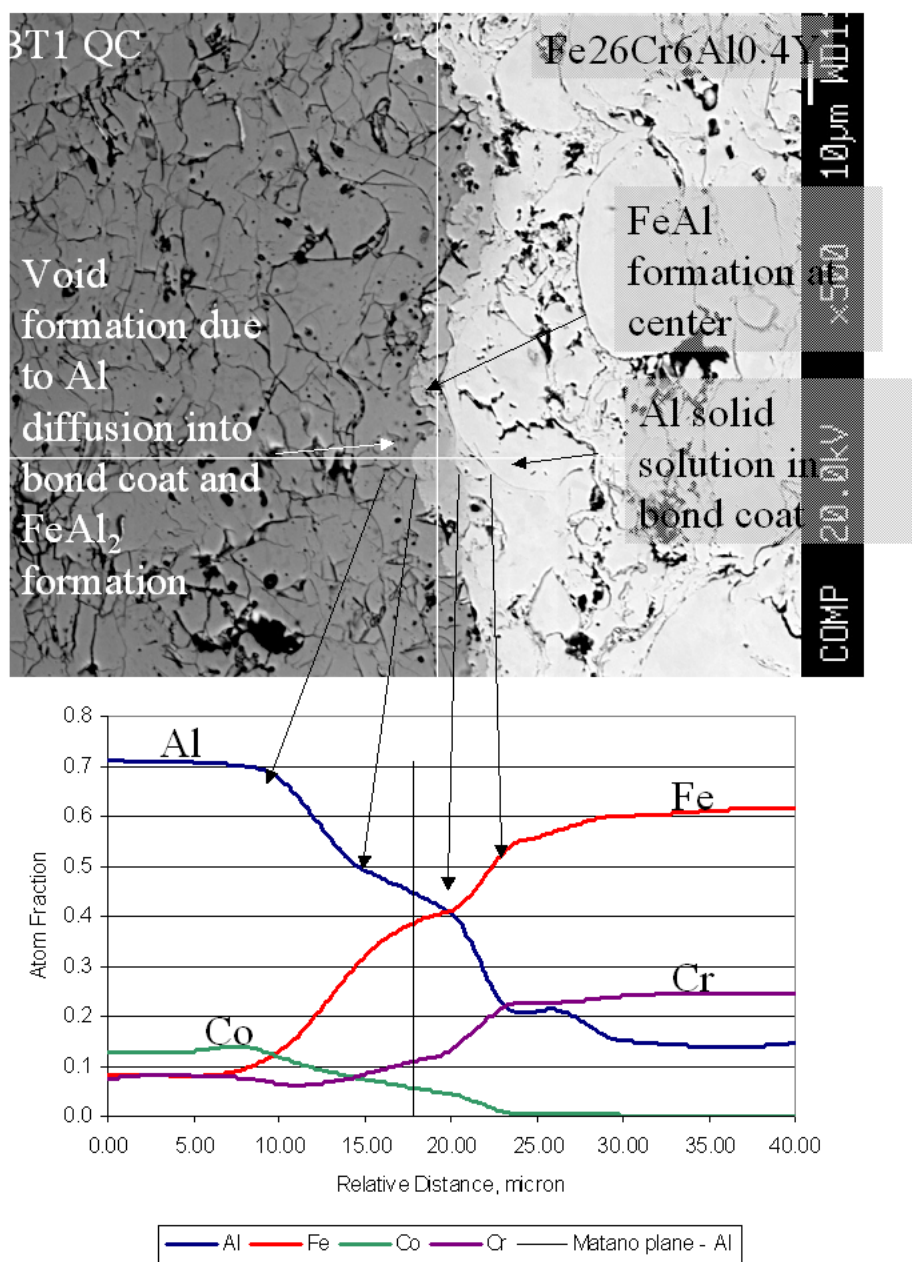


**Figure 6.2-7.** Microstructure of Fe26Cr8Al0.4Y-BT1 diffusion couple after initial 25 hours at 700 °C showing the development of the phases at the interface. The FeAl intermetallic phase initially forms at the interface with FeAl<sub>2</sub> composition indicated in the BT1 QC.

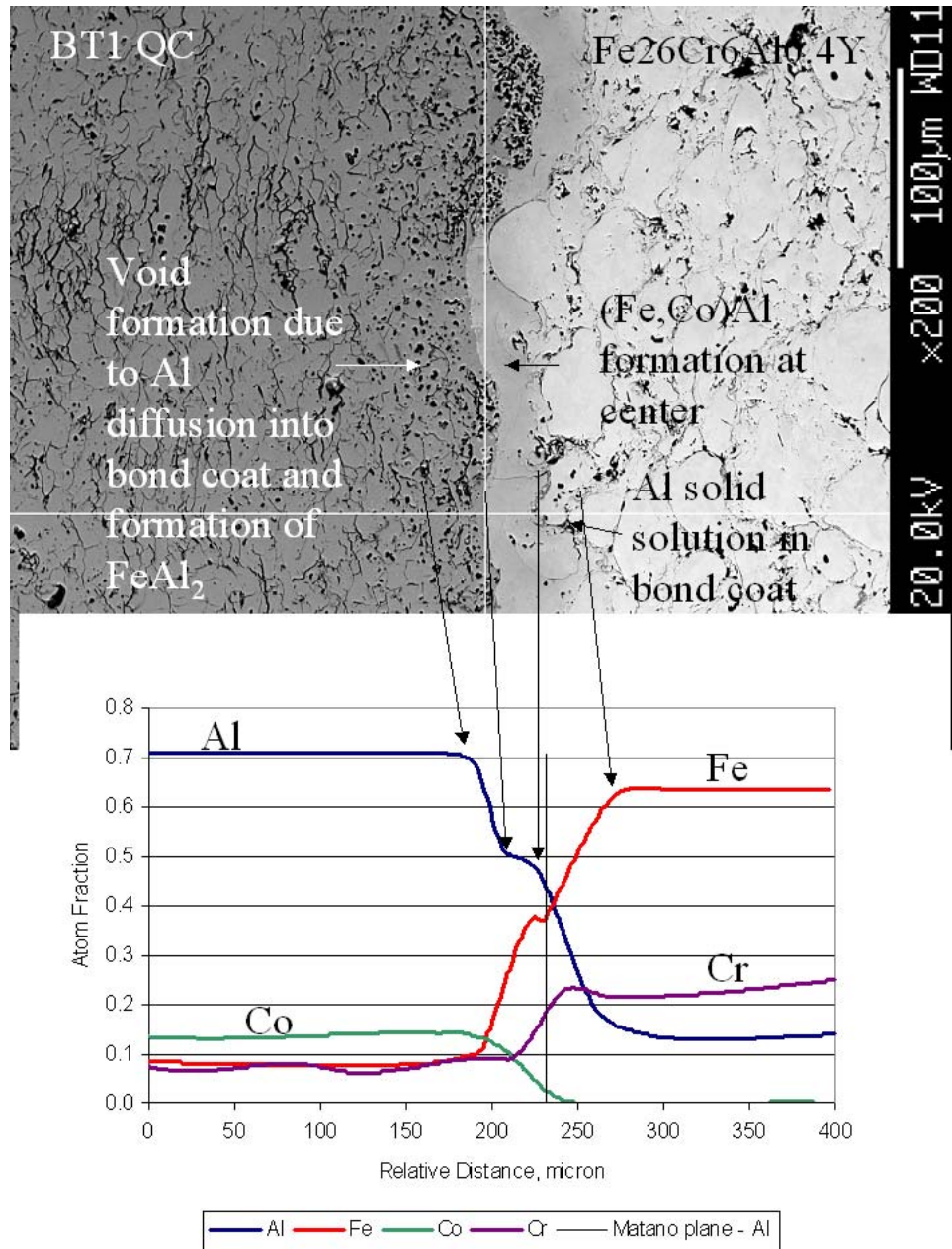


**Figure 6.2-8.** Microstructure of Fe<sub>26</sub>Cr<sub>8</sub>Al<sub>0.4</sub>Y-BT1 diffusion couple after 500 hours at 700 °C showing the development of the phases at the interface. The FeAl intermetallic phase has thickened with Co substituting into the structure on the BT1 QC side of the interface. FeAl<sub>2</sub> begins to form on the BT1 QC side of the interface and the aluminum diffuses into the iron bond coat as solid solution.

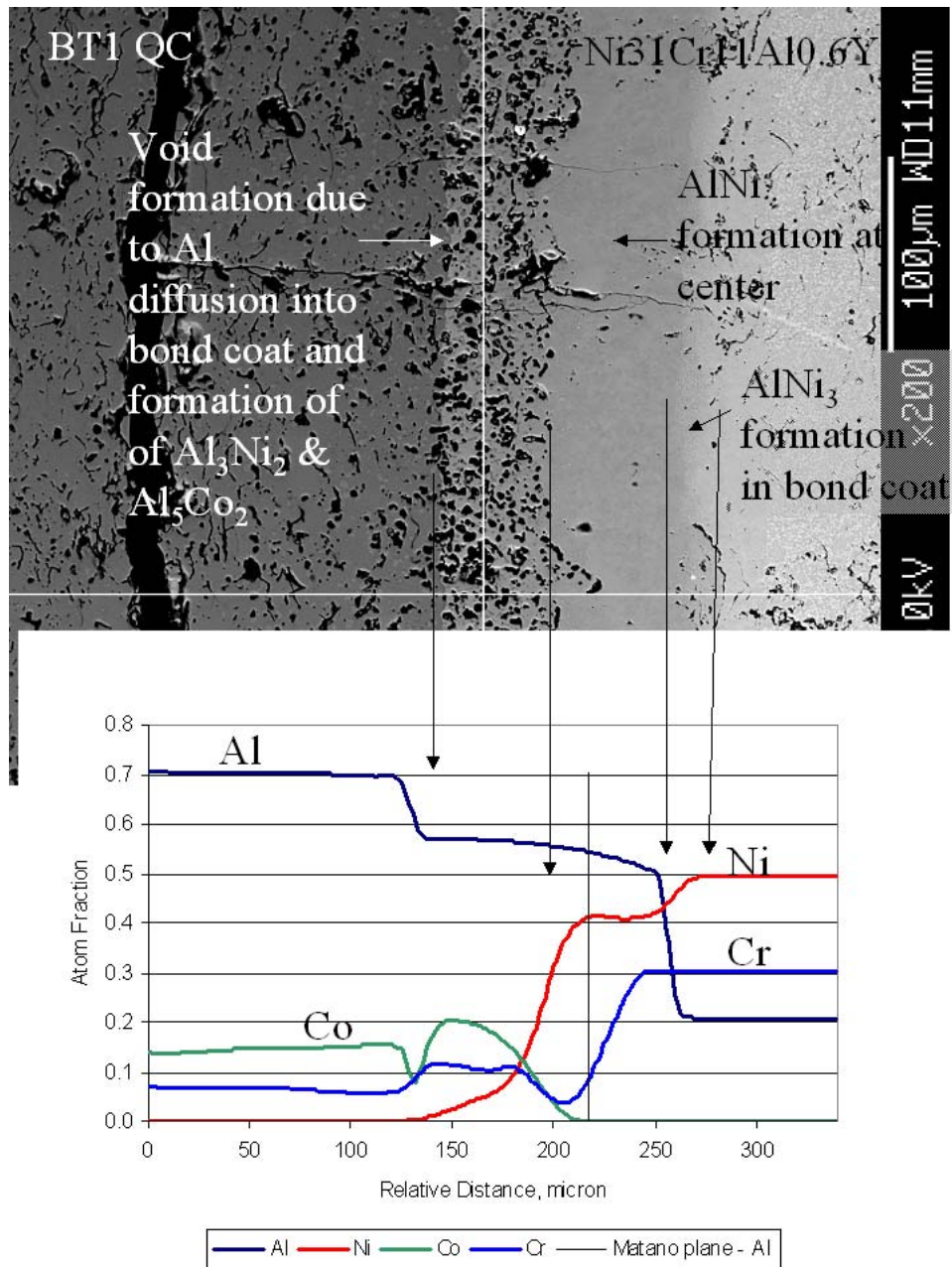


**Figure 6.2-9.** Microstructure of Ni<sub>31</sub>Cr<sub>11</sub>Al<sub>0.6</sub>Y-BT1 diffusion couple after initial 25 hours at 900 °C showing the development of the phases at the interface. The NiAl intermetallic phase forms at the center of the interlayer phase with Al<sub>3</sub>Ni<sub>2</sub> and Al<sub>5</sub>Co<sub>2</sub> forming to the left of the interface due to the relative increase in Co content as the Al diffuses into the bond coat. AlNi<sub>3</sub> forms initial forms in the bond coat until enough Al diffuses into the coating from the interface.

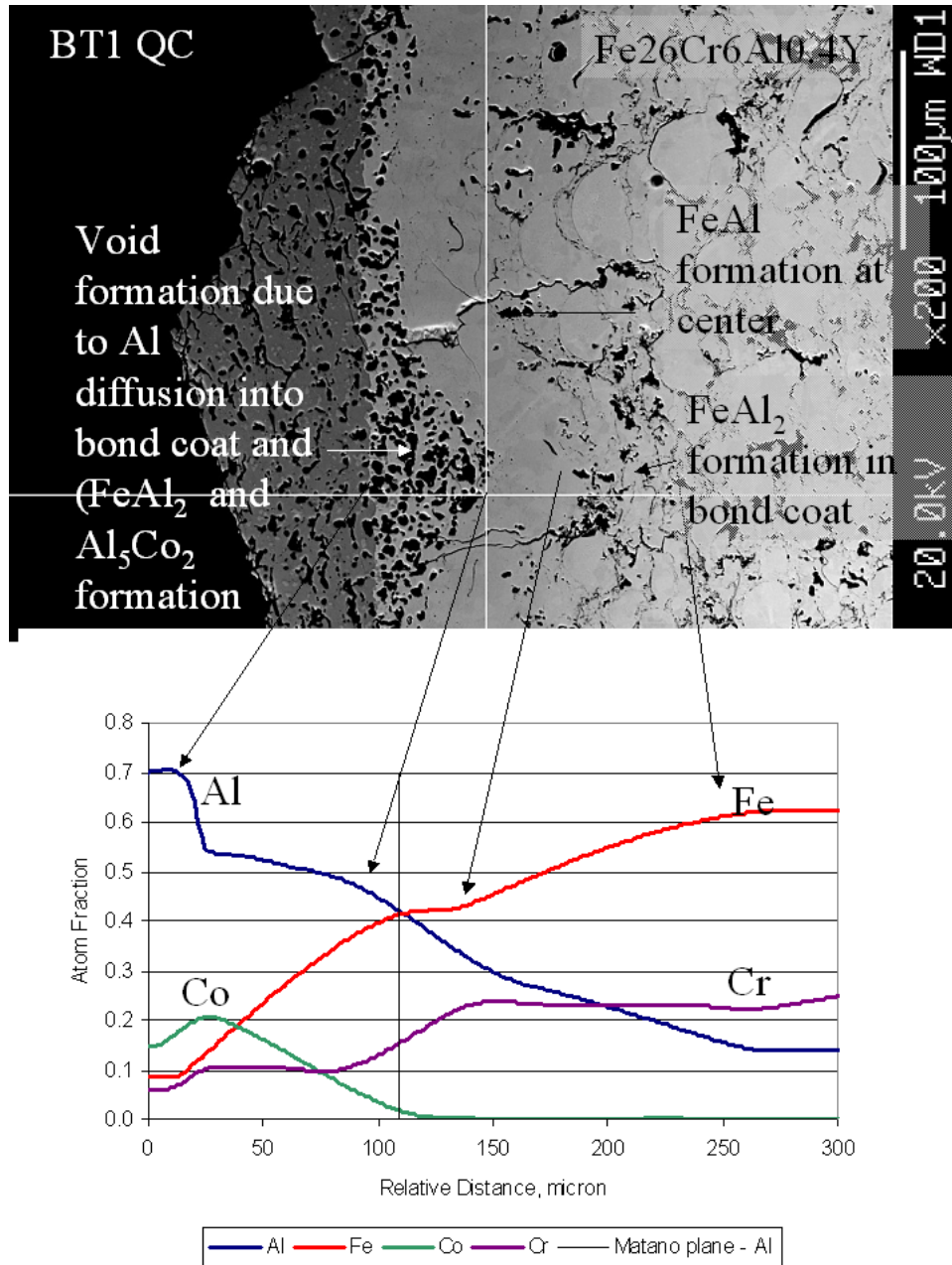


**Figure 6.2-10.** Microstructure of Fe<sub>26</sub>Cr<sub>6</sub>Al<sub>0.4</sub>Y--BT1 diffusion couple after initial 25 hours at 900 °C showing the development of the phases at the interface. The FeAl intermetallic phase form at the center of the interlayer phase with FeAl<sub>2</sub> and Al<sub>5</sub>Co<sub>2</sub> formation to the left of the interface as Al diffuses into the interface increasing the relative Co content. Aluminum diffuses into the iron-based bond coat as solid solutions to the right of the interface.

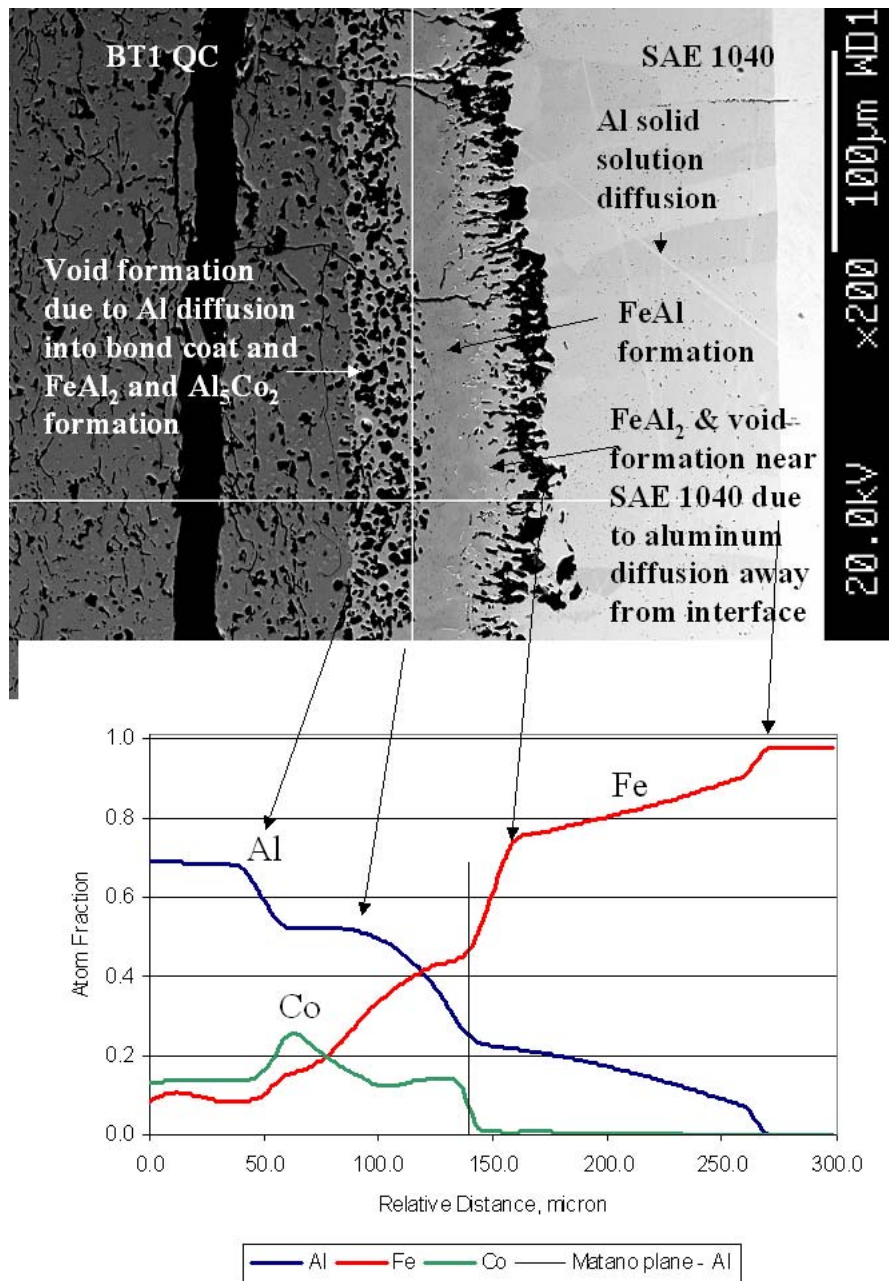


**Figure 6.2-11.** Microstructure of SAE 1040-BT1 diffusion couple after initial 25 hours at 900 °C showing the development of the phases at the interface. The FeAl intermetallic phase form at the center of the interlayer phase with  $\text{FeAl}_2$  and  $\text{Al}_5\text{Co}_2$  formation to the left of the interface as Al diffuses into the interface increasing the relative Co content. Aluminum diffuses into the steel substrate as solid solutions to the right of the interface.

### 6.3 Diffusion Coefficients

The plots for the average the diffusion coefficients for the aluminum and nickel or iron shown in Figures 5.6-7 and 5.6-8 of Section 5.6 support the phase-development observations at the interface of the diffusion couples. It can be readily seen that the interdiffusion coefficients for the nickel- and iron-bond coat couples are similar in magnitude at all temperatures and should result in the similar interface microstructures if nickel and iron are assumed to be chemically similar, which they are at the temperatures of interest. For the SAE 1040 couple, the diffusion coefficients for aluminum and iron were considerably different than those for the nickel- or iron-based bond coat couples at 700°C.

Linear equation fits with  $R^2$  correlation fitting parameters are given in Table 5.6-2. The cause for the lower diffusion coefficient for the SAE 1040 couple at 700°C is unclear. One significant difference between the SAE 1040 couple and that of the bond coat couples is the grit blasting of the initial SAE 1040 surface prior to spraying. The bond coat couples were not grit blasted prior to the BT1 QC being sprayed onto the bond coat (the substrate prior to applying the bond coat was grit blasted). Embedded grit particles are evident in the interface between the BT1 and SAE 1040, as shown in Figure 5.4-3e. It has been shown by internal work at Caterpillar Inc. that this type of grit blasting can result in contamination of up to 35% of the surface of the steel with the aluminum oxide grit used. This contamination has been shown to reduce the wetting of the surface during cladding of steel surfaces by welding processes. This contamination may also act as a diffusion barrier in the SAE 1040-BT1 diffusion couples. Prior studies of diffusion of bond coat materials on grit blasted interfaces may not have shown this affect due to the higher temperatures used (800° to 1200°C) similar to the increase in diffusion for the SAE 1040 couples at 900°C.

The clustering of the diffusion coefficients at the 500°C temperature is probably more a factor of the lower mobility at this temperature and the lack of precision of the concentration gradients used.

Interaction of the alloying elements result in lower mobility of aluminum and iron. Prior work by Hirano et al. [56] in determining interdiffusion coefficients for iron, nickel and cobalt in aluminum measured higher interdiffusion coefficients for iron and nickel than what was determined in this study in the temperature range of 359°C to 630°C, Figure 6.3-1. Diffusion coefficients in the iron- and nickel-based bond coat couples at 500°C and 700°C were also lower than those reported by Hirano et al. [56]. In addition, Jindal et al. [57] reported rapid growth of iron aluminide at the interface of diffusion couples at 500°C to 600°C made by roll bonding pure iron and aluminum [57]. No iron aluminide was found in

the SAE 1040 couples in this study at 500°C or 700°C probably due to the alumina contamination previously discussed.

The high purity, low-carbon iron used in the study by Jindal et al. [57] was inferred to have led to the rapid formation of the interlayer. High purity, low-carbon iron was also used by Hirano et al. [56]. The influence of the minor alloying elements in the SAE 1040 steel may have some influence on the interlayer formation of the iron aluminide but no definite evidence of this was present in the current study. The studies by Hirano et al. and Jindal et al. used roll bonded and chemically plated samples that would not have been influenced by contamination of the interface as proposed for the SAE 1040-BT1 couples.

The lower diffusion coefficients for the nickel- and iron-containing bond-coat couples compared to the prior work require a different explanation. The diffusion coefficients for the bond-coat couples and the prior studies [56] appear to converge at 700°C with the diffusion coefficients for the pure aluminum and iron being slightly higher. This would suggest that the lower coefficients in the bond-coat materials are due to the chromium content (17 wt% and 31 wt% for the nickel and 26wt% for the iron) that has been reported to increase the chemical activity of aluminum, resulting in a slower diffusion in nickel and iron [58,59]. This dependence was reported to be weak at the 900°C to 1200°C range for the prior work, but it appeared to increase with decreasing temperature in this study.

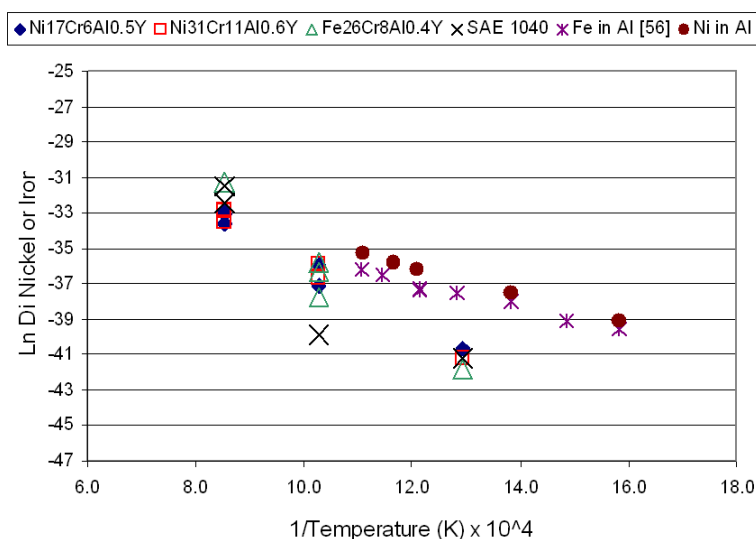


**Figure 6.3-1.** The average diffusion coefficient ( $D_{i,C}$ ) for nickel or iron for current work compared to prior work of Hirano et al. [56] showing lower values.

#### 6.4 Bond Coat and Graded Material Selection

The extrapolated penetration depths shown in Table 5.7-1 would indicate that if the TBC system is designed to have an interface temperature of 400°C between the bond coat and BT1 insulating top coat, no bond coat would be required to prevent excessive reaction with the BT1 and substrate. The low alloy steels used for pistons in advanced diesels will, however, require a bond coat material for long-term oxidation resistance. The nickel-based bond-coat materials are the best selection for this as they also provide for strain relief between the iron-based substrates and the BT1 as both have high thermal expansion coefficients.

A TBC system that uses a metallic material graded with the BT1 to provide toughness and strength to the BT1 will require different criteria for selection due to the large diffusion interaction between the nickel-base bond coats and the BT1. Even at a relatively low temperature of 500°C, interaction zones at 10,000 hours on the order of 5 to 6  $\mu\text{m}$  are predicted. This is the size of the metallic graded material in the TBC coating as shown in Figure 6.4-1.

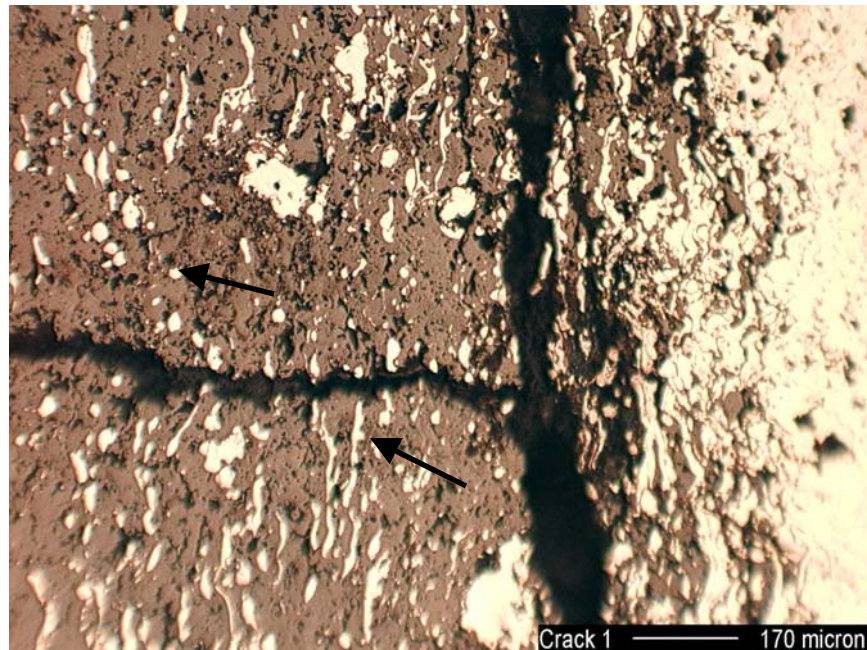


*Figure 6.4-1. Higher magnification of graded TBC structure shown in Figure 1-1 showing the metallic graded phase (white areas indicated by arrows) to be on the order of 5 to 10  $\mu\text{m}$  in thickness.*

If the lower diffusion at 700°C for the SAE 1040 steel is due to the embedding of grit, this may provide a method to reduce the interaction of the bond coat materials with the BT1. A pre-oxidation of the bond coat surface prior to deposition of the BT1 coating would allow the aluminum in the bond coat to develop into an oxide scale that could aid in reducing the diffusion as seen in the SAE 1040 couples. Further work is required to determine in this affect does occur (alumina reducing the diffusion kinetics) and at would temperatures it would be affect as the SAE 1040 couples do show dramatic diffusion zones at 900°C.

Different materials than that of the  $\gamma$ -Ni +  $\beta$ -AlNi bond coats used in this study may be required. One possibility is to use single-phase  $\beta$ -AlNi as the grading material. As the AlNi phase develops at the interface of the BT1 and nickel-based bond coats, it should be stable when in contact with the BT1 at temperature. This is probably another reason for the reduction in the interaction layer thickness that Sanchez et al. [5] found in the use of diffusion barriers in addition to any effect caused by the addition of yttria. The AlNi coating with yttria that they used resulted in a much lower interlayer formed than the BT1 with yttria. Although Sanchez et al. attributed this to the yttria addition to the AlNi, the results of this study would indicate that AlNi would be stable with the BT1 QC and aid in the prevention and growth of a reaction layer.

## 7.0 Conclusions

Results of this study indicate a potential for use of the BT1 quasicrystalline approximant material for TBC systems for diesel engine components, particularly when the maximum coated-component temperatures will be 700°C or less. At higher temperatures, the coating structure changes that occur in the BT1 QC coating will impact the durability of the coating system. Specific conclusions are as follows:

1. The BT1 QC powder can be sprayed into dense and adherent coating structures using high velocity oxygen-fuel spray processes with deposition efficiencies that are economical for production applications.
2. The BT1 QC coatings undergo coating structural changes with exposure to temperatures of 700°C or higher. This includes a reduction in microcrack density and porosity consolidation. These changes in the coating structure led to mechanical property changes, specifically changes in the coating modulus, that will need to be accounted for in the design of the TBC systems using the BT1 QC material. The changes in mechanical properties will be the limiting factor in regard to durability of the BT1 QC material in TBCs for diesel engine components.
3. The crystallographic aspects of the BT1 QC material changes with time at temperatures above 700°C as indicated by the changes in XRD pattern of the coating. The changes in phase may be associated with what appears to be precipitation and growth of quasicrystalline phases in the structure. As long as these changes do not significantly increase the BT1 QC thermal conductivity, they should not significantly impact the use of the material in TBC systems for diesel engine components.
4. An interface compound of the AlNi or AlFe type developed at the interface between the BT1 QC coating and the MCrAlY bond coat materials at 700°C and above. Predicted growth kinetics for the interlayer phase from the diffusion study indicates that the use of MCrAlY materials as a bond coat will be limited to applications with temperatures below 600°C.
5. Single-phase nickel aluminide (AlNi) may potentially be a metallic material for use with the BT1 QC coating in a graded TBC system at temperatures above 600°C as it appears to be a stable phase when in contact with the BT1 QC at temperatures above 700°C

## References

1. Miller, R. A., "Thermal Barrier Coatings for Aircraft Engines - History and Directions", J. of Thermal Spray Tech., 6 [1] 35 (1997).
2. Dubois, J.M., Thiel, P. A., Tsai, A.P., and Urban, K., "Quasicrystals", Mat. Res. Soc., Sym. Proc. 553 preface (1999).
3. Urban, K., Feuerbacher, M. and Wollgarten, M., "Mechanical Behavior of Quasicrystals", MRS Bulletin 65-68 (November 1997).
4. Archambault, P., Plaindoux, P., Belin-Ferre, E., and Dubois, J. M., "Thermal and Electronic Properties of an AlCoFeCr Approximant of the Decagonal Phase", Mat. Res. Soc. Symp. Proc., 553 409-414 (1999).
5. Sánchez, A., Garcia, F. J., Algaba, J. M., Alvarez, J., Vallés, P., Garcia-Poggio, M. C., and Agüero, A., "Application of Quasicrystalline Materials as Thermal Barriers in Aeronautics and Future Perspectives of Use for These Materials", Mat. Res. Soc. Symp. Proc. 553 447-458 (1999).
6. Tucker, R.C., "Thermal Spray Coatings", ASM Handbook Ninth Ed. 5 (1994).
7. Soechting, F. O., "A Design Perspective on Thermal Barrier Coatings", Thermal Barrier Coatings Workshop, NASA Conference Publication 3312, 1-15 (1995).
8. Bose, S. and DeMasi-Marcin, J., "Thermal Barrier Coating Experience in Gas Turbine Engine at Pratt & Whitney", J. of Thermal Spray Tech. 6 [1] 99 (1997).
9. Brindley, W. J., "Properties of Plasma Sprayed Bond Coats", J. of Thermal Spray Tech. 6 [1] 85 (1997).
10. Gaffin, W. O., "JT9D Ceramic Outer Air Seal System Refinement Program", NASA-CR-165554 (1982).

11. Nelson, W. A. and Orenstein, R. M., "TBC Experience in Land Based Gas Turbines", J. of Thermal Spray Tech. 6 [2] 176 (1997).
12. Zhu, D., Nesbit, J. A., McCue, T. R., Barrett, C. A., and Miller, R. A., "Furnace Cyclic Behavior of Plasma-Sprayed Zirconia-Yttria and Multi-Component Rare Earth Oxide Doped Thermal Barrier Coatings", Ceram. Eng. & Sci. Proc. 23 [4] 533-545 (2002).
13. Fritscher, K., Szucs, F., Schulz, U., Saruhan, B., Peters, M. and Kaysser, W. A., "Impact of Thermal Exposure of EB-PVD TBCs on Young's Modulus and Sintering", Ceram. Eng. & Sci. Proc. 23 [4] 341-352 (2002).
14. Bast, U. and Schumann, E., "Development of Novel Oxide Materials for TBC's", Ceram. Eng. & Sci. Proc. 23 [4] 525-532 (2002).
15. Zhu, D. and Miller, R. A., "Thermal Conductivity and Sintering Behavior of Advanced Thermal Barrier Coatings", Ceram. Eng. & Sci. Proc. 23 [4] 457-468 (2002).
16. Miller, R. A., "Assessment of Fundamental Materials Needs for Thick Thermal Barrier Coatings (TTBC's) for Truck Diesel Engines", DOE/NASA/21749-1, NASA TM-103130 (1990).
17. Zhu, D., Lee, K. N., and Miller, R. A., "Sintering and Cyclic Failure Mechanisms of Thermal and Environmental Barrier Coating Systems Under Thermal Gradient Test Conditions", Ceram. Eng. & Sci. Proc. 23 [4] 505-516 (2002).
18. Zhu, D. and Miller, R. A., "Determination of Creep Behavior of Thermal Barrier Coatings Under Laser Imposed Temperature and Stress Gradients", NASA TM-113169, ARL-TR-1565 (2000).
19. Yonushonis, T. M., "Overview of Thermal Barrier Coatings in Diesel Engines", J. of Thermal Spray Tech., 6 [1] 50 (1997).
20. Kvernes, I., Fartum, P., and Henriksen, R., "Characterization of Microstructures and Measurements of Thermal Effects of Ceramic Coatings in Service", Metallurgical

Coatings 1980, American Vacuum Society, Elsevier Sequoia, Lausanne and New York, 2 478 (1980).

21. Beardsley, M. B. and Larson, H. J. "Thick Thermal Barrier Coatings for Diesel Components", DOE/NASA/0332-1, NASA CR-190759 (1992).
22. Kulkarni, A., Gutleber, J., Sampath, S., Goland, A., Lindquist, W.B., Herman, H., Allen, A.J., and Dowd, B., "Studies of the microstructure and properties of dense ceramic coatings produced by high-velocity oxygen-fuel combustion spraying", *Mat. Sc. & Eng.*, A369, 124-137 (2004).
23. Beardsley, M. B., Happoldt, P. G., Kelley, K. C., Rejda, E. F., and Socie, D. F., "Thermal Barrier Coatings for Low Emission, High Efficiency Diesel Engine Applications", SAE Tech. Paper Series, 1999-01-2255, Government/Industry Meeting, Washington, D.C. (1999).
24. Brink, R. C., "Material Property Evaluation of Thick Thermal Barrier Coating Systems", ASME, 89-ICE-13 (1989).
25. Trice, R. W., Prine, D. W., and Faber, K. T., "Deformation Mechanisms in Compression-Loaded, Stand-Alone Plasma-Sprayed Alumina Coatings", *Ceram. Eng. Sci. Proc.* 22 [4] 477-433 (2000).
26. Beardsley, M. B., "Thick Thermal Barrier Coatings for Diesel Engines", *J. of Thermal Spray Tech.* 6 [2] 181 (1997).
27. Wesling, K. F., Socie, D. F., and Beardsley, M. B., "Fatigue of Thick Thermal Barrier Coatings", *J. Am. Ceram. Soc.* 77 [7] 1863-1868 (1994).
28. Rejda, E. F., Socie, D. F., and Itoh, T., "Deformation Behavior of Plasma-Sprayed Thick Thermal Barrier Coatings", *Surf. Coatings Tech.* 113 218-226 (1999).
29. Shechtman, D. and Lang, C.I., "Quasiperiodic Materials: Discovery and Recent Developments", *MRS Bulletin* 40-42 (Nov. 1997).

30. Steurer, W., "Approximants-the key to the structure of quasicrystals", Mat. Res. Soc. Symp. Proc. 643 K3.2.1 (2001).
31. Quichandon, M., Calvayrac, Y., Quivy, A., Faudot, F., and Gratias, D., "Phase Diagrams and Approximants", Mat. Res. Soc. Symp. Proc. 553 95-106 (1999).
32. Yamada, H., Takeuchi, T., Mizutani, U., and Tanaka, N., "Structural Studies of  $\text{Al}_{55}\text{Si}_7\text{Cu}_{25.5}\text{Fe}_{12.5}$  1/1-Cubic Approximant by Means of X-Ray Rietveld Method and HAADF-STEM", Mat. Res. Soc. Symp. Proc. 553 177-182 (1999).
33. Luck, R., Scheffer, M., Godecke, T., Ritsch, S., and Beeli, C., "Phase Diagram Determination for Modifications of the D Phase in the Al-AlCo-AlNi System", Mat. Res. Soc. Symp. Proc. 533 25-36 (1999).
34. Tsai, A.P., "Metallurgy of Quasicrystals: Alloys and Preparation", MRS Bulletin 43-47 (Nov. 1997).
35. Archambault, P., and Janot, C., "Thermal Conductivity of Quasicrystals and Associated Processes", MRS Bulletin 48-53 (Nov. 1997).
36. Takeuchi, S., "Bulk Mechanical Properties of Quasicrystals", Mat. Res. Soc. Symp. Proc. 553 283-294 (1999).
37. Schurack, F., Eckert, J., and Schultz, L., "Processing and Mechanical Properties of Quasicrystal-Reinforced Al-Alloys", Mat. Res. Symp. Proc. 643 K9.11.1. (2001).
38. Bailey, D., Chandler, P., Raymond, P., and Nicoll, A. R., "High Performance Surface Engineering from Plasma Spraying", Mat'ls. & Des. 9 [6] 232 (1988).
39. Feit, E. and Shaw, H., "Advances in Thermal Properties Testing at Oak Ridge National Laboratories", Ceramic Bulletin, 70 [1] 125 (1991).
40. Stecura, S., "Optimization of the NiCrAl-Y/ZrO<sub>2</sub>-Y<sub>2</sub>O<sub>3</sub> Thermal Barrier System", NASA TM-86905, (1985).

41. Besser, M. F. and Eisenhammer, T., "Deposition and Applications of Quasicrystalline Coatings", MRS Bulletin 59-63 (Nov. 1997).
42. Huttunen-Saarivirta, E., Turunen, E., and Kallio, M., "Microstructural characterization of thermally sprayed quasicrystalline Al-Co-Fe-Cr", J. of Alloys and Compounds, 354, 269-280 (2003).
43. Dong C., "The Concept of the Approximants of Quasicrystals", Scripta Metallurgica, 33, [2] 239-243 (1995).
44. Wehner, B.I., Koster, U., Rudiger, A., Pieper, C. and Sordélet, D.J., "Oxidation of Al-Cu-Fe and Al-Pd-Mn quasicrystals", Mat. Sci. & Engr. A, 294-296, 830-833 (2000).
45. Yamasaki, M. and Tsai, A. P., "Oxidation behavior of quasicrystalline Al<sub>63</sub>Cu<sub>25</sub>Fe<sub>12</sub> alloys with additional element", J. of Alloys and Compounds, 342, 473-476 (2002).
46. Demange, V., Machizaud, F., Dubois, J. M. Anderegg, J. W. Thiel, P. A. and Sordélet, D. J., "New approximants in the Al-Cr-Fe system and their oxidation resistance", J. of Alloys and Compounds, 342, 24-29 (2002).
47. Kong, J., Zhou, C. Gong, S. and Huibin, X., "Low-pressure plasma-sprayed Al-Cu-Fe-Cr quasicrystalline coating for Ti-based alloy oxidation protection", Surf. & Coating Tech., 165, 281-285 (2003).
48. Morral, J.E., and Barkalow, R.H., "Analysis of Coating/Substrate Interdiffusion with Normalized Distance and Time", Scripta Met., 16, 593-594 (1982).
49. Dayananda, M.A., "Average Effective Interdiffusion Coefficients in Binary and Multicomponent Alloys", Defect and Diffusion Forum, 95-98, 521-536 (1993).
50. Dayananda, M.A., "A New Analysis for the Determination of Ternary Interdiffusion Coefficients from a Single Diffusion Couple", Met. & Mat. Trans. A, 30A, 535-543, (1999).

51. Dayananda, M.A., "MultiDiFlux©", Purdue Univ. Sch. of Mat'ls. Engr., Copyright 2003, 2007.
52. Thomas, G. B., "Calculus and Analytic Geometry", 4<sup>th</sup> ed., Addison-Wesley Pub. Co., 178-182, (1969)
53. d'Heurle, F.M. and Ghez, R., "Reactive diffusion in a prototype system: nickel-aluminum I: Non-constant diffusion coefficient", Thin Solid Film, 215, 19-25 (1992)
54. Gleeson, B., Wang, W., Hayashi, S., and Sordet, D., "Effects of Platinum on the Interdiffusion and Oxidation Behavior of Ni-Al-Based Alloys", to be published.
55. ASM International, Handbook Online, "Phase Diagrams", [3], (2002).  
<http://products.asminternational.org/hbk/index.jsp>
56. Hirano, K-I., Agarwala, R.P., and Cohen, M., "Diffusion of Iron, Nickel and Cobalt in Aluminum", Acta Met., 10, 857-863, (September 1962) .
57. Jindal, V., Srivastava, V.C., Das, A., and Ghosh, R.N., "Reactive diffusion in the roll bonded iron-aluminum system", Mat. Letters, 60, 1758-1761, (2006).
58. Nesbitt, J.A., and Heckel, R.W., "Interdiffusion in Ni-Rich, Ni-Cr-Al Alloys at 1100 and 1200 °C: Part II. Diffusion Coefficients and Predicted Concentration Profiles", Met. Trans. A, 18A, 2075-2085 (Dec 1987)
59. Akuezue, H.C. and Stringer, J., "Interdiffusion in Ternary Fe-Cr-Al Alloys", Met. Trans. A, 20A, 2767-2781 (December 1989).
60. Oliver, W. C. and Pharr, G. M., "An improved technique for determining hardness and elastic modulus using load and displacement sensing indentation experiments", J. Mater. Res., 7, [6], 1564-1583 (Jun 1992).
61. Herbert, E.G., Pharr, G.M., Oliver, W.C., Lucas, B.N. and Hay, J.L., "On the measurement of stress-strain curves by spherical indentation", Thin Solid Film, 389-399, 331-335 (2001).

62. Alcalá, J., Gaudette, F., Suresh, S. and Sampath, S., “Instrumented spherical micro-indentation of plasma-sprayed coatings”, *Mat. Sc. & Eng.*, A316, 1-10 (2001).
63. Malzbender, J., and Steinbrech, R.W., “Determination of the stress-dependent stiffness of plasma-sprayed thermal barrier coatings using depth-sensitive indentation”, *J. Mater. Res.*, 18 [8] 1975-1984 (2003).
64. Duan, K., and Steinbrech, R.W., “Influence of Sample Deformation and Porosity On Mechanical Properties by Instrumented Microindentation Technique”, *J. of the European Ceram. Soc.*, 18, 87-93 (1998).
65. Thompson, J.A. and Clyne, T.W., “The Effect of Heat Treatment on the Stiffness of Zirconia Top Coats in Plasma-Sprayed TBCs”, *Acta Mater.*, 49, 1565-1575 (2001).
66. Reyes-Gasga, J., Pita-Larrañaga, A., Valles-Gonzalez, M.P., and Sánchez-Pascual, A., “Observation of a decagonal quasicrystalline phase and quasicrystalline approximants in in-situ heated thin films of the Al-Co-Cr-Fe-O system”, *Thin Solid Films*, 355-356, 506-512 (1999).
67. Reyes-Gasga, J., Pita-Larrañaga, A., Mondragón-Galicia, G., Valles-Gonzalez, M.P., and Sánchez-Pascual, A., “Presence of oxygen in the structure of quasicrystalline phases in in-situ heated thin films of the Al-Co-Cr-Fe-O and Al-Mn-Si-O systems”, *Mat’ls. Sci. & Eng.*, 294-296, 850-853 (2000).
68. Nelson, W. A. and Orenstein, R. M., “TBC Experience in Land Based Gas Turbines”, *Thermal Barrier Coating Workshop, NASA Conf. Publication 3312*, 91-110, (1995).